

Technische Universität München
Lehrstuhl für Hochfrequenztechnik

**Polarimetric SAR Modelling
of a Two-Layer Structure**
– A Case Study Based on Subarctic Lakes –

Noora Al-Kahachi

Vollständiger Abdruck der von der Fakultät für Elektrotechnik und
Informationstechnik der Technischen Universität München zur Erlangung des
akademischen Grades eines

– *Doktor-Ingenieurs* –

genehmigten Dissertation.

Vorsitzender: Univ.-Prof. Dr.-Ing. Eckehard Steinbach
Prüfer der Dissertation: 1. Univ.-Prof. Dr.-Ing., Dr.-Ing. habil. Jürgen Detlefsen (i.R.)
2. Univ.-Prof. Dr.-Ing. habil. Alberto Moreira
Karlsruher Institut für Technologie

Die Dissertation wurde am 25.04.2013 bei der Technischen Universität
München eingereicht und durch die Fakultät für Elektrotechnik und
Informationstechnik am 14.10.2013 angenommen.

Zusammenfassung

Die vorliegende Arbeit liefert einen Beitrag zur Interpretation vollpolarimetrischer SAR-Daten von (flachen) subarktischen Seen. Zweck ist es, das Potenzial eines Radars mit synthetischer Apertur aufzudecken, das zur Ermittlung der Eigenschaften von unter der Oberfläche gelagerter Schichten und Inhomogenitäten im Eis – vorwiegend Methanbläschen – beitragen kann.

Dazu wird ein Modell der polarimetrischen Rückstreuung einer zweischichtigen Struktur erarbeitet, wie sie auch mit einem seitlich blickenden Radar mit synthetischer Apertur bei niedrigen Frequenzen (L-Band) gemessen wird. Die obere Schicht ist wenige Meter dick und enthält Inhomogenitäten. Das erstellte Modell beschreibt die Rückstreuung als inkohärente Überlagerung der drei Hauptbeiträge: Streuung an der Zwischenschicht (X-Bragg), Rückstreuung des Volumens kleiner Teilchen und Zweifachstreuung. Das Volumen wird als Wolke teilweise vertikal ausgerichteter Ellipsoide modelliert. Die Komponente mit zweifacher Streuung entsteht durch Streuung an der Wolke kleiner Teilchen – verantwortlich für die Volumenstreuung – und anschließender Reflektion an der Zwischenschicht. Die mathematischen Ausdrücke für diese zweifache Streuung werden hier erstmals vorgestellt und erweisen sich als wesentlicher Bestandteil des Modells.

Die Berechnungen mit dem Modell werden mit SAR-Daten verglichen. Die Daten stammen von ALOS-PALSAR, aufgenommen über gefrorenen, flachen, subarktischen Seen verschiedener Gebiete in den nördlichen subarktischen Regionen. ALOS-Daten zeigen die gleiche polarimetrische Signatur wie die Modellsimulationen. Das Modell kann zeitliche Veränderungen des Eises beschreiben und zwischen bis auf den Grund gefrorenen Seen und Seen mit schwimmendem Eis unterscheiden.

Abstract

The work contributes to the interpretation of quad polarimetric SAR data over (shallow) subarctic lakes, on the purpose of investigating SAR capabilities in revealing facts about the subsurface and the inhomogeneities within the ice layer which are dominated mainly by methane bubbles.

For this, a model for the polarimetric backscattering from a two-layer structure observed by a fully polarimetric side looking synthetic aperture radar at low frequency (L-Band) is developed. The upper layer thickness is few metres thick and contains inhomogeneities. The developed model describes the backscattering as the incoherent sum of the three main contributions: subsurface (X-Bragg), volume and dihedral backscattering. The volume is modelled as a cloud of partially vertically oriented ellipsoids. The dihedral backscattering component is modelled as the electromagnetic wave reflected on the subsurface after being scattered by the same cloud of particles that is responsible for the volume backscattering. The mathematical formulation of this dihedral backscattering is presented for the first time here and proved to be an essential component in the model.

The model simulations are compared to data obtained by ALOS-PALSAR over frozen shallow subarctic lakes acquired over several regions in the northern wetlands. ALOS data show the same polarimetric backscattered signature as the simulations. The model can describe temporal changes of the ice and the difference between grounded and floating ice.

Contents

1	Introduction	1
1.1	Ice Inhomogeneities and Methane Bubbles	3
1.2	Subarctic Lakes	4
1.3	Polarimetric SAR: State of the Art	6
1.4	ALOS-PALSAR System	7
1.5	Objectives and Scope of the Work	8
2	Polarimetric SAR Principles	11
2.1	Polarimetric Scattering Matrix	12
2.2	Pauli Scattering Vector	13
2.3	Radar Cross Section	14
2.3.1	Covariance Matrix	16
2.3.2	Coherency Matrix	16
2.4	Eigen Decomposition	17
2.4.1	Polarimetric Entropy, Anisotropy and Mean Alpha Angle	19
2.4.2	Entropy-Alpha Histogram	20
2.5	Model-Based Decomposition	23
2.5.1	Surface Scattering Contribution	23
2.5.2	Dihedral Scattering Contribution	24
2.5.3	Volume Scattering Contribution	26
3	Experimental Data	29
3.1	Test Sites	30
3.1.1	Churchill Site	30
3.1.2	Baker Lake Site	33
3.1.3	Inuvik Site	33
3.1.4	Lena Delta Site	36
3.2	Data Processing	38

3.3	Data Analysis	40
3.3.1	Churchill Site	40
3.3.2	Baker Lake Site	44
3.3.3	Inuvik Site	46
3.3.4	Lena Delta Site	48
4	Random Rough Surface Scattering	51
4.1	Surface Properties	51
4.1.1	Physical Properties	52
4.1.2	Geometrical Properties	53
4.2	Surface Modelling	55
4.2.1	Coherent Component (Specular Reflection and Transmission)	56
4.2.2	Incoherently Scattered Component	57
4.3	Small Perturbation Model (Bragg Surface Scattering)	58
4.4	X-Bragg Model	60
5	Particle and Volume Scattering	63
5.1	Scattering of a Single Particle	63
5.2	Rayleigh Scattering	65
5.2.1	Sphere Shaped Particle	66
5.2.2	Dipole Shaped Particle	68
5.2.3	Ellipsoid Shaped Particle	70
5.3	Mie Scattering	72
5.3.1	Sphere Shaped Particle	73
5.3.2	Dipole Shaped Particle	73
5.3.3	Ellipsoid Shaped Particle	74
5.4	Coherency Matrix for a Cloud of Particles	75
6	Multiple Scattering (Dihedral Backscattering)	79
6.1	Sphere Shaped Particles	80
6.2	Dipole Shaped Particles	82
6.2.1	Short Dipole	84
6.2.2	Long Dipole	86
6.3	Ellipsoid Shaped Particles	88
6.4	Coherency Matrix for a Dihedral of a Cloud of Particles and a Subsurface	91
7	Two-Layer Structure Ice–Subsurface	95
7.1	Model equation	96
7.2	Scenario Simulation	97

7.2.1	Combination of Volume and Dihedral Backscattering	98
7.2.2	Subsurface, Volume and Dihedral Backscattering Combination	100
7.3	Data Interpretation	103
7.3.1	Churchill site	103
7.3.2	Baker Lake site	106
7.3.3	Inuvik site	111
7.3.4	Lena Delta site	115
7.4	Data Representation	118
7.4.1	Churchill site	120
7.4.2	Baker Lake site	126
7.4.3	Inuvik site	127
7.4.4	Lena Delta site	128
8	Conclusion	131
	Bibliography	137
A	Nomenclature	149
B	Derivation of the dipole scattering matrix	153

Chapter 1

Introduction

Methane (CH_4) is a potent greenhouse gas, which traps heat far more powerfully than (CO_2). Its atmospheric concentration has risen by 1 % per year [74] over the last century. The reasons for this trend are not completely understood since the sources and sinks of methane on a global scale are today inaccurately quantified.

Methane is produced from the degradation of organic materials in the absence of oxygen and is released into the atmosphere from both natural and human sources. One of the natural sources of methane is in the cryosphere, as the carbon that is stored in the permafrost is in the form of peat and methane. When climate warms, permafrost thaws and releases methane to the atmosphere through microbial processes. Methane release induces warming, causing more gas release and further warming.

Thermokarst lakes are bodies of freshwater, usually shallow, that are formed as ice-rich permafrost thaws. These lakes are known to emit methane gas. However, the magnitude of these emissions remains uncertain since the principal emission mode (ebullition) is highly variable in space and time. Ebullition represents 50-95 % of lakes' methane emissions and increases the previous estimations of Northern wetlands methane fluxes, as shown in [96], by 10-63 %. This methane is imprecisely accounted for in climate change modelling [35].

During winter these lakes freeze and the methane bubbles are trapped in the lake ice, such that the amount of the trapped methane is in correlation with ebullition. Quantitative monitoring of the trapped methane on a global scale can extend current climate models. Remote sensing achieved by satellite synthetic aperture radar (SAR) systems at low Earth orbits provides periodically global coverage observations of the northern wetlands. Therefore relating

SAR observations with the amount of trapped methane is an essential step in evaluating ebullition.

The analysis of SAR data acquired by RADARSAT-1 (C-band) and ALOS-PALSAR (L-band) over thermokarst lakes showed that the backscattering from methane bubbles becomes visible in the SAR image implying that SAR may have a role in evaluating methane ebullition. In [97] a correlation between the backscattered power measured by RADARSAT-1 with field survey data for a percentage of lake ice with bubbles and for point-source ebullition has been observed. The results show a better correlation in the early winter acquisition, and also at steeper look angles. Similar relations are shown in [25]. However, relations based on observations are not sufficient for quantitative evaluation of methane bubbles ebullition, as they cannot account for the varying conditions that can occur over different areas and times, such as the dependency of the observation on the material under the ice. In addition, finding the optimum measurement system (e.g. optimum look angle and/or frequency) is harder when relying on observations rather than relying on a model. Therefore an adequate modelling of the backscattering is required.

In this work I establish a model for the polarimetric backscattering of frozen shallow subarctic lakes, which are frozen usually up to two meters depth during winter, as shown schematically in Fig. 1.1. The model takes into account the inhomogeneities in the ice layer introduced mainly by trapped methane bubbles. The electromagnetic waves at lower frequencies are expected to penetrate into the ice volume, interact with the trapped bubbles, and finally reach the interface between the ice and the subsurface, such that considerable backscattering from bubbles, subsurface and their mutual interaction is expected.

The scattering from the bubbles depends strongly on the nature and shape of the bubbles for a certain frequency and direction of the incident electromagnetic wave. Several studies report inhomogeneities within the ice layer specially caused by methane bubbles. A brief description of the inhomogeneities is given in the next section of this chapter.

Any scattering model for the evaluation of methane bubbles trapped in the ice lake should be able to account for the variety of possible scenarios such as floating and grounded ice. Changes in the experimented backscattered power under different lake conditions are summarized in Section 1.2.

Some observations of the polarimetric backscattering from the subarctic lakes within the last decade are presented in Section 1.3. However current models cannot accurately explain the relation of the co-polarisation ratio with the presence of floating ice. Therefore the changes in the backscattering under different conditions are not yet predictable.

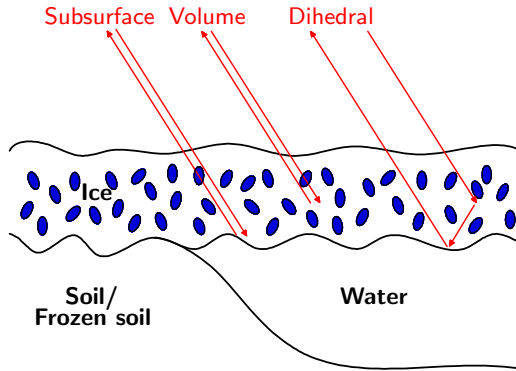


Figure 1.1 The Scattering mechanisms considered in the model of shallow subarctic lakes

As the derived model is compared to fully polarimetric L-Band data obtained by the ALOS-PALSAR sensor, Section 1.4 includes a short summary about ALOS-PALSAR instrument in the polarimetric mode.

1.1 Ice Inhomogeneities and Methane Bubbles

Observation of inhomogeneities within ice cores from arctic lake ice have been done in [25] and [47]. The authors describe several shapes of bubbles and crystals in ice cores with a diameter of 10 cm obtained in a region east of Churchill, Manitoba. It is reported in [25] that different types of inhomogeneity exist within the ice without explicitly mentioning their size. They are mainly elongated tubular (cylindrical) bubbles oriented normal to the ice surface. Beside them, tiny spherical bubbles, spherical and sub-spherical (teardrop-like) bubbles were also observed. In addition to the bubbles, crystals are mentioned, where some of them are congelation crystals with horizontal c -axes and others massive crystals with vertically oriented c -axes. Along the c -axis (crystalline axis), the light can pass unhindered through the crystal. The author also explains that a strong radar backscattering can occur due to large spherical (ebullition) bubbles, often created by methane released from the lake sediment. In [47] the ice formation for water freezing on the bottom of the initial layer is described. The ice crystals grow downward into the water with two different orientations of the c -axes. One has horizontally oriented c -axis and the other has vertically oriented c -axis, but regardless of the c -axes orientation both types generate vertically elongated crystals. In [98], it is demonstrated that emission of methane associated with thawing produces dissolved methane in lake water, which ap-

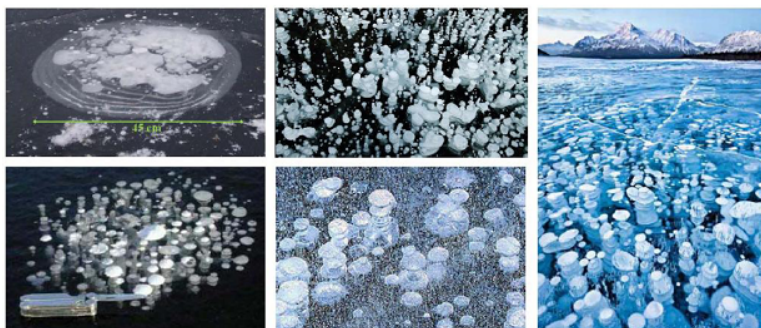


Figure 1.2 Methane bubbles trapped in lake ice, images obtained from [27] and [31]

pears as densely-packed, vertically oriented tabular bubbles in ice. The density increases when the ice thickness increases for shallow lakes.

More recent observations of high methane emission lakes describe methane bubbles in more detail [27], and relate the methane emission rate to "the point source classification", as the methane bubbles form different structures depending on the emission rate. According to [27], the structures can be isolated bubbles trapped between multiple ice layers above each other, merged in multiple layers, merged in one single big pocket or untrapped rising from open holes in the ice most of the year. In the mentioned publication, methane bubbles are described as tiny bubble tubes (< 2 cm diameter) generated at the sediment layer in the hotspots, where the methane is produced in a larger volume.

In general, bubbles rise constantly from the sediment at the bottom of the lake. The ice is formed layer by layer (night after night) and the bubbles that rise get trapped in the newly formed layer of ice, generating the column shape structure. This formation and these bubble shapes, shown in Fig. 1.2, are approximated by vertically oriented ellipsoids in this work, in order to evaluate its backscattering to the side-looking SAR.

Permittivity of methane is almost similar to air. In spite of the small permittivity, methane bubbles can still play a significant role in the backscattering which is more dependent on the bubble size than on the material permittivity, as will be discussed later in Chapter 5.

1.2 Subarctic Lakes

The subarctic land is mostly covered by lakes, and most of them are shallow. The lakes usually melt completely during summer. During winter, ice of ap-

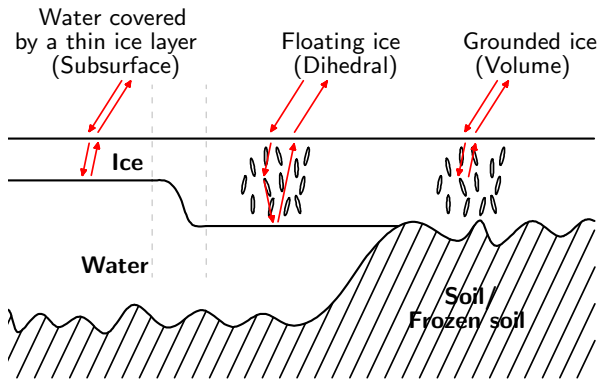


Figure 1.3 Scattering scenarios in thermokarst lakes during winter

proximately one meter depth is formed with a snow cover, which typically does not exceed 50 cm, above it [28]. Many publications had already reported about observations of subarctic lake ice using a radar/SAR system [24], [22], [23], [25], [21], [46], [48], [49], [68], [47], [102], [100], [101], which is different from the ice observed at glaciers [87], [79], where ice thickness exceeds the penetration depth [17]. For some lakes, ice freezes to the lake bed and forms grounded ice, while for deeper lakes, fresh water exists all year long and only floating ice is generated during winter, see Fig. 1.3. The changes in the dielectric properties of the material under the ice and the inhomogeneities within it influence the backscattered power to the SAR system. Many publications report on changes in the backscattered power from the lakes during different times of the year. In summer, most of the incident electromagnetic wave is reflected on the smooth lake surface away from the receiver of a monostatic system resulting in a low backscattered power, such that the lake appears dark in the radar image. When floating ice is formed, the backscattered power increases dramatically (around 10 dB at C-band), due to the contribution of the scattering from the ice inhomogeneities that are reflected back on the ice-water interface [25]. The backscattered power is lower when the water freezes to the bed, since the reflection from the ice-water interface is replaced by the one from ice-lakebed, whose permittivity contrast is lower, and leads to a lower reflection from this interface. A low power backscattered from the lakes' borders, due to the lower depth of the lake bed that forms grounded ice during winter, is reported in the literature [49] [51].

1.3 Polarimetric SAR: State of the Art

SAR observations of the lake ice addressed in the previous section are based on the evaluation of the amplitude of the backscattered signal. However there are several works developed within the last two decades addressing the relative ratios between different polarisations. Polarimetric observations allow better quantitative estimations because the observed polarimetric signatures depend strongly on the actual scattering process. In comparison to conventional single-channel SAR, SAR polarimetry can lead to a significant improvement in the quality of data analysis [59].

One of the earliest observations of the polarimetric SAR backscattering from frozen lakes is reported in [71]. The data were acquired over the Great Lakes at C-band with incident angles up to 60° . The data show a higher horizontal than vertical backscattering and low co-polarisation coherence during ice presence. The polarimetric SAR data set were useful for the development of ice mapping algorithms; the maps were in good agreement with the ice charts of the National Ice Center (NIC) [60]. A higher ratio of horizontally to vertically polarised backscattering and the lower co-polarisation coherency during ice presence on Mackenzie River near Inuvik is also reported in [93]. The co-polarisation backscattering ratio is addressed even clearer in [36] and proved to be related to the presence of floating ice, where the results are based on observations.

Current models of the backscattering from a two-layer structure could not explain the observed co-polarisation ratio and its dependency on ice presence. The model presented in [37] predicts a higher vertical than horizontal backscattering with a difference that increases for larger ice thickness. The publication mentions the backscattering from the interactions of the volume within the upper layer and the boundary between the two-layers, but this backscattering contribution is not considered in the model. In [99], a model for the polarimetric backscattering from a two-layer structure is presented. The backscattering from the interaction between the volume in the upper layer and the surface in the lower layer were neglected here as well. The model was compared with data obtained by the PALSAR sensor over permafrost regions in Alaska. Despite that the model could explain the trend in the cross-polarisation channels, it predicts a lower horizontal to vertical backscattering ratio than the observed data.

Statistical parameters extracted from the polarimetric backscattering allow a discrimination of different types of scattering mechanisms and a better evaluation of the polarimetric signature. The polarimetric entropy-alpha parameters proposed in [16] are statistical parameters that are considered, because of their capabilities in interpreting the backscattering mechanism as will be seen in

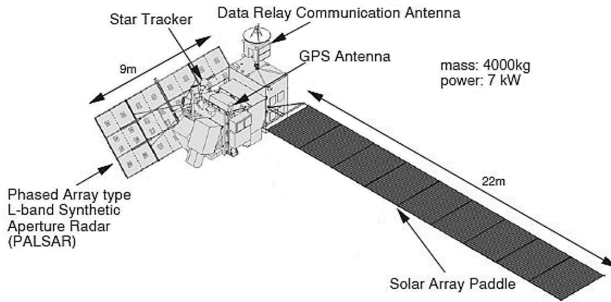


Figure 1.4 Schematic illustration of the ALOS spacecraft (image credit: JAXA)

Chapter 2. Evaluation of the entropy-alpha values observed over a two-layer structure of ice and fresh water was recently shown in [92], without providing an interpretation of the entropy-alpha trends.

Modelling the polarimetric backscattering, while considering second order scattering mechanisms, is essential for explaining the polarimetric signature. The importance of these scattering mechanisms has also been noted in [58], where mathematically based approaches are established to represent them. Nevertheless the electromagnetic theory behind these scattering processes has to be addressed for a more realistic and interpretable approach. Therefore the main focus of this study is to establish a scattering model with second order scattering mechanisms for the shallow subarctic lakes that can explain the entropy-alpha values and the co-polarisation ratio observed by a fully polarimetric sensor such as ALOS-PALSAR.

1.4 ALOS-PALSAR System

The Advanced Land Observing Satellite (ALOS) [45] was launched by the Japanese Aerospace Exploration Agency (JAXA) in 2006. The satellite observed most of the land surface in a systematic way until 2011, when the mission ended.

One of the main objectives of ALOS was to enable land observations with the *Phased Array type L-band Synthetic Aperture Radar (PALSAR)*. The PALSAR instrument, shown in Fig. 1.4, was capable of acquiring fully polarimetric images, when it was operated in the polarimetric mode. This mode was operated during ascending passes every second years and covered most of the Northern subarctic region. The look angle used in this operation mode is 21.5° or 23.1° ,

Central Frequency	1270MHz (L-band)
Chirp bandwidth	14MHz
Polarisation	HH + HV + VV + VH
Incidence angle	8 – 30°
Range Resolution	24 to 89m
Observation Swath	20 to 65km
Bit quantization (BAQ)	3 or 5 bits
Data rate	240Mbps
Noise-equivalent sigma-zero (NESZ)	-29dB
Signal-to-ambiguity ratio	19dB

Table 1.1 Parameters of PALSAR Polarimetric Mode [72]

while the achieved resolution is 24 m in range, and 5 m for single look in the azimuth. The system covers a 30 km swath width in this mode. All further parameters of ALOS-PALSAR are summarised in Tab. 1.1.

1.5 Objectives and Scope of the Work

The detailed information about the steps of building a scattering model for the shallow subarctic lakes and the comparison with ALOS-PALSAR data are presented in the following chapters. Below is a short summary of the contents of each chapter, followed by a presentation of the main points addressed in the thesis.

In Chapter 2, the basics of scattering concepts for fully polarimetric synthetic aperture radar are described, where the included information is essential for the understanding of the model development and evaluation. In this chapter, the requirement of coherency and the covariance matrix to describe the distributed scatterers is clarified, and two decomposition concepts (eigen decomposition and model-based decomposition) are presented.

The available test sites for this study are the Churchill, Baker Lake, Inuvik, and Lena Delta regions. Their Pauli images and first analyses of the lakes' samples are included in Chapter 3.

Chapter 4 describes the properties of a surface and the dependencies of a suitable surface model on those properties. The coherent component (reflected / transmitted) and the incoherent component (scattered) of the electromagnetic wave impinging a surface are discussed. Bragg and X-Bragg models [40] are used in modelling the subsurface scattering under the ice cover and a closer look at these models is performed.

The volume scattering from particles of ellipsoidal shape and its mathematical model are introduced in Chapter 5. In order to better understand the

scattering from a volume of ellipsoids, as a first step the volume scattering from spherical and dipole shaped particles is introduced. The chapter introduces the general equations of the scattering from an ellipsoid and a volume of ellipsoids, that can be adapted for bistatic cases and also for obtaining the scattering from a volume of particles reflected back by the subsurface (dihedral of volume and subsurface), which is done in Chapter 6. The volume scattering model in this chapter is used to model methane bubbles in the ice layer of the subarctic lakes.

Chapter 6 introduces the dihedral scattering from the interaction of volume and subsurface. The model presented in this chapter is used to estimate the scattering from the volume of methane bubbles that is reflected back by the subsurface interface (ice-water/soil).

The complete model with the clarified subsurface, volume and dihedral scattering of the previous chapters is presented in Chapter 7 with several scenarios that include different lake conditions. The results are compared with ALOS data, which allow the interpretation of the data. Then based on those results a colour scheme is proposed and colour coded maps which visualise the data interpretation are shown. A summary of achievements, and conclusions based on the comparison between the simulated and measured data are drawn in Chapter 8. In addition further investigations to improve the retrieval of information about the subarctic lakes with methane bubbles and applicability to other scenarios are suggested in this last chapter.

The work presented within the eight chapters establishes a novel understanding of the electromagnetic theory in relation to the polarimetric backscattering from a two-layer structure measured by a side-looking SAR system. The two-layer structure for the case addressed in this study is set up by a surface and a volume above it.

To achieve this, several issues are addressed:

- The dihedral backscattering from a volume reflected by a subsurface is well known and had been considered in a variety of applications, but its polarimetric backscattering for the application of side-looking synthetic aperture radar had not been considered in an analytical approach, that coherently adds the backscattering from the two paths (surface – particle and particle – surface) so far. Therefore this scattering mechanism is studied in detail in this work.
- Within the scope of this work, basic expressions for the scattering from a single particle within a volume and from the interaction of the single particle with the subsurface are derived. A method to obtain the backscattering from the volume and the interaction between volume and

subsurface is presented, and dedicated processing functions are developed for this purpose.

- It is shown that the new approach of combining the volume backscattering with the dihedral of volume-subsurface backscattering can open many new possibilities for a novel understanding and interpreting of the backscattered polarimetric signature.
- Applying the newly developed forward model to a two-layer structure of frozen lakes shows a remarkable agreement with fully polarimetric L-band experimental data acquired by the ALOS-PALSAR sensor over the Northern subarctic region. The model can explain temporal changes and can successfully distinguish between different physical properties of a lake, such as lakes with grounded ice versus lakes with floating ice. This is the first known approach of using the polarimetric information based on a model to separate lakes with grounded ice and floating ice without exploiting the absolute backscattered power of the lake.
- The comparison of the experimental data and the forward model leads to a power independent colour scheme. Accordingly, maps of ALOS-PALSAR acquisitions are generated where a closer look at the individual lakes are provided. The conclusions obtained from these colour coded maps are in agreement with the results of the previous comparison.

Chapter 2

Polarimetric SAR Principles

Over the last five decades, SAR has been evolved to a very powerful remote sensing tool for monitoring the planet Earth. It has been used extensively for mapping biological and geological structures and features.

The translation of the measured data into information about the temporal or spatial changes within the observed scene and changes in the physical or spatial properties of the scatterers is an important task to evaluate the usability of microwave remote sensing. In many cases, the backscattered power alone had proved to be insufficient to extract this information accurately, therefore polarimetric measurements for the backscattering had been implemented, as the polarimetric signatures depend strongly on the actual scattering process [43]. Therefore polarimetric SAR data are considered in this work and a brief introduction of polarimetric SAR is discussed in this chapter.

In order to understand polarimetric SAR, the polarimetric scattering matrix for objects will be presented in the first part of this chapter. Since most natural scenes consist of distributed scatterers, statistical quantities of the scattering matrix, covariance and coherency matrix particularly, are more suitable for describing them [59]. These matrices will be introduced and discussed in the second part of this chapter.

Natural scenes are usually covered by forest/vegetation, by snow and ice in cold regions, and by dunes in desert. Therefore, the backscattering will usually not only correspond to a pure surface scattering, but also to the scattering from the covering volume. Several concepts to decompose the polarimetric backscattering into individual components have been developed [11], and two of the most powerful and commonly used are presented in the last part of this chapter.

2.1 Polarimetric Scattering Matrix

The temporal changes of the electric or magnetic field cause spatial changes in the magnetic or electric field respectively. These relationships have been described by Maxwell's equations. According to these equations, a source that generates temporal electric field changes $\partial E/\partial t$, will induce a magnetic field $\nabla \times H$ that is spatially perpendicular to the electric field which, in turn, induces a changing electric field perpendicular to the magnetic field which will further generate a magnetic field resulting in a propagating electromagnetic wave.

When the source of the electromagnetic wave is relatively far from the observed scene and the considered resolution cell, then the wave is travelling in parallel directions generating surfaces of constant phase, which is a so called plane wave.

The electric field of the plane electromagnetic wave is described by the wave equation shown in Eq. (2.1), which is derived from Maxwell's equation assuming a source free propagation medium with a permittivity equal to ϵ and permeability of μ .

$$\nabla^2 E = \mu\epsilon \frac{\partial^2 E}{\partial t^2} \quad (2.1)$$

The solution of this equation for the electric field is described by

$$E(r, t) = E_0 e^{j(\frac{2\pi}{\lambda} \cdot r + \omega t)}, \quad (2.2)$$

where r is the distance from the source. The electric field is perpendicular to the direction of the wave propagation.

When an electromagnetic wave propagates then its electric field vector must lay in the plane that is perpendicular on the Poynting vector, which corresponds to the direction of the wave propagation. Therefore two orthogonal basis in this plane are sufficient to describe the electric field, and hence the electromagnetic wave completely.

One of the commonly used orthogonal basis is the horizontal and vertical polarizations basis, where the electric field is described as follows

$$\vec{E}(r, t) = E_h(r, t)\vec{h} + E_v(r, t)\vec{v}. \quad (2.3)$$

Other orthogonal basis, such as left and right handed circular polarisation, are also used in certain applications, but the linear horizontal and vertical polarisations are considered in the following.

In this sense, the electric field is better described in a vector form, that corresponds to the orthogonal polarisations as

$$\vec{E} = \begin{bmatrix} E_h \\ E_v \end{bmatrix}. \quad (2.4)$$

The transmitted electromagnetic field interacts with the scatterers within the scene, such that the polarisation and the power of the scattered electromagnetic wave depend on the object's physical properties, such as dimension and permittivity in addition to its spatial properties, for example its orientation with respect to the incident wave.

The scattered electromagnetic wave can be described in the same basis as the incident wave, while the changes on the field induced by the scatterers in the resolution cell are described by the scattering matrix. The relation between the incident and scattered wave is shown in Eq. (2.5), where $[S]$ is the scattering matrix, the subscript "inc" corresponds to the incident wave and "obs" to the observed wave.

$$\begin{bmatrix} E_{h,obs} \\ E_{v,obs} \end{bmatrix} = \begin{bmatrix} S_{hh} & S_{hv} \\ S_{vh} & S_{vv} \end{bmatrix} \begin{bmatrix} E_{h,inc} \\ E_{v,inc} \end{bmatrix} \quad (2.5)$$

The diagonal elements in the scattering matrix describe the changes in the observed wave depending on the incident wave that has the same polarimetric basis as the observed wave, therefore they are called the co-polarisation scattering coefficients. The off-diagonal elements describe the relation of the observed wave with the incident wave of the orthogonal base, as part of the incident wave with a certain polarisation is transferred to the orthogonal polarisation in the scattering process, therefore the off-diagonal elements are known as the cross-polarisation scattering coefficients. In the monostatic case with transmitter and receiver collocated, which is the case considered in this work, the cross-polarisation components are identical $S_{vh} = S_{hv}$ for reciprocal scatterers [8]. The scattering matrix is vectorised in a lexicographic scattering vector [59]

$$\vec{k}_l = \begin{bmatrix} S_{hh} & \sqrt{2}S_{hv} & S_{vv} \end{bmatrix}^T. \quad (2.6)$$

2.2 Pauli Scattering Vector

With the scattering matrix, the influence of the scattering process on the field can be evaluated, but the physical interpretation of the scattering mechanisms can be better achieved by considering the Pauli combination between the scattering coefficients. The Pauli vector is another representation of the scattering coefficients, where the relative phase between the co-polarisations is clearer and better addressed.

The scattering Pauli vector for a monostatic case is written as [59]

$$\vec{k}_p = \frac{1}{\sqrt{2}} \begin{bmatrix} S_{hh} + S_{vv} & S_{hh} - S_{vv} & 2S_{hv} \end{bmatrix}^T. \quad (2.7)$$

The first element in the vector is usually dominant when a first order scattering is dominant in the resolution cell, as the co-polarisation components are usually in phase. The second element is dominant when the co-polarisation backscattering is out of phase, which usually occurs when the second order scattering is dominant, such as for the case of dihedral backscattering. The third term is dominant when the scatterer is rotated about the line of sight or when randomness is dominant in the resolution cell. Further details are discussed in the last part of this chapter. Hence polarimetric colour coded radar images are usually based on Pauli colour coding of the scattering coefficients, as a better interpretation of the images is achieved.

2.3 Radar Cross Section

For a single object, the radar equation gives a direct form for calculating the received power from the object. Eq. (2.8) is the radar equation for a monostatic radar case

$$P_r = \frac{P_t G^2 \lambda^2}{(4\pi)^3 R^4} \sigma. \quad (2.8)$$

The received power P_r depends on the transmitted power P_t , antenna gain G , wavelength λ , the distance between object and radar R , and the radar cross section (RCS) σ of the surface which is measured in units of m^2 .

From the radar equation, the RCS can be defined as the effective area of a perfectly and isotropically reflecting object that intercepts the transmitted radar power and then scatters that power back to the receiver. The RCS is calculated from the far field of the scattered and incident electric field \vec{E}_s , \vec{E}_i

$$\sigma = \lim_{r \rightarrow \infty} 4\pi r^2 \frac{|\vec{E}_s|^2}{|\vec{E}_i|^2}. \quad (2.9)$$

When an observed object, for example a surface observed by a SAR system, has a larger extent than the resolution cell, then the scattering is described with several scattering centres distributed in the resolution cell, where the distribution usually changes with time and space, as shown in Fig. 2.1b. Most of the natural scatterers like forest, vegetation and snow consist of a collection of statistically identical scatterers. For such cases Eq. (2.8) is not appropriate to calculate the received power for those scatterers, and it is necessary to integrate the total power over the illuminated area A_0 as

$$P_r = \iint_{A_0} \frac{P_t G^2 \lambda^2}{(4\pi)^3 R^4} \sigma^0 ds. \quad (2.10)$$

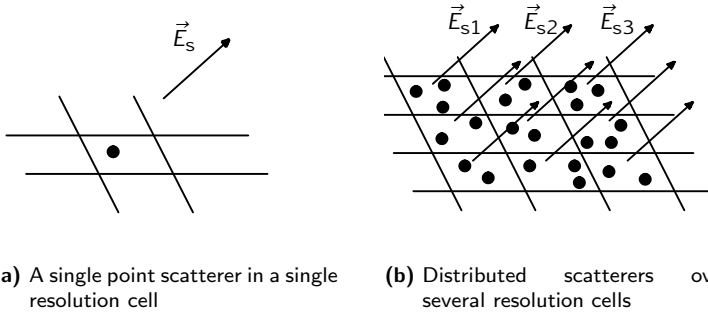


Figure 2.1 Illustration of scatterers type, where \vec{E}_{s1} , \vec{E}_{s2} , and \vec{E}_{s3} are the scattered electric fields of the corresponding realisation [59]

The term σ^0 is the average radar cross section of the statistically identical objects per unit area, and defined as [59]

$$\sigma^0 = \frac{\langle \sigma \rangle}{A_0} = \frac{4\pi r^2}{A_0} \frac{\langle |\vec{E}_s|^2 \rangle}{|\vec{E}_i|^2}. \quad (2.11)$$

Each radar cross section σ corresponds to the ratio of the total scattered power intensity from a certain resolution cell to the incident power intensity for a certain realisation. The total scattered electric field from this resolution cell E_s is obtained from the coherent superposition of backscattered signals from the multiple scatterers within the resolution cell, where each of them scatters the electromagnetic field with a different propagation phase depending on the scatterer's position. Therefore a different distribution of scatterers leads to a different backscattered power, such that the measured backscattered power fluctuates from one resolution cell to the next when a scene with distributed scatterers is considered. This phenomenon is known as speckle [67]. The statistical value of the scattering includes the information about the properties of the distributed scatterers.

Matrices that consider the average over the main power components and the correlation between them give a good description of the distributed scatterers. The matrices are usually averaged over space assuming a stochastic distribution where the temporal and spatial variations of the distribution are identical. The larger the averaging window, the better the estimation of the matrices as the random fluctuations (speckle noise) are reduced and the estimation of the matrix component has less variance and is closer to the mean.

A description of those matrices and their mathematical derivation is discussed in the following subsections, according to the definitions presented in [59].

2.3.1 Covariance Matrix

The scattering matrix completely describes the scattering from a single scatterer, but it is insufficient to describe the scattering from a set of scatterers with different shapes and orientations located within a single resolution cell, such as for natural scenes. Statistically based matrices are required for the full description of such cases.

From the lexicographic scattering vector shown in Eq. (2.6), the lexicographic covariance matrix C_3 is generated by computing the outer product of the vector with its conjugate transpose

$$C_3 = \langle \vec{k}_l \cdot \vec{k}_l^H \rangle = \begin{bmatrix} \langle |S_{hh}|^2 \rangle & \sqrt{2} \langle S_{hh} S_{hv}^* \rangle & \langle S_{hh} S_{vv}^* \rangle \\ \sqrt{2} \langle S_{hv} S_{hh}^* \rangle & 2 \langle |S_{hv}|^2 \rangle & \sqrt{2} \langle S_{hv} S_{vv}^* \rangle \\ \langle S_{vv} S_{hh}^* \rangle & \sqrt{2} \langle S_{vv} S_{hv}^* \rangle & \langle |S_{vv}|^2 \rangle \end{bmatrix}. \quad (2.12)$$

The diagonal elements of the matrix correspond to the power in each polarimetric channel, the off-diagonal elements are the correlation between those polarimetric components.

2.3.2 Coherency Matrix

The coherency matrix is generated from the outer product of the Pauli vector shown in Eq. (2.7), with its conjugate transpose

$$T_3 = \langle \vec{k}_p \cdot \vec{k}_p^H \rangle = \frac{1}{2} \begin{bmatrix} \langle |S_{hh} + S_{vv}|^2 \rangle & \langle (S_{hh} + S_{vv})(S_{hh} - S_{vv})^* \rangle & 2 \langle (S_{hh} + S_{vv}) S_{hv}^* \rangle \\ \langle (S_{hh} - S_{vv})(S_{hh} + S_{vv})^* \rangle & \langle |S_{hh} - S_{vv}|^2 \rangle & 2 \langle (S_{hh} - S_{vv}) S_{hv}^* \rangle \\ 2 \langle S_{hv} (S_{hh} + S_{vv})^* \rangle & 2 \langle S_{hv} (S_{hh} - S_{vv})^* \rangle & 4 \langle |S_{hv}|^2 \rangle \end{bmatrix}. \quad (2.13)$$

The diagonal elements represent the power of the Pauli elements while the off diagonal elements are given by the correlation between them. As already been discussed in Section 2.2 and further clarified in Section 2.5, a certain Pauli component dominates when a common scattering mechanism (surface, dihedral and volume) is dominating. Therefore, Pauli components can better interpret the scatterers than lexicographic components as the second one can better describe the impact of the scatterer on the wave. Hence the coherency

matrix has been used more often to describe the scatterers within the observed scene and in decomposing the scattering mechanisms.

Both covariance and coherency matrices are Hermitian positive semi-definite matrices which implies that they possess only real non-negative eigenvalues with orthogonal eigenvectors. Unique transformations from the covariance matrix to the coherency matrix and vice versa are shown in Eq. (2.14) and Eq. (2.15),

$$[C_3] = \begin{bmatrix} c_1 & c_2 & c_3 \\ c_2^* & c_4 & c_5 \\ c_3^* & c_5^* & c_6 \end{bmatrix}, \quad (2.14)$$

$$[T_3] = \frac{1}{2} \begin{bmatrix} c_1 + c_6 + c_3^* + c_3 & c_1 - c_6 + c_3^* - c_3 & \sqrt{2}(c_2 + c_5^*) \\ c_1 - c_6 - c_3^* + c_3 & c_1 + c_6 - c_3^* - c_3 & \sqrt{2}(c_2 - c_5^*) \\ \sqrt{2}(c_2^* + c_5) & \sqrt{2}(c_2^* - c_5) & 2c_4 \end{bmatrix},$$

$$[T_3] = \begin{bmatrix} t_1 & t_2 & t_3 \\ t_2^* & t_4 & t_5 \\ t_3^* & t_5^* & t_6 \end{bmatrix}, \quad (2.15)$$

$$[C_3] = \frac{1}{2} \begin{bmatrix} t_1 + t_4 + t_2^* + t_2 & \sqrt{2}(t_3 + t_5) & t_1 - t_4 + t_2^* - t_2 \\ \sqrt{2}(t_3^* + t_5^*) & 2t_6 & \sqrt{2}(t_3^* - t_5^*) \\ t_1 - t_4 - t_2^* + t_2 & \sqrt{2}(t_3 - t_5) & t_1 + t_4 - t_2^* - t_2 \end{bmatrix}.$$

Both covariance and coherency matrices consist of three real values in the diagonal and three off-diagonal complex values with their conjugate in the symmetric places, such that the matrices include nine degrees of freedom instead of five for the scattering matrix shown in Eq. (2.5).

2.4 Eigen Decomposition

Most of the observed scenes include more than one scattering mechanism within the resolution cell and the radar measures the cumulative backscattering of them all. In order to extract physical information about the scattering process from polarimetric information, several decomposition algorithms of the backscatter have been proposed during the last decades. In every decomposition algorithm, several assumptions have been considered because of the large number of unknowns compared to the dimensions of the observable space.

Eigen decomposition of the coherency matrix, proposed in [16], is an effective technique to decompose a maximum of three scattering mechanisms where each can be fully represented with a single scattering matrix and is polarimetrically orthogonal to the others. The decomposition provides polarimetric parameters (entropy, anisotropy and mean alpha angle) that can be used to interpret the

scattering mechanisms even if they are not completely orthogonal or more than three scattering mechanisms existing within the observed cell. The parameters can also separate certain physical effects from each other as some of them can be independent of part of the physical parameters, for example separating the permittivity of a surface from the roughness influence [41].

Solving the eigen problem for the coherency matrix is equivalent to rotating the scattering mechanism to its symmetry axis such that it corresponds to one eigenvalue. Since the matrix is hermitian positive semi-definite, then the eigenvalue is non-negative and real, such that it represents the mechanism's backscattered power. The mechanism itself is described by the eigenvector, as shown in Eq. (2.16). The coherency matrix is usually of $\text{rank}(T) = 3$, but it can have a lower rank. When a single scattering mechanism exists within the observed resolution cell then the coherency matrix is of $\text{rank}(T) = 1$ [11].

$$[T_3] = [U_3] \begin{bmatrix} \lambda_1 & 0 & 0 \\ 0 & \lambda_2 & 0 \\ 0 & 0 & \lambda_3 \end{bmatrix} [U_3]^{-1}. \quad (2.16)$$

The matrix $[U_3]$ in Eq. (2.16) contains the eigenvectors of the coherency matrix that are associated with the scattering mechanisms as shown in the following equation

$$[U_3] = [\underline{u}_1 \quad \underline{u}_2 \quad \underline{u}_3], \quad (2.17)$$

$$\underline{u}_i = [\cos \alpha_i e^{j\phi_{1,i}} \quad \sin \alpha_i \cos \beta_i e^{j\phi_{2,i}} \quad \sin \alpha_i \sin \beta_i e^{j\phi_{3,i}}]^T.$$

The value of α represents the type of the scattering mechanism independent of its rotation, β is the rotation angle around the line of sight (LOS) and ϕ describes the scattering phase angle which accounts for the phase relations between the elements of the vector. The alpha value can lie between 0° and 90° depending on the co-polarisation ratio backscattered from the mechanism after rotating it to be symmetric around the line of sight. The alpha value is close to zero when S_{hh} and S_{vv} are almost equal and in phase like in the case of the backscattering from a surface, while it is close to 90° when S_{hh} and S_{vv} are almost equal but out of phase as for the case of the backscattering from a dihedral. When one of the polarisation components is dominant over the other, the alpha angle is close to 45° similar to the case of the backscattering from a dipole since it can be rotated to backscatter S_{hh} or S_{vv} while the other co-polarisation component is zero, see Fig. 2.2.

The rotation angle of the object around the LOS ($\beta_i/2$) is zero or $180^\circ/2$ when the object is symmetric around the line of sight. The symmetric object has a zero cross-polarisation backscattering which can also be observed

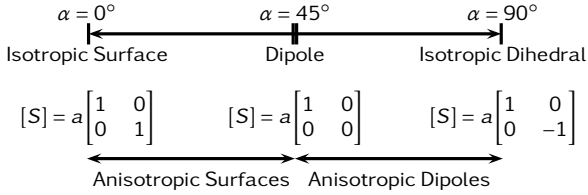


Figure 2.2 Alpha angle interpretation [11]

from Eq. (2.17). When an object is rotated around the LOS, its backscattering will contribute with a cross-polarisation component that is correlated to the co-polarisation component. This happens because part of the horizontal and vertical incident power is transferred to the other channel by the scattering process for the rotated scatterer. Later in this work, backscattering from shallow subarctic lakes is considered and the lake surface is symmetric and horizontally oriented independently from the topography such that the cross and co-polarisation channels are expected to be completely uncorrelated [11].

In the same way since most of the natural fields are flat and a symmetric distribution of scatterers above it is a realistic assumption, a zero correlation between cross- and co-polarimetric channel is common. This is the main assumption included in model-based decomposition, as will be seen in Section 2.5.

2.4.1 Polarimetric Entropy, Anisotropy and Mean Alpha Angle

There are three main polarimetric parameters obtained from the eigen decomposition algorithm which can effectively describe physical features. The parameters are extracted from the eigenvalues and eigenvectors. The first one is the polarimetric scattering entropy H which is shown in Eq. (2.18), where P_i corresponds to the appearance probability for each of the decomposed scattering mechanisms. When one of the scattering mechanisms is dominant then its probability is close to one while the other mechanisms have an almost zero probability resulting in an entropy value close to zero. On the other hand, the entropy is maximized and equal to one when the probabilities of all the

mechanisms are equal which means they are $P_i = 1/3$. In general, the entropy describes the dominance of one scattering mechanism over the other.

$$H = \sum_{i=1}^3 P_i \log_3 \frac{1}{P_i} \quad (2.18)$$

The appearance probability of a single scattering mechanism is equivalent to its power contribution normalised to the total backscattered power. Therefore, the probabilities are calculated from the eigenvalues by evaluating

$$P_i = \frac{\lambda_i}{\lambda_1 + \lambda_2 + \lambda_3}. \quad (2.19)$$

The second parameter is the polarimetric scattering anisotropy. It describes the relative dominance of the second most dominant scattering mechanism over the third one. As can be seen from Eq. (2.20) an anisotropy value of 1 corresponds to a highly dominating second scattering mechanism over the third and zero anisotropy corresponding to an equal contributions from second and third scattering mechanism

$$A = \frac{\lambda_2 - \lambda_3}{\lambda_2 + \lambda_3}. \quad (2.20)$$

The mean alpha angle is the third main polarimetric parameter obtained from the eigen decomposition. As discussed in Section 2.4 the value of alpha for a single scattering mechanism is easily related to the physics behind the scattering mechanism. The mean alpha angle is calculated from the probability weighted average of the alpha values for each scattering mechanism, as shown in the following equation

$$\alpha = P_1 \alpha_1 + P_2 \alpha_2 + P_3 \alpha_3. \quad (2.21)$$

The mean alpha value, henceforth simply called alpha, describes the average of the type of the scattering mechanisms within the observed resolution cell.

2.4.2 Entropy-Alpha Histogram

The polarimetric parameters introduced in the previous section are combined together to describe the backscattering from the scene. An effective method of interpreting the scatterers and classifying them is to observe the two dimensional distribution of the measured entropy and alpha. The algorithm had been proposed in [16]. It is based on the idea that the entropy rises when the degree of statistical disorder increases, which is an indicator of the natural influence within the observed scene, and alpha can be used to identify the average underlying scattering mechanism.

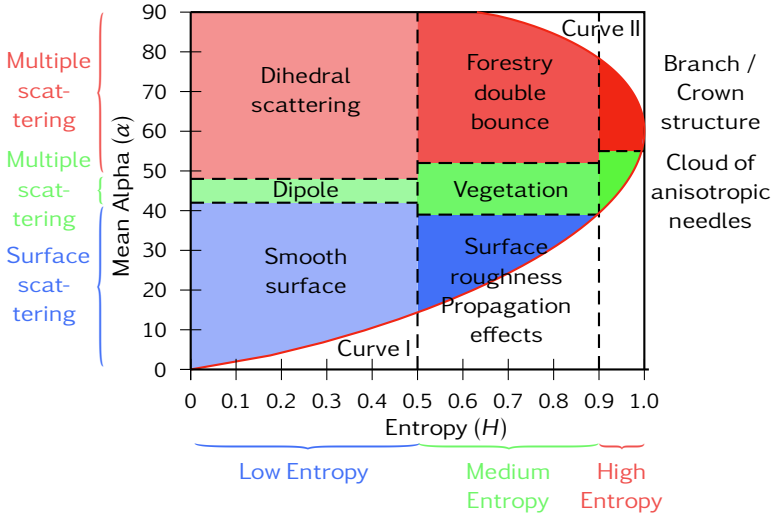


Figure 2.3 Entropy alpha classification proposed in [8] and [16]

The entropy-alpha plane has a certain feasible region, defined mathematically and not physically due to the eigen decomposition. The two curves (curve I and curve II) shown in Fig. 2.3 specify the boundaries of maximum entropy for a certain alpha. The curves can be calculated from obtaining the entropy-alpha values of coherency matrices for extreme cases. The coherency matrices, which generate curve I and curve II are shown in Eq. (2.22), where the subscripts I and II correspond to the coherency matrix for curve I and II respectively.

$$\begin{aligned}
 [T]_{II} &= \begin{bmatrix} 1 & 0 & 0 \\ 0 & m & 0 \\ 0 & 0 & m \end{bmatrix}, & 0 \leq m \leq 1 \\
 [T]_{II,1} &= \begin{bmatrix} 0 & 0 & 0 \\ 0 & 1 & 0 \\ 0 & 0 & 2m \end{bmatrix}, & 0 \leq m \leq 0.5 \\
 [T]_{II,2} &= \begin{bmatrix} 2m-1 & 0 & 0 \\ 0 & 1 & 0 \\ 0 & 0 & 1 \end{bmatrix}, & 0.5 \leq m \leq 1
 \end{aligned} \tag{2.22}$$

From the feasibility region of the entropy-alpha plane, it can be seen that with increasing disorder, and hence entropy, the interpretation of the average

scattering mechanism type becomes more challenging as a very limited range of α is feasible.

For the example of L-band data at around 40° look angle the feasible region of the entropy-alpha plane can be divided into eight zones, which correspond to classes of different scattering behaviour [8]. The region of low entropy and low α is associated with pure surface scattering. Higher entropy with low α is associated with rougher surfaces as the roughness introduced extra randomness which increases the entropy. The zone of $\alpha = 45^\circ$ and low entropy corresponds to a volume of oriented dipoles. When the volume of dipoles is partially oriented or random, then the entropy increases without a significant change in α as α depends on the type of scatterer (dipole) and not the orientation. The fourth zone of medium entropy and $\alpha = 45^\circ$ is reached for partially oriented volume of dipoles which can be observed in vegetated scenes. The zone of high entropy with $\alpha \approx 50^\circ$ is for scenes where several scattering mechanisms contribute all together within the resolution cell without the dominance of one over the other. Noise has an entropy = 1 and lays in this zone.

High values of α occur with the presence of conventional dihedrals which have both non-zero S_{hh} and S_{vv} values, and out of phase as will be discussed in Section 2.5.2. A low entropy, high α zone is for pure dihedral scattering, occurring mostly in urban areas. When other mechanisms take place while dihedral scattering is present and dominating then the entropy-alpha values are in the region of medium entropy and high α . Forest backscattering belongs to this zone since the dominant scattering mechanism is the dihedral one and the trees' canopy contributes with volume backscattering that increases the observed entropy. The final zone is the high entropy and high α region. This zone is associated with scenes where high randomness can be observed, nevertheless the presence of the dihedral scattering is still noticeable. The boundaries of this classification can change for different frequencies and look angles.

In this study, the model and scattering mechanisms considered in it are evaluated by mainly considering the entropy-alpha distribution of the simulated scenarios as will be explained in Chapters 5, 6, and 7. The data are also evaluated by the entropy-alpha histogram of the observed lake samples in addition to the anisotropy, power, coherencies, and other polarimetric ratios that will be presented in Chapters 3 and 7.

2.5 Model-Based Decomposition

The Model-Based decomposition, proposed in [32], considers three simple and primary scattering mechanisms. In this approach, the mechanisms are modelled and incoherently added such that the total coherency matrix is considered to be the cumulation of the three main contributions, using

$$[T] = [T_{\text{surface}}] + [T_{\text{dihedral}}] + [T_{\text{volume}}]. \quad (2.23)$$

Those three scattering process are: surface scattering, dihedral scattering and volume scattering. The coherency matrix of the surface and dihedral are usually of rank 1, while the volume matrix is a rank 3 matrix. The coherency matrix for each one, $[T_{\text{surface}}]$, $[T_{\text{dihedral}}]$ and $[T_{\text{volume}}]$, can be calculated as clarified in the following subsections.

Model-Based decomposition can separate between the scattering mechanisms even if they are depolarising and not orthogonal, but it requires pre-knowledge and assumptions about the physical property of the scattering component within the observed scene. This decomposition considers no rotation of the scattering component along the azimuth, such that the elements t_3 and t_5 of the coherency matrix in Eq. (2.15) are equal to zero, which has also been discussed in Section 2.4.

2.5.1 Surface Scattering Contribution

The first scattering is theoretically modelled by Bragg surface model. To simplify Bragg model only the first order Bragg equation is considered [90], such that no cross-polarisation backscattering is predicted. The horizontal R_h and vertical R_v scattering coefficients are presented in the following equation

$$[S_{\text{surface}}] = \begin{bmatrix} R_h & 0 \\ 0 & R_v \end{bmatrix}$$

$$R_h = \frac{\sqrt{\epsilon_{r1}} \cos \theta - \sqrt{\epsilon_{r2} - \epsilon_{r1} \sin^2 \theta}}{\sqrt{\epsilon_{r1}} \cos \theta + \sqrt{\epsilon_{r2} - \epsilon_{r1} \sin^2 \theta}} \quad (2.24)$$

$$R_v = (\epsilon_{r2} - \epsilon_{r1}) \frac{\epsilon_{r1} \sin^2 \theta - \epsilon_{r2}(1 + \sin^2 \theta)}{\left[\epsilon_{r2} \cos \theta + \sqrt{\epsilon_{r1}} \sqrt{\epsilon_{r2} - \epsilon_{r1} \sin^2 \theta} \right]^2}.$$

The scattering coefficients depend on the local incident angle θ , the relative permittivities of the first medium ϵ_{r1} and of the second medium ϵ_{r2} . The first medium's permittivity is usually smaller than the one of the second medium.

As can be concluded from the equations above, when only the real parts of the permittivities are considered, such that the imaginary parts of the permittivities

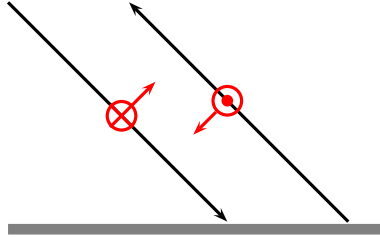


Figure 2.4 Bragg surface scattering mechanism

are low compared to the real parts, which is the usual case for soil and water both with low salt content, then both R_h and R_v are usually real and negative, such that a zero phase between the horizontal and vertical backscattering is expected, as shown in Fig. 2.4.

The coherency matrix of the surface is shown in Eq. (2.25), and it is a rank 1 matrix. The power contribution of the surface backscattering, which is embedded in P_{Surface} , is not modelled, but is usually obtained from the decomposition.

$$[T_{\text{Surface}}] = P_{\text{Surface}} \begin{bmatrix} 1 & \frac{R_h - R_v}{R_h + R_v} & 0 \\ \frac{R_h - R_v}{R_h + R_v} & \left(\frac{R_h - R_v}{R_h + R_v}\right)^2 & 0 \\ 0 & 0 & 0 \end{bmatrix} \quad (2.25)$$

Bragg surface model has proved to be a good estimation of backscattering for surfaces with low roughness and low correlation length [90]. The model has been extended to X-Bragg [41] to show even a better estimation of the surface backscattering behaviour combined with an increase in the model complexity as the surface matrix is extended to rank 3. The modelling of the surface backscattered power and the X-Bragg model will be discussed in Chapter 4.

2.5.2 Dihedral Scattering Contribution

The conventional dihedral scattering consists of two planes perpendicular to each other, such that the electromagnetic wave is reflected first on the first plane then on the second plane to propagate back to the transmitter, as shown in Fig. 2.5. The backscattering is obtained from the product of the specular

reflection on the first plane and the specular reflection on the second one, as follows

$$\begin{aligned}
 [S_{\text{Dih}}] &= \begin{bmatrix} S_{\text{hh,Dih}} & 0 \\ 0 & -S_{\text{vv,Dih}} \end{bmatrix} \\
 &= \zeta_{\text{Dih}} \begin{bmatrix} R_{\perp,\text{Surf1}}(\theta)R_{\perp,\text{Surf2}}\left(\frac{\pi}{2}-\theta\right) & 0 \\ 0 & -R_{\parallel,\text{Surf1}}(\theta)R_{\parallel,\text{Surf2}}\left(\frac{\pi}{2}-\theta\right) \end{bmatrix}.
 \end{aligned} \tag{2.26}$$

The negative sign included in the scattering matrix is due to the geometry, which leads to a horizontal and vertical backscattering that are out of phase, as shown in Fig. 2.5. The specular reflection is calculated from the Fresnel coefficients $R_{\perp,\text{Surf1}}$ and $R_{\perp,\text{Surf2}}$, where the subscript ‘‘Surf1’’ refers to the horizontal plane and ‘‘Surf2’’ refers to the vertical plane. By considering the SAR geometry, the vertical polarisation is usually the component of the electromagnetic wave that is parallel to the plane of incidence denoted by the subscript ‘‘||’’, and the horizontal polarisation is the component that is perpendicular to the plane of incidence and denoted by the subscript ‘‘⊥’’. The Fresnel coefficients are calculated as follows

$$\begin{aligned}
 R_{\perp,\text{Surface}}(\theta) &= \frac{\sqrt{\epsilon_{r1}} \cos \theta - \sqrt{\epsilon_{r,\text{Surface}} - \epsilon_{r1} \sin^2 \theta}}{\sqrt{\epsilon_{r1}} \cos \theta + \sqrt{\epsilon_{r,\text{Surface}} - \epsilon_{r1} \sin^2 \theta}}, \\
 R_{\parallel,\text{Surface}}(\theta) &= \frac{\epsilon_{r,\text{Surface}} \cos \theta - \sqrt{\epsilon_{r1} \epsilon_{r,\text{Surface}} - \epsilon_{r1}^2 \sin^2 \theta}}{\epsilon_{r,\text{Surface}} \cos \theta + \sqrt{\epsilon_{r1} \epsilon_{r,\text{Surface}} - \epsilon_{r1}^2 \sin^2 \theta}}.
 \end{aligned} \tag{2.27}$$

As can be seen in the equations above, the reflected horizontal component encounters a 180° phase shift, since usually the upper medium’s dielectric constant ϵ_{r1} is smaller than the lower medium’s dielectric constant $\epsilon_{r,\text{Surface}}$, while the vertical component is not shifted for local incident angles smaller than the Brewster angle. Further discussions about the reflection, transmission, and scattering of an electromagnetic wave impinging a surface will be presented later in Chapter 4.

The coherency matrix of the dihedral component is a rank 1 matrix. The power contribution of the dihedral backscattering, which is embedded in P_{Dih} , is obtained from the decomposition.

$$[T_{\text{Dih}}] = P_{\text{Dih}} \begin{bmatrix} \left(\frac{S_{\text{hh,Dih}} - S_{\text{vv,Dih}}}{S_{\text{hh,Dih}} + S_{\text{vv,Dih}}} \right)^2 & \frac{S_{\text{hh,Dih}} - S_{\text{vv,Dih}}}{S_{\text{hh,Dih}} + S_{\text{vv,Dih}}} & 0 \\ \frac{S_{\text{hh,Dih}} - S_{\text{vv,Dih}}}{S_{\text{hh,Dih}} + S_{\text{vv,Dih}}} & 1 & 0 \\ 0 & 0 & 0 \end{bmatrix} \tag{2.28}$$

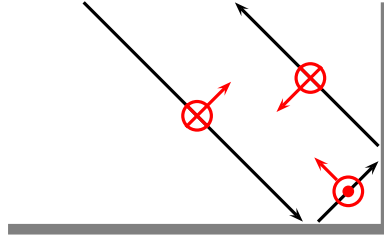


Figure 2.5 Dihedral scattering mechanism

The dihedral scattering mechanism is well observed in the polarimetric backscattered signature of buildings and trees, nevertheless this model-based decomposition has been considered on scenes where there is no clear presence of a physical dihedral structure. In these scenes the dihedral scattering mechanism is the simplest approximation of the second order scattering (multiple scattering) in vegetation and ice observations.

2.5.3 Volume Scattering Contribution

The third scattering process is a volume of randomly oriented dipoles, as shown in Fig. 2.6. This is a special case of a volume with ellipsoid shaped particles which is discussed in Chapter 5. The coherency matrix of this volume is as follows

$$[T_{\text{Volume}}] = R_{\text{Volume}} \begin{bmatrix} 2 & 0 & 0 \\ 0 & 1 & 0 \\ 0 & 0 & 1 \end{bmatrix}, \quad (2.29)$$

where R_{Volume} is the power contribution of the volume backscattering. The coherency matrix above is obtained from integrating over the backscattering from dipoles of different orientations. A detailed explanation on how to obtain the coherency matrix for a volume is presented in Chapter 5. The matrix is a rank 3 matrix, since the backscattering from each dipole is different from the others due to the different orientation.

In the model of Eq. (2.23), the number of observations is not sufficient for achieving a unique estimation of the unknowns. Therefore several assumptions are considered in practice. Nevertheless the three main contributions of surface, dihedral and volume scattering give a starting point for modelling, since each scattering process corresponds to a different polarimetric signature. Depending on the observed scenarios, some contributions can be directly taken into

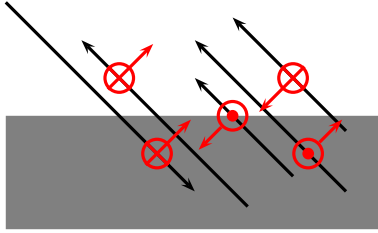


Figure 2.6 Volume scattering

account while others require more complex modelling or further propagation considerations.

Chapter 3

Experimental Data

The spaceborne ALOS-PALSAR system presented in Section 1.4 operates at L-Band with several modes. In this study, only the polarimetric mode is considered, where fully polarimetric (HH, VV, HV, VH) data have been acquired in an ascending orbit. ALOS had observed the subarctic region with this mode every two years within the mission lifetime (2007, 2009, and 2011).

Product level 1.1 for the polarimetric mode is available. At this level the data are compressed in range and a one look azimuth compression is performed. The data are stored as complex values, and the data represent azimuth and slant range measurements, where the phase history information is preserved. Each SAR image covers a swath width of 30 km and a length of 62 to 83 km with a resolution of around 25 m in range and 8 m in azimuth.

Test sites with prior knowledge have been considered in this study. The knowledge is obtained either by on-site measurements in the vicinity of the study area, or by publications that observed the lake's ice. In spite of the unavailability of information about the lake ice in a (freely accessible) website or publications, data over Lena delta site have also been analysed. This site is scientifically intriguing due to the high methane emissions, as described in [86], which is caused by the region's sensitivity to climate changes.

Areas located on the north coast of Alaska such as Barrow Lake and north coast of Canada have been avoided, because of a broadband, radio frequency interference induced by military over-the-horizon radar systems [20]. This interference cannot be corrected for level 1.1 ALOS products, and it limits the choice of test areas. Fig. 3.1 shows the locations of the four selected test sites for this study.



Figure 3.1 Considered test sites with data acquired by ALOS

3.1 Test Sites

All the test sites used in this study are located on the Northern subarctic region. The freezing cycle for the lakes in this region starts in October. In May, the ice reaches its maximum thickness, which is between one and two metres. Melting starts around June and in July the lakes are practically ice free. The depth of the subarctic lakes can vary between 1 m and 2.5 m. Lakes selected in this work have a minimum dimension larger than 2 km and do not exceed 7 km. The lakes had been visually chosen and a sample with a size of $400 \times 400 \text{ m}^2$ from the centre of the lake is considered, corresponding to around 20 independent looks in range and around 80 in azimuth dimension. The centre of the lakes is assumed to have a homogeneous ice thickness with a rather smooth and untilted ice water interface. In addition, the sediments are assumed to produce a flat lake bed, relevant for the case of grounded ice. Therefore the assumption of a flat terrain topography is reasonable, and the terrain topography has no impact on the polarimetric signature of the lake samples in the center of the lakes [3]. The available information about each site is summarised in the following subsections.

3.1.1 Churchill Site

This site has been used as a test site in a number of investigations about ice of shallow subarctic lakes. Ice cores from lakes in the region had been investigated, as mentioned in Section 1.1, in [25]. Radar observations with RADARSAT-1 (C-band) lead to remarkable conclusions regarding backscattered power difference

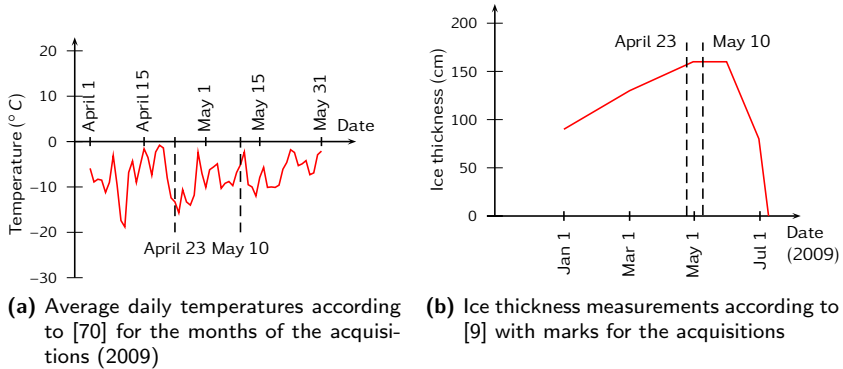
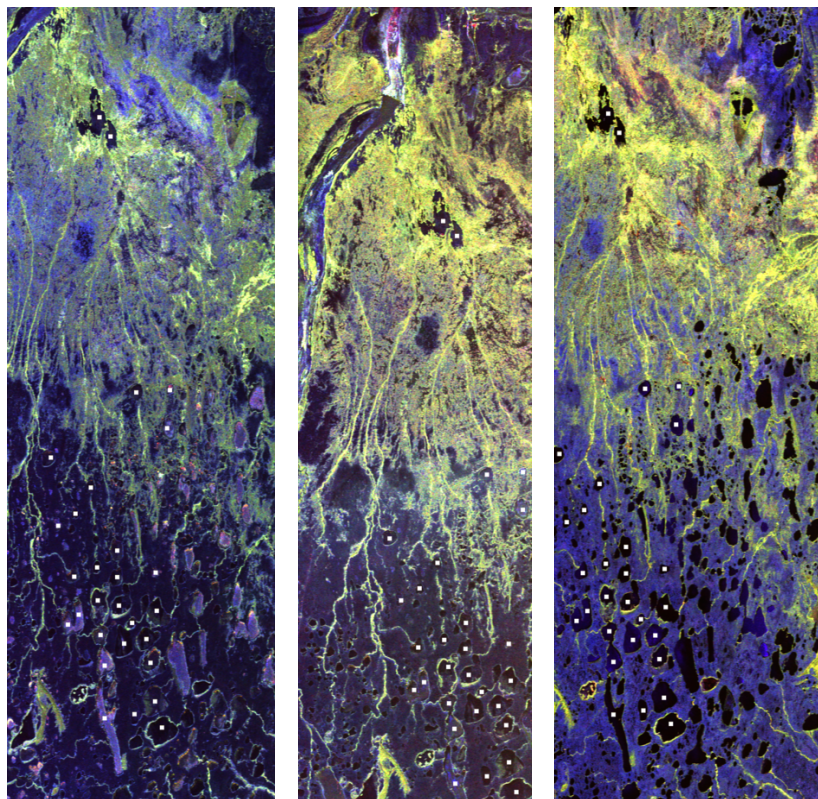


Figure 3.2 Churchill site: reference data.

between floating and grounded ice, which had been discussed in Section 1.2. For the purpose of estimating lake depth, Laura Brown and Claude Duguay proposed an ice thickness model in [9], where measurements of ice thickness on the Malcolm-Ramsay Lake were compared with model predictions. Those ice thickness measurements are shown in Fig. 3.2b. The lakes of interest in this study are located around $(58.46^{\circ}\text{N}, -93.86^{\circ}\text{E})$, which is rather to the west of the Malcolm-Ramsay lake, but since ALOS did not cover Malcolm-Ramsay area, the closest area observed by ALOS is considered and the same ice thickness is assumed.

The Pauli images shown in Fig. 3.3 are filtered from the additive noise, by considering a 7×7 window for calculating the coherency matrix. The near range for all ALOS acquisitions shown here is on the left side of the image (west) while the far range is on the right side (east). The ALOS data set available over Churchill includes three acquisitions, one during summer and two during winter. In order to better compare the changes within the lake ice, the Pauli colour coded winter images are normalised to the same RGB colour mapping. The lakes selected in the winter images are the ones that are observed in both acquisitions and the lake samples are indicated by a white box in the Pauli image. Near and far range differences are neglected, since the variation in the look angle is only around 2° .

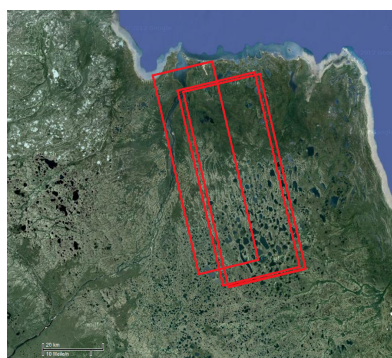
Measurements indicate a 1.5 m ice thickness during the first acquisition, and a slight increase of the ice thickness to 1.6 m for the second acquisition. Pauli images do not show a dramatic change in the two winter acquisitions over the



(a) SAR image from April 23, 2009 (Pauli image)

(b) SAR image from May 10, 2009 (Pauli image)

(c) SAR image from July 27, 2010 (Pauli image)



(d) ALOS-PALSAR Scene location in Google Maps [39]

Figure 3.3 ALOS data over Churchill site.

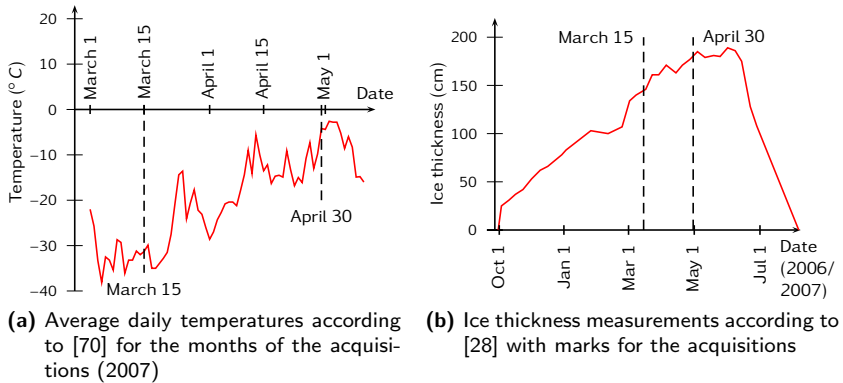


Figure 3.4 Baker Lake site: reference data.

lakes while a very clear difference can be observed and compared to the summer acquisition. The polarimetric parameters are discussed in Section 3.3.

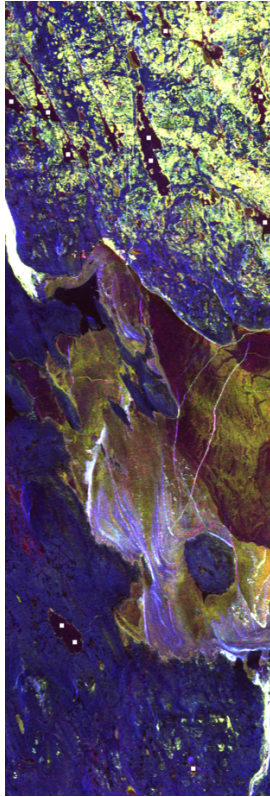
3.1.2 Baker Lake Site

Information about the ice thickness of Baker Lake is provided by the Canadian Ice Service [28]. The ice thickness on the lake is around 1.50 m to 1.85 m during the time of the two ALOS winter acquisitions as shown in Fig. 3.4b, with an increase of around 30 cm during the second acquisition compared to the first one.

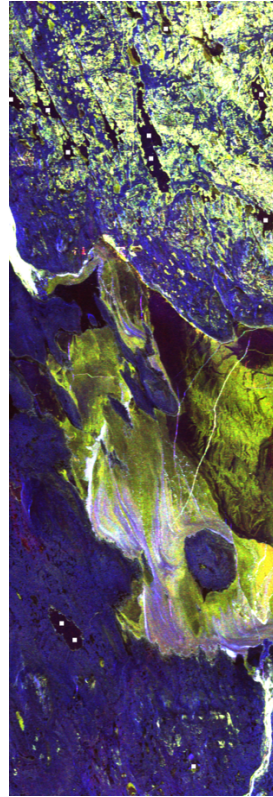
Baker Lake itself is not considered, because of its large size which makes it susceptible to cracking due to the presence of fast flowing water, such that its backscattering is highly influenced by cracks. Samples from the smaller lakes that are around Baker Lake are evaluated and assumed to have similar ice thickness as Baker Lake. Those samples are visible in the Pauli image as they correspond to the bright squares in the middle of the lake. ALOS acquisitions are located around (64.35° N, -95.99° E), and both of the acquisitions are acquired during winter. Pauli images of the site in Fig. 7.18a are normalised to the same RBG colour mapping, for the purpose of better comparison.

3.1.3 Inuvik Site

The Canadian Ice Service [28] also covers a lake in the Inuvik region (68.12° N, -131.85° E). Unfortunately the ice thickness data are available only for several years before the ALOS observations. Nevertheless, the old data show



(a) SAR image from March 15, 2007 (Pauli image)

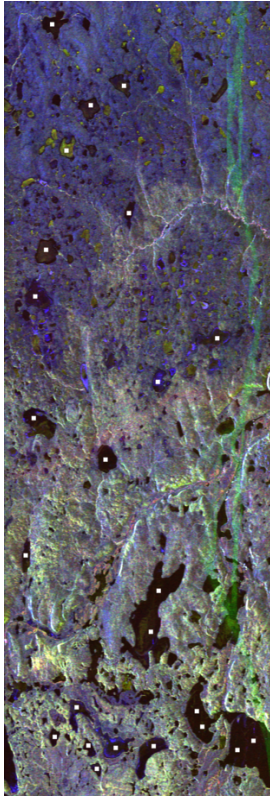


(b) SAR image from April 30, 2007 (Pauli image)

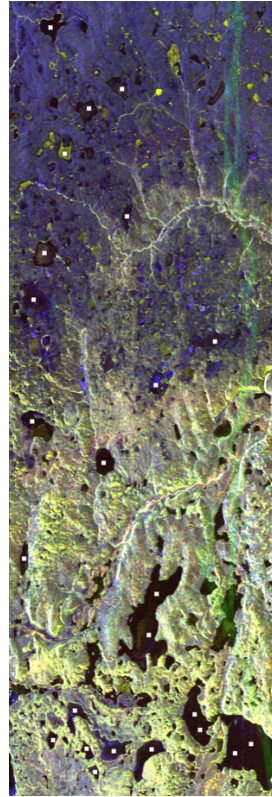


(c) Image of the scene taken from Google Maps [39]

Figure 3.5 ALOS data over Baker Lake site.



(a) SAR image from March 11, 2007 (Pauli image)



(b) SAR image from April 26, 2007 (Pauli image)



(c) Image of the scene taken from Google Maps [39]

Figure 3.6 ALOS data over Inuvik site.

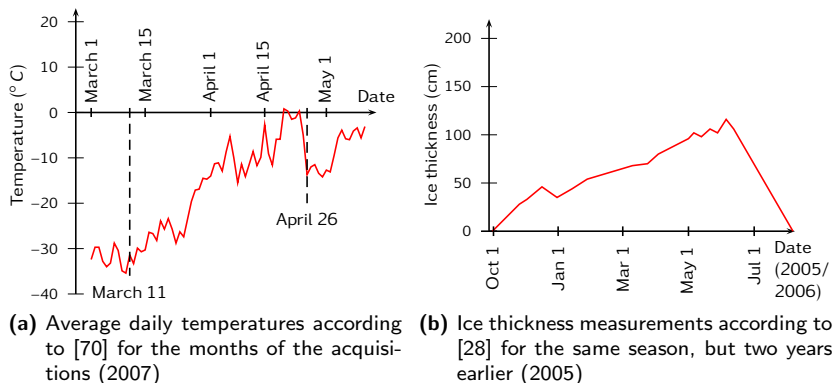


Figure 3.7 Inuvik site: reference data.

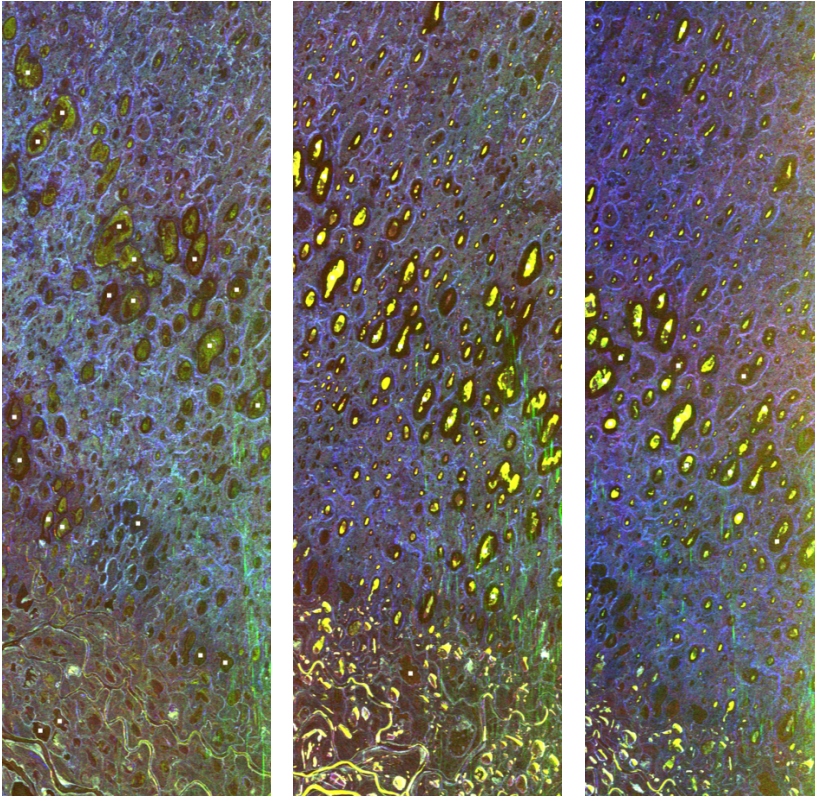
some short periods in May during which the ice thickness is reduced indicating ice melting. Temperature measurements are available freely in “National Climate Data and Information Archive” provided by Environment Canada [70]. Fig. 3.7a shows the temperature measurements during the ALOS acquisitions. The plot shows average temperatures above 0°C during the week before the second acquisition. Therefore a short period of ice melting, similar to the ones observed the years before through the ice thickness measurements, is expected before the second acquisition.

Two ALOS winter images are available in this area and are used to evaluate the lakes using the same procedure applied for the previous sites for evaluating the images. The SAR images show a range ambiguity along the azimuth in far range especially visible in the cross-polarisation channel. The origin seems to be a river located at Nadir. Lakes located in this range ambiguity are avoided, as their polarimetric signature might be corrupted. Applying advanced techniques in future SAR systems can help in avoiding such unwanted echos [104].

3.1.4 Lena Delta Site

As mentioned in the beginning of this chapter, high methane emission occurs in the Lena delta region [86]. However the nature of the methane bubbles in the lake ice, in regards to size, density, and local variations are not available. Therefore investigations in this site are based on assumptions.

Because of the large dynamic range in the relative power between the different polarisations for different acquisitions from Lena delta, each Pauli colour coded image of Lena delta acquisitions is displayed with its own colour range.



(a) SAR image from November 27, 2008 (Pauli image)

(b) SAR image from March 28, 2009 (Pauli image)

(c) SAR image from May 01, 2009 (Pauli image)



(d) Image of the scene taken from Google Maps [39]

Figure 3.8 ALOS data over Lena Delta site.

The images are located around (73.3°N, 124.3°E). All the lakes within each image have been considered because only a small portion of the lakes overlaps between the images, which would limit the evaluation of the temporal changes.

The images show colour changes along the azimuth and the range which might be due to radio interference. However there isn't any source that describes an interference system in the region. The colour change might also be due to the changes in the physical properties of the soil as the observed scene distance from the Laptev see is changing along the azimuth.

3.2 Data Processing

As discussed in Chapter 2, for a monostatic system the noise free cross-polarisation channels for reciprocal scatterers are expected to be identical. Accordingly, the difference between the (HV and VH) channels for ALOS data have been used to estimate additive noise [57].

The principles of estimating the power of the additive noise and filtering it are proposed in [41]. The algorithm is based on diagonalising the 4×4 coherency matrix T_4 by solving its eigen problem. Usually four eigenvalues ($\lambda_1, \lambda_2, \lambda_3, \lambda_4$) are obtained with four eigenvectors arranged in the eigenvector matrix $[U_4]$. The fourth eigenvalue is $(|S_{hv} - S_{vh}|^2)/2$, and corresponds to the additive noise power. To filter the noise, the fourth eigenvalue is subtracted from each of the eigenvalues. The sum of the new eigenvalues is assumed to be the signal power. The filtered coherency matrix is obtained then as

$$\begin{bmatrix} & & & 0 \\ & [T_3] & & 0 \\ & & & 0 \\ 0 & 0 & 0 & 0 \end{bmatrix} = [U_4] \begin{bmatrix} \lambda_1 - \lambda_4 & 0 & 0 & 0 \\ 0 & \lambda_2 - \lambda_4 & 0 & 0 \\ 0 & 0 & \lambda_3 - \lambda_4 & 0 \\ 0 & 0 & 0 & \lambda_4 - \lambda_4 \end{bmatrix} [U_4]^{-1}. \quad (3.1)$$

For the ALOS data used in this study, the coherency matrix is obtained by averaging a 7×7 spatial window, which provides an adequate number of independent looks. The data are filtered according to Eq. (3.1) and the signal to noise ratio is evaluated.

At L-band the distortion induced by the ionosphere can affect the data. Faraday rotation is one of the most prominent ionospheric effects, which alter the polarimetric signature. Faraday rotation occurs because of the presence of both the ionosphere and the Earth magnetic field. A higher influence of Faraday rotation closer to the Earth's poles is expected [7]. Faraday rotation of a few degrees (less than 45°) transports part of the horizontal backscattering into the vertical channel and part of the vertical backscattering into the horizontal channel. This process increases the backscattering from the

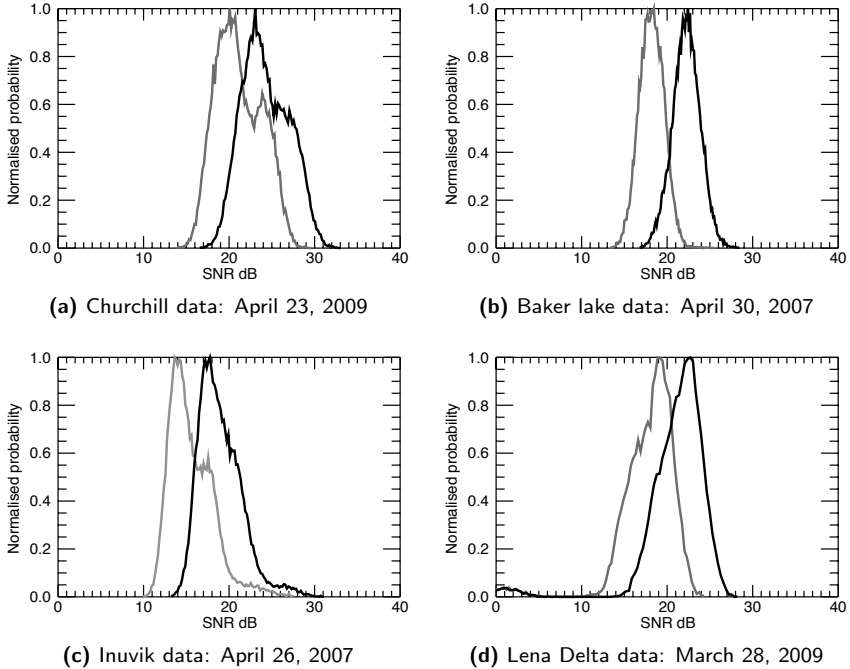


Figure 3.9 Histograms of SNR over the lakes samples before Faraday rotation correction (grey) and after Faraday rotation correction (black)

cross-polarisation channels. As the cross-polarisation channels include a power portion transported from the co-polarisation channels, the coherency between the cross-polarisation and co-polarisation channels increases. However this coherency is expected to be zero for reflection symmetry (Section 2.4) in Faraday rotation free data. In addition, Faraday rotation produces a larger $\langle |S_{hv} - S_{vh}|^2 \rangle / 2$, as it breaks the reciprocity of the scatterer.

For the correction of Faraday rotation, the algorithm in [7] has been used. The algorithm converts the data to circular polarisation basis and estimates the Faraday rotation angle from the angular difference between the two circular cross-polarisations. The exact same processing engine implemented in [50] has been used to calibrate the data and only calibrated data are considered for further processing.

The coherency matrix of the Faraday rotation free data are calculated and filtered from the additive noise. An increase of around 3 dB in the signal to

noise ratio (SNR) over the lakes is observed as shown in the histogram plots in Fig. 3.9. Despite that the entropy-alpha histograms did not change noticeably before and after Faraday rotation correction, only corrected data are considered.

3.3 Data Analysis

The polarimetric parameters and ratios of the lakes' samples are presented and discussed in this last section of this chapter. For each site, the correlation between the two co-polarisation channels as well as between the cross- and co-polarisation channels are shown. The histograms of the co-polarisation ratio and phase difference are plotted. The eigen decomposition presented in Section 2.4 is implemented on the data, and the obtained entropy, mean alpha angle and anisotropy are estimated and discussed.

3.3.1 Churchill Site

Because of the three available acquisitions, one in summer and two in winter, the site is a good candidate to compare the backscattering from the lakes for the case of ice presence with the case of ice absence.

In Fig. 3.10 and 3.11, the polarimetric parameters of the lake samples over Churchill region are displayed. The yellow curve corresponds to the summer acquisition (27/07/2010), the green one to the first winter acquisition (23/04/2009), and the blue line to the second winter acquisition (10/05/2009).

From the SNR histogram in Fig.3.10a, two peaks, one of high and one of low power, are observed in the summer acquisition. The peak with the low power corresponds to open water as it is expected to have less backscattering than ice. The second peak could be related to parts of the lakes where ice is still available at the time of the acquisition. The first winter acquisition shows, on average, higher backscattered power than the second. Nevertheless, both winter acquisitions show higher power than open water during summer.

The coherency between the co-polarisation and cross-polarisation channels is in general low as the data are corrected for Faraday rotation. The peak is around 0.003 and the variance increases as a function of noise dominance, such that summer data show larger variance since it has less SNR. The coherency between S_{hh} and S_{vv} is presented only for Churchill site as the other sites show the same behavior.

The coherency between the co-polarisation channels in Fig. 3.10c shows higher values during summer than during winter, which is due to the dominance of the surface backscattering during summer compared to winter case.

The ratio of the horizontal to vertical polarisation is shown in Fig. 3.10d. Summer data show a higher vertical backscattering than horizontal, which

matches the predictions of Bragg surface backscattering. Winter data show a remarkable increase in the ratio of horizontal to vertical backscattering compared to the summer case. The co-polarisation phase difference is around -4° during summer, which is very similar to a Bragg surface, whose predictions do not exceed 2° . Winter data show a zero co-polarisation phase difference.

From the scattering mechanisms considered by the model-based decomposition presented in Section 2.5, a higher horizontal than vertical backscattering is obtained from the backscattering of a dihedral consisting of two surfaces. The winter data cannot be interpreted by this scattering mechanism since a zero co-polarisation phase difference is measured instead of 180° despite the higher horizontal than vertical backscattering

A possible scattering mechanism that can predict a zero co-polarisation phase difference with a higher horizontal backscattering than vertical is a volume of particles where the major axis of the particles are horizontally oriented, as horizontally oriented dipoles scatter back higher horizontally polarised portion than vertically polarised portion of the electromagnetic wave. Since the descriptions of inhomogeneities within ice refer to rather vertically oriented structures as discussed in Section 1.1, a mechanism of a volume backscattering that produces a higher horizontal than vertical backscattering is not very likely.

Therefore the dihedral scattering from a volume of ellipsoids and the subsurface is more realistic and will be developed and investigated in Chapter 6.

The entropy-alpha values of the summer data presented in Fig. 3.11a cover the same region of entropy-alpha as X-Bragg at around 25° local incident angle, as will be clarified in Section 4.4. In Fig. 3.11 b, and c the winter data show higher entropy and alpha values. Nevertheless the entropy-alpha range is still far from the region expected by a dihedral scattering of two surfaces shown in Fig. 2.3.

The anisotropy values of the data are shown in Fig. 3.11d. For the summer data, the values are close to unity with a peak around 0.8 which is expected for a Bragg surface and, more precisely, for a rather smooth X-Bragg surface. Winter data show lower anisotropy values.

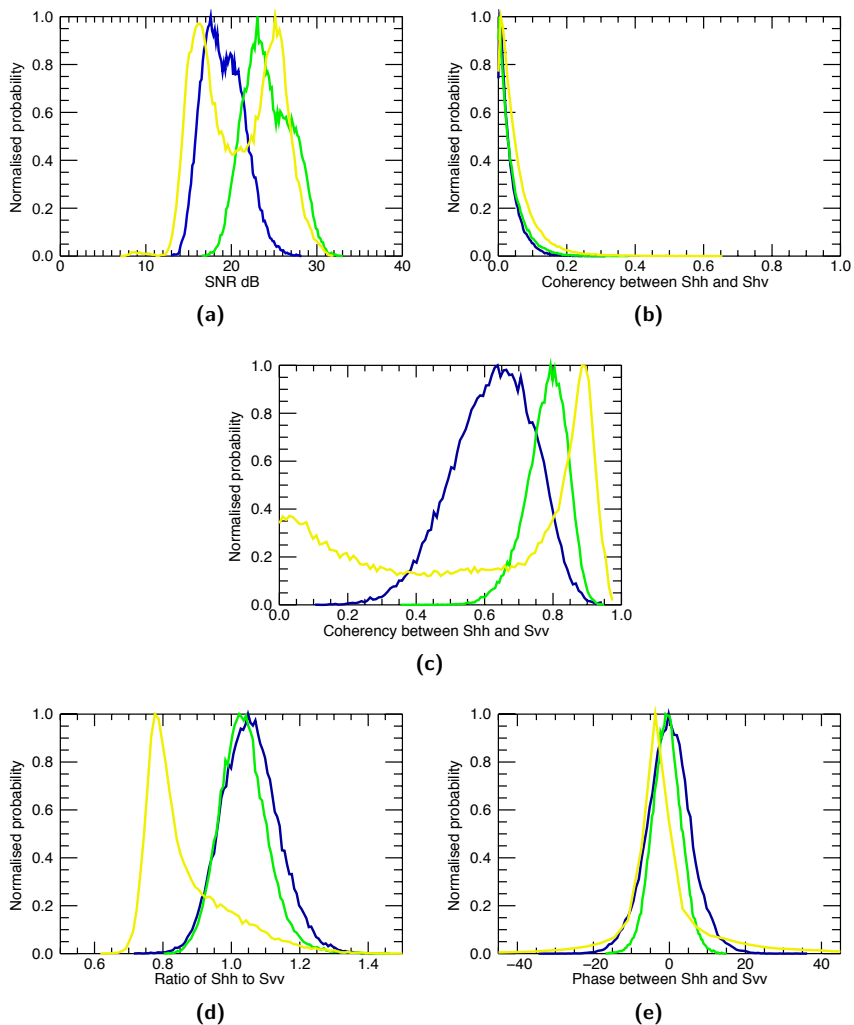


Figure 3.10 Polarimetric parameters of the lake samples over Churchill region; Yellow: summer acquisition on 27/07/2010, green: first winter acquisition on 23/04/2009, blue: second winter acquisition on 10/05/2009

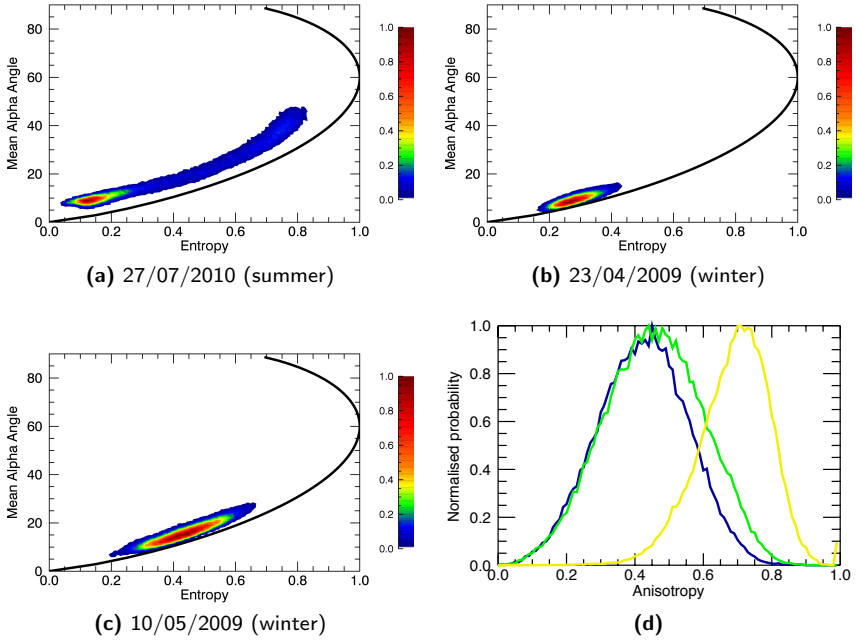


Figure 3.11 Entropy-alpha histogram and anisotropy plots for the Churchill data.

3.3.2 Baker Lake Site

The two winter acquisitions show almost similar backscattered power, both shown in Fig. 3.12. The coherency between the co-polarisation channels is around 0.8. The horizontal backscattering is equal or slightly larger than the vertical backscattering with a zero phase between them. The entropy-alpha histogram in Fig. 3.13 shows that for some samples the entropy and alpha values have increased during the second acquisition on 30/04/2007 compared to the first acquisition on 15/03/2007.

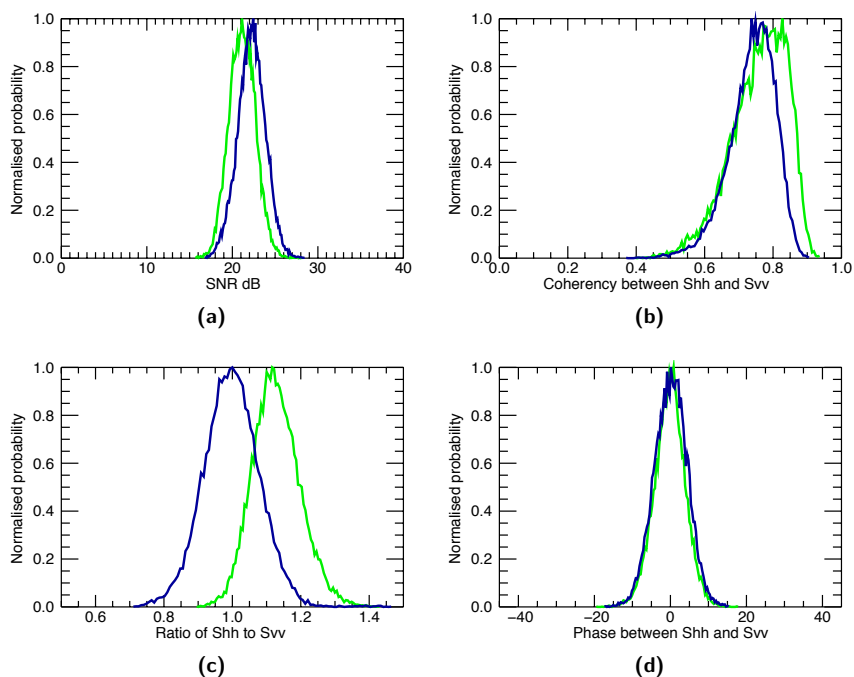


Figure 3.12 Polarimetric parameters of the lake samples close to Baker Lake region; Blue curve: acquisition on 15/03/2007, green curve: acquisition on 30/04/2007

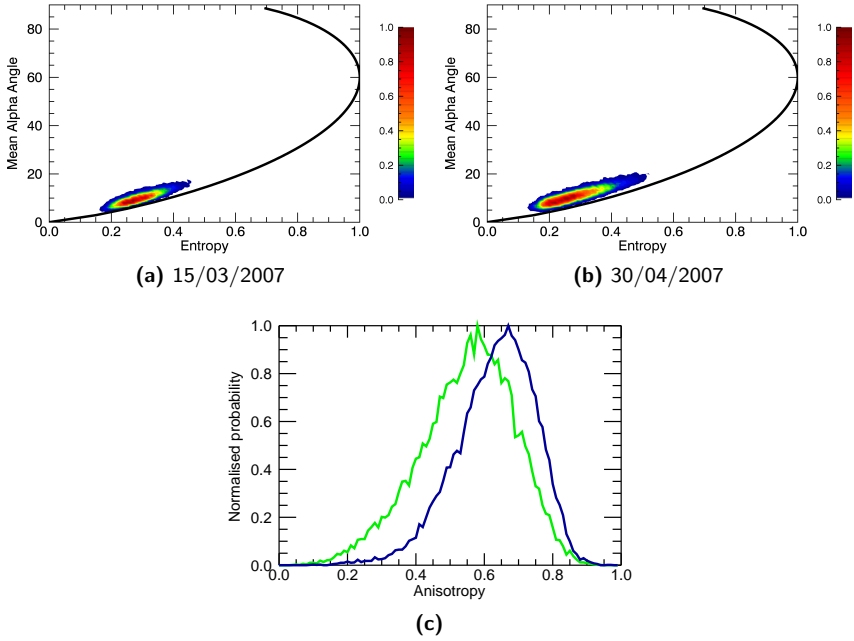


Figure 3.13 Entropy-alpha histogram and anisotropy plots for the Baker Lake data.

3.3.3 Inuvik Site

The two winter acquisitions from the Inuvik site, show almost similar backscattered power. The coherency between the co-polarisation channels is around 0.5 for the first acquisition on 11/03/2007 and 0.6 for the second one on 26/04/2007. Both observations show a second smaller peak with a coherency close to one in Fig. 3.14b. This small power and high coherence peak might be an artefact caused by the choice of lake samples that include some land surface. This is also visible in the entropy-alpha histogram in Fig. 3.15 a and b, as a second peak appears in the histogram which lays in the typical region for X-Bragg surface scattering. The horizontal backscattering is in general larger than the vertical backscattering with a zero phase between them.

The entropy-alpha histogram shows higher values during the first acquisition in March compared to the second acquisition in April.

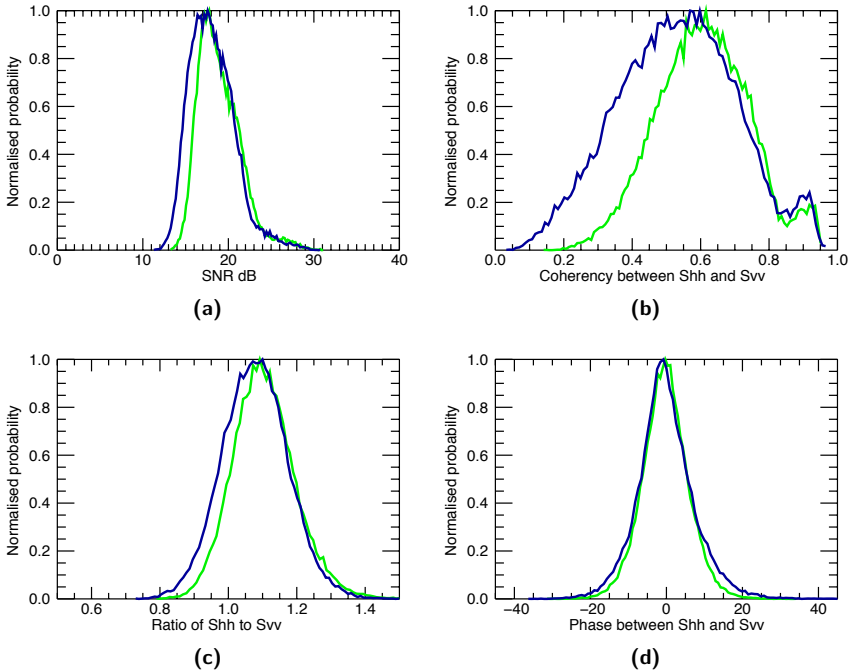


Figure 3.14 Polarimetric parameters of the lake samples in Inuvik region; Blue curve: acquisition on 11/03/2007, green curve: acquisition on 26/04/2007

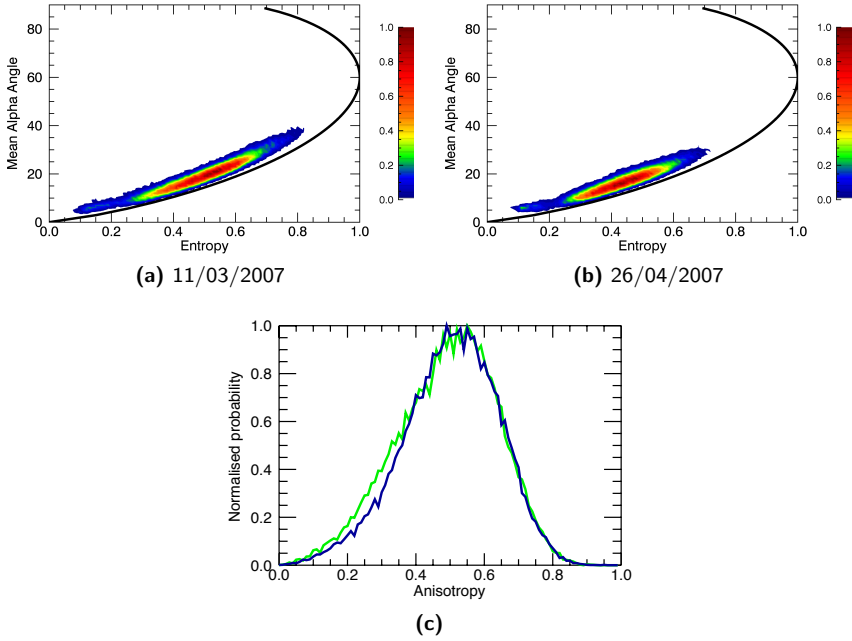


Figure 3.15 Entropy-alpha histogram and anisotropy plots for the Inuvik data.

3.3.4 Lena Delta Site

Early winter data show similar polarimetric properties as the winter data from the other sites. Winter data acquired during March and May show a lower co-polarisation coherency and a higher vertical backscattering than horizontal one.

Figures 3.16 and 3.17 show polarimetric parameters of the lake samples in Lena Delta site. The entropy-alpha histogram for the March and May acquisitions show much higher entropy and alpha values compared to the other sites, as the entropy is almost close to one.

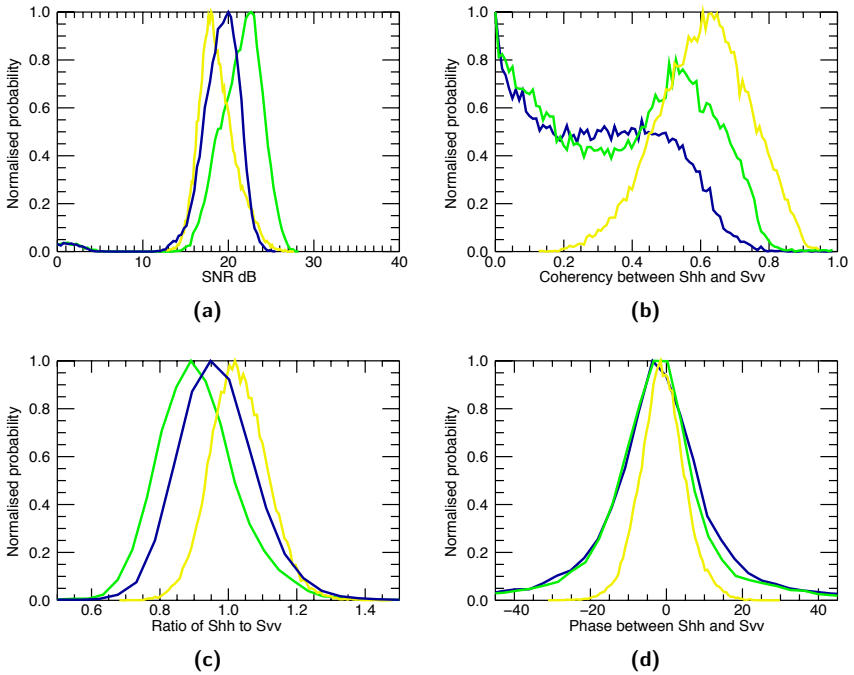


Figure 3.16 Polarimetric parameters of the lake samples in the region of Lena Delta; Yellow: early winter acquisition on 27/11/2008, green: first (late) winter acquisition on 28/03/2009, blue line: the second (late) winter acquisition on 01/05/2009

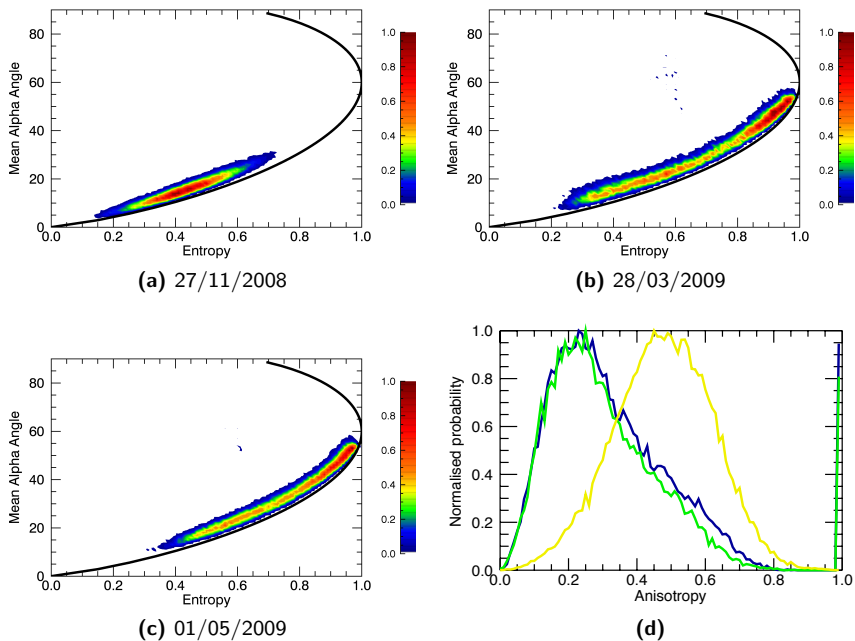


Figure 3.17 Entropy-alpha histogram and anisotropy plots for the Lena Delta data.

Chapter 4

Random Rough Surface Scattering

The purpose of this chapter is to introduce scattering, transmission and reflection of a polarised electromagnetic wave impinging a surface, which are dependent on the wavelength of the incident electromagnetic wave, geometry, and the surface properties.

In the first part of this chapter, the physical and geometrical surface properties are summarised. In the second part, several surface scattering models are discussed. The last part of this chapter provides a close look to Bragg surface model and X-Bragg model as X-Bragg model has been implemented in this study to model both ice-water and ice-soil interfaces of the subarctic lakes.

4.1 Surface Properties

Surface properties, both of the physical and geometrical nature of the soil, influence the scattering, reflection, and transmission of the electromagnetic wave when it impacting the surface. Physical properties are mainly described by the complex dielectric constant of the surface. This constant influences the penetration through the surface layer, the direction of the coherent component of the wave (the reflected and the transmitted), the polarimetric ratios, the propagation speed of the electromagnetic wave within the medium, and the scattered power from the surface [90]. The geometrical parameters describe the spatial distribution of the surface material over the interface. Surface roughness and its variation in space give a statistical evaluation of spatial changes of the surface. The geometrical parameters are mainly responsible for transferring part of the power from the coherent components to the scattered ones. They also influence the polarimetric ratios.

4.1.1 Physical Properties

The complex dielectric constant, which is also called relative permittivity $\epsilon_r = \epsilon'_r + j\epsilon''_r$, is the main physical parameter that influences the electromagnetic waves encountering a surface. Theoretically, the permeability μ_r can have an effect equivalent to the permittivity. In practice, most of the materials have a permeability that is close to unity, which is especially true for normal soil that does not contain heavy materials, while volcanic sediment can have a non-negligible permeability [103]. The permeability is considered to be equal to unity throughout this study.

The permittivity of the material depends on its type, soil porosity, temperature, operating wavelength, and other physical and chemical parameters. The Debye relaxation equation [44] describes the dependency of the permittivity of a dielectric material with an electrical dipole moment, such as water, on different frequencies and temperatures. In general, the equation shows that the permittivity increases with increasing temperature and that it is lower for higher frequencies.

Regarding the porosity, when the vacancies between the soil grains are filled with air, then the permittivity is lower compared to the permittivity of the soil grains. When those vacancies are filled with water then the soil permittivity increases with increasing water content, since the water permittivity is high. There are several approaches to obtain the permittivity of a mixture, for example the method proposed by G.P. De Loor in [18].

In general, the real part of the water permittivity is around 80 at low frequencies up to 3 GHz [42], while for ice it is much lower ($\epsilon'_r = 2.5 \dots 3$) because of the ice crystallisation which binds the water dipoles to each other and prevent them from getting aligned along the varying electric field. For the same reason, frozen soil has a lower permittivity than wet soil. However it requires lower temperatures to freeze wet soil than to freeze water [52].

The imaginary part of the permittivity is directly related to losses, such that the penetration depth depends mainly on it [42]. The imaginary part of the permittivity, at a certain frequency, leads to losses in the material in the same way as the conductivity.

For water, the conductivity varies strongly depending on the salt content [5]. For natural water, a high conductivity is assumed and even higher for sea water than for fresh water. When water freezes to form ice, the water molecules form crystals which reject the salt [95] such that the ice has low conductivity. As a consequence, an electromagnetic wave at low frequencies can penetrate through it.

For the subarctic lakes, the water permittivity is assumed to be $\epsilon_r = 80 + j20$, while for the ice a lower permittivity of $\epsilon_r = 2.5 + j0.01$ is assumed. In spite

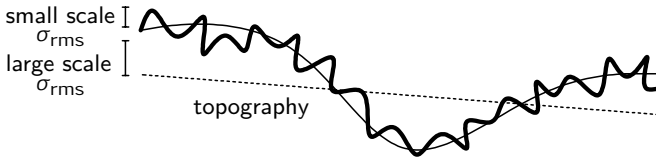


Figure 4.1 A two-scale rough surface

of the pessimistically high value for the imaginary part of the ice permittivity as compared to literature, the losses for the penetration of a 2 m ice layer are almost negligible. For frozen soil a permittivity of $\epsilon_r = 8 + j2$ is assumed. These assumptions can vary with temperature and for different material compositions. Nevertheless, the assumptions are a good starting point for the modelling of subarctic lakes since they demonstrate the high dielectric contrast between water, frozen soil and ice.

4.1.2 Geometrical Properties

The spatial variations of the surface are described statistically by three parameters: The standard deviation of surface height σ_{rms} , the surface correlation length l , and the normalised autocorrelation function ρ .

Surface roughness

The standard deviation of the surface height σ_{rms} is the measure of the surface roughness. It is obtained by the root mean square of the height differences between the samples of the natural surface compared to the average height of the surface. The average height of the surface can change when the area considered increases as shown in Fig. 4.1. For this reason, the roughness is usually defined for a certain spatial frequency, and usually referred to as small scale and large scale roughness [90].

The dependency of the scattered electromagnetic wave on the roughness varies for different wavelengths, such that surfaces appear smoother at lower frequencies. Therefore the surface roughness is usually multiplied by the wave number $k\sigma_{rms}$. The considered roughness in modelling should be measured with the scale that plays the most significant role in the scattering of the electromagnetic wave, and this scale depends on the system resolution and operating frequency. For high resolution systems, large scale roughness should be treated as topographic slopes that is considered in the local incident angle of the surface scattering model [81], [82].

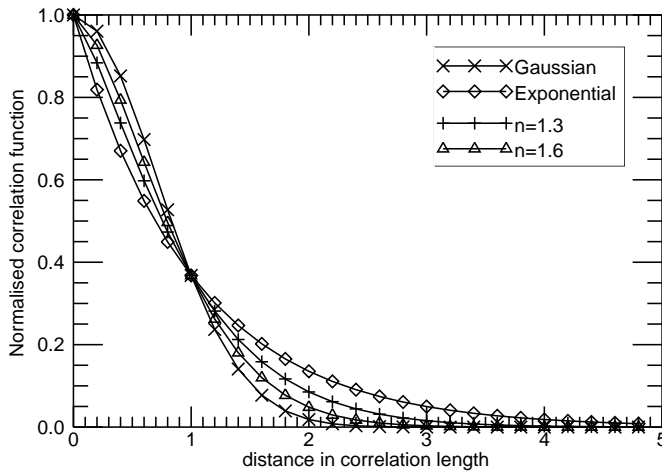


Figure 4.2 An example of different surface correlation functions that had been considered in [62]

Surface correlation length

The correlation length describes the spatial properties of the surface. When considering an area larger than the correlation length, the surface roughness shows large changes in its geometrical parameters. The correlation length can be calculated from the surface autocorrelation function, as it corresponds to the distance in which the correlation drops to e^{-1} .

Because of the same reasons discussed in the previous section, the correlation length is usually expressed by its product with the wave number kl . In general roughness describes the vertical variation, while the correlation length shows the horizontal variations of the surface.

Surface autocorrelation function

The shape of the autocorrelation function can influence the power scattered by the surface. Observations of surfaces described a surface autocorrelation function whose trend varies between Gaussian and Exponential distribution. Figure 4.2 shows different shapes of the correlation function that had been considered to represent the surface autocorrelation. The plots show the correlation versus the distance which has been normalised to the correlation length.

The influence of the autocorrelation function shape on the backscattered power and polarimetric signature is significant when the system wavelength is in the same range as the correlation length [63], because the observed roughness range of the surface (the effective roughness) varies for different frequencies

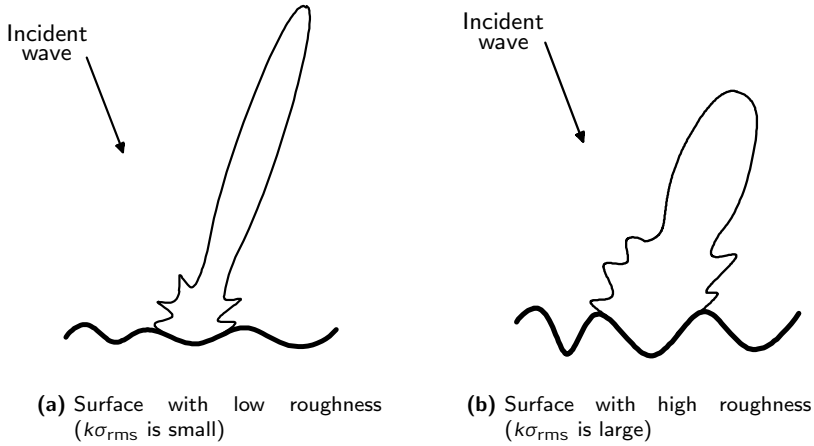


Figure 4.3 Example of schematic scattering pattern for two surfaces with different roughness.

within the system bandwidth. This variation follows the shape of the correlation function, which shows a varying slope when the electromagnetic wavelength is in the range of the correlation length [62].

4.2 Surface Modelling

When a plane electromagnetic wave impinges a surface, each point on the surface acts similar to a point source. The radiations from all the points are added together. In the direction of the specular reflection, the individual contributions are added coherently, such that they generate a high, directed power component, referred to as the coherent component [90]. Depending on the geometrical properties of the surface and especially the roughness, the losses in the coherent component can vary.

In directions other than the specular reflection direction, the radiation is added incoherently and only a scattered component is observed. The surface roughness influences the total power in the coherent component, such that higher roughness reduces the power in the coherent components and increases the incoherent scattered component, as shown in Fig.4.3.

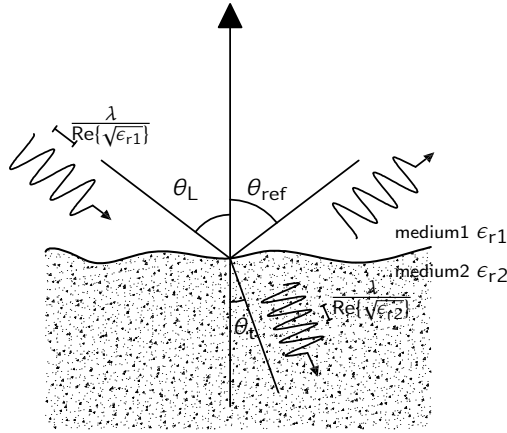


Figure 4.4 Reflection and transmission on a surface.

4.2.1 Coherent Component (Specular Reflection and Transmission)

Part of the power from the wave incident on the surface is reflected while the other part is transmitted. Both reflected and transmitted powers are obtained by the coherent addition of the fields on the boundary between the two media (the medium that contains the local incident and reflected wave and the medium that contains the transmitted wave). The intensity of the reflected or transmitted power portion depends on the local incident angle and the complex permittivities of the media.

The direction of the specular reflection lies in the incident plane which is defined by the direction of the incident wave and the surface normal vector. The local incident angle θ_L , which is the angle between the incident wave and the normal vector is equal to the reflected angle θ_{ref} that is the angle between the normal vector and the direction of the reflected wave, as shown in Fig. 4.4.

The specular reflection is defined by the Fresnel coefficients presented in Eq. (2.27), which are derived from the boundary conditions [90].

The transmitted wave travels in the second medium with a different speed as its wavelength changes to $\lambda_{Re\{\sqrt{\epsilon_{r2}}\}}$ [19]. For this reason, the direction of the transmitted coherent component changes according to the permittivity of the medium. In general, the transmitted wave lays also on the incident plane and the transmitted angle θ_t is calculated according to

$$\text{Re}\{\sqrt{\epsilon_{r2}}\} \sin \theta_t = \text{Re}\{\sqrt{\epsilon_{r1}}\} \sin \theta_L. \quad (4.1)$$

The transmissions coefficients are obtained by considering the power portion of the incident wave that is not reflected. The power transmission coefficients for both horizontal and vertical polarization are given by,

$$\begin{aligned} T_{\perp}^2 = 1 - R_{\perp}^2 &= \frac{4\sqrt{\epsilon_{r1}} \cos \theta_L \sqrt{\epsilon_{r2} - \epsilon_{r1} \sin^2 \theta_L}}{\left(\sqrt{\epsilon_{r1}} \cos \theta_L + \sqrt{\epsilon_{r2} - \epsilon_{r1} \sin^2 \theta_L}\right)^2} \\ T_{\parallel}^2 = 1 - R_{\parallel}^2 &= \frac{4\epsilon_{r2} \cos \theta_L \sqrt{\epsilon_{r1} \epsilon_{r2} - \epsilon_{r1}^2 \sin^2 \theta_L}}{\left(\epsilon_{r2} \cos \theta_L + \sqrt{\epsilon_{r1} \epsilon_{r2} - \epsilon_{r1}^2 \sin^2 \theta_L}\right)^2}. \end{aligned} \quad (4.2)$$

The surface roughness effect on the power of the coherent component is modelled as exponential losses as follows [90]

$$\text{Coherent component} \propto e^{-4k^2 \cos^2 \theta_L \sigma_{rms}^2}. \quad (4.3)$$

From the equation above, it can be seen that a roughness of several centimetres in *L*-band ($\lambda_0 = 24 \text{ cm}$ and $\lambda_{ice} \approx 10 \text{ cm}$), is already very small and will drive the exponential term to be almost equal to one. Therefore in the following, these losses in the coherent component of the scattering are neglected. The depolarisation in the coherent component due to roughness had not been considered here.

4.2.2 Incoherently Scattered Component

For a monostatic side-looking SAR system, the specular reflection does not contribute to the backscattering, so in spite of the low power contribution of the incoherent scattering component compared to the contribution of the coherent component, only the incoherent scattering component is received by the system. Several models have been proposed to describe this component. Some of those models are empirical and based on experimental measurements, others are theoretical, and some combine theory and empirical approaches (semi-empirical). In this study, only theoretical models are addressed because empirical models, for the subsurface case, are not well developed.

For the electromagnetic problem on the surface boundary of any surface geometry, the Kirchhoff approximation is used. Nevertheless the theoretical solution is too complex to be formulated in a closed or in a series form. Therefore theoretical models consider only a certain range of surface geometries [90].

For surfaces with large correlation lengths (compared to the wavelength) optical approaches have been implemented. The Geometrical Optics model

predicts a polarimetric backscattering that is equal in both horizontal and vertical channels [90], which does not fully match the data over frozen lakes. Models based on Physical Optics predict a different horizontal than vertical backscattering, but so far they have not succeeded in practically estimating the polarimetric backscattering from bare soil surfaces.

Surfaces with low correlation length compared to the wavelength and with low roughness can be modelled using the Small Perturbation Method (also referred as Bragg model) [90]. Bragg surface model has proved to provide a good estimation for the surface backscattering within its validity range. The model has been used in this thesis, not only because of its performance, but also because of its simplicity such that its polarimetric signature is independent of the correlation length. The influence of roughness on the polarimetric signature is observed in experimental data but not considered by Bragg model; therefore the model has been extended by X-Bragg model [41]. X-Bragg model has a better estimation for the surface backscattering [41], such that it could model a wider range of surface roughness compared to the simple Bragg surface.

The Integral Equation Method (IEM) covers a large range of surface correlation lengths and roughnesses [63]. The method gives identical estimations of the polarimetric backscattering as Bragg model when a small value for the correlation length is assumed [34], [2]. The main challenge in implementing the IEM method in its validity range is the strong dependency of its polarimetric signature on the correlation length and the shape of the surface correlation function [62]. The Small Slope Approximation model (SSA) is another approach to estimate the backscattering of surfaces that are rougher than Bragg surfaces. The model requires a similar knowledge about the surface as the IEM model, which also limits its applicability [29].

Information about the surface roughness and correlation length, for the interface between ice and water/soil, are not available. Nevertheless the Small Perturbation (SPM) or Bragg surface model is used, not only because it is widely independent of the correlation length, but also because at L -band, Bragg and X-Bragg models show practically a good performance in the prediction of the backscattering from bare surfaces [41].

4.3 Small Perturbation Model (Bragg Surface Scattering)

The theoretical conditions for applying the SPM model are a standard deviation of the surface height of less than 5% of the wavelength and a low correlation length such that $kl < (k\sigma_{\text{rms}})^2$ [90].

The standard deviation considered corresponds to the surface roughness component with a spatial frequency of $2k\sin\theta$. The model assumes that this sur-

face component resonates with the incident wave and is responsible for the main part of the backscattered power, such that a Fourier transform of the surface correlation function $W(k)$ is obtained and only this spatial frequency is used to calculate the backscattering. The radar cross section of Bragg surface σ_{pp} is given as follows [90]

$$\sigma_{vv, hh} = 8k^2 \sigma_{rms}^2 \cos^4 \theta |R_{v,h}|^2 W(2k \sin \theta, 0). \quad (4.4)$$

From this equation, it is clear that the power backscattered by Bragg surface increases with higher roughness, higher operating frequency, and lower local incident angle as long as $W(2k \sin \theta)$ is not too small. The polarimetric signature depends on Bragg scattering coefficients R_h , R_v which are given in Eq. (2.24).

An investigation of a two-layered structure built up by Bragg surface and Bragg subsurface is performed in [1]. The results show a total polarimetric alpha angle value equivalent to the power weighted average of the alpha values belonging to the surface and subsurface. The entropy value of the two-layered structure hardly increases above zero. This indicates that the polarimetric signature of a two-layer structure is almost similar to the polarimetric signature of a synthetic single Bragg surface whose surface parameters are between the parameters of the two surfaces and closer to the parameters of the dominant one.

The power contribution from the surface is reduced in comparison to the contribution from the subsurface with increasing the incident angle when the propagation losses within the upper layer are small. Because of this, the parameters of the synthetic surface change with the angle and approach the parameters of the subsurface when increasing the incident angle. Consequently, the curve of alpha angle for the synthetic surface versus the local incident angle deviates from the one of a single Bragg surface.

Data acquired by ALOS covers a very small range of local incident angles. Therefore the backscattering from two Bragg interfaces will appear as a single Bragg surface. Thus, for the shallow subarctic lakes, a single Bragg layer is assumed. Since the contrast in the permittivity between air and ice is less than the contrast in the permittivity between the ice and the subsurface (water/wet soil), a higher power backscattered from the subsurface is expected. Therefore the synthetic Bragg surface is assumed to be similar in parameters to the subsurface only.

4.4 X-Bragg Model

The polarimetric parameters presented in Chapter 2 for Bragg surface depend only on the surface permittivity and the local incident angle. The first order (simple) Bragg model does not predict any cross-polarisation backscattering, which is in contrast to experimental data, that show a clear dependency of the polarimetric signature on the surface roughness [41]. In order to consider the influence of the surface roughness along the azimuth direction on the polarimetric signature, the extended Bragg model (X-Bragg) has been proposed. The roughness along azimuth is modelled by rotating the coherency matrix of Bragg surface around the line of sight and the final coherency matrix is then the integral over the different rotations. At a single small fragment of the surface, Bragg surface is asymmetric around the line of sight. The backscattering at that fragment transfers part of the co-polarisation backscattering to the cross-polarisation channel, as discussed in Section 2.4. For the full resolution cell, different fragments of the surface within the cell are rotated at different angles clockwise and anti-clockwise, where each rotation angle is specified by the surface slope at that fragment. The sum of the coherency matrices with different rotations results in a zero coherency between the co-polarisation and cross-polarisation channel and also a reduction in the coherency between the two co-polarisation channels.

For the mathematical calculation of the coherency matrix, a uniform distribution of the slope angles is assumed. The coherency matrix for X-Bragg surface [T_S] depends on the distribution width of the slope angles (2β) as follows

$$[T_S] = P_S \cdot \begin{bmatrix} 1 & \frac{R_h - R_v}{R_h + R_v} \text{sinc}(2\beta) & 0 \\ \frac{R_h - R_v}{R_h + R_v} \text{sinc}(2\beta) & \frac{(R_h - R_v)^2}{(R_h + R_v)^2} (1 + \text{sinc}(4\beta)) & 0 \\ 0 & 0 & \frac{(R_h - R_v)^2}{(R_h + R_v)^2} (1 - \text{sinc}(4\beta)) \end{bmatrix}. \quad (4.5)$$

The entropy-alpha distribution of X-Bragg surface is shown in Fig. 4.5. The entropy value increases when the roughness increases and reduces the difference between the horizontal and vertical polarisation, such that the value of alpha decreases.

The figure shows higher entropy and alpha values for higher local incident angles. Unfortunately, the polarimetric ALOS data set were acquired at 25° local incident angle, where the plot indicates a weak sensitivity of the surface entropy and alpha angle to permittivity changes. Therefore the investigations of grounded and floating ice in Chapter 7 are recommended to be reperfomed later with data sets acquired at higher local incident angles, in order to better observe the effect of the subsurface permittivity.

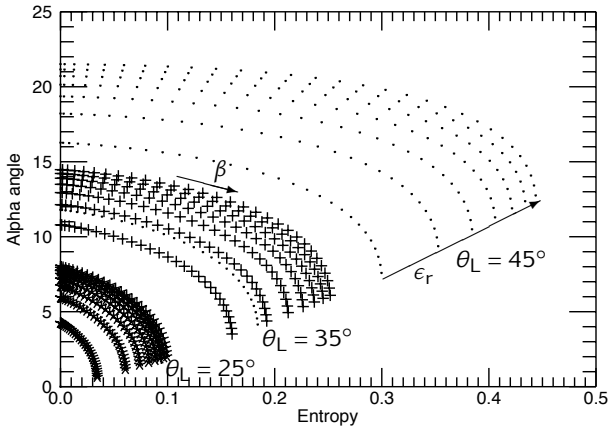


Figure 4.5 Entropy-alpha distribution for X-Bragg surface of different local incident angles plotted for changes in $\beta = 0 \dots \pi/2$ and $\epsilon_r = 3 \dots 25$.

Chapter 5

Particle and Volume Scattering

Volume scattering occurs within media with local variations in dielectric properties distributed in a three-dimensional geometry. When the electromagnetic wave penetrates into the media, it interacts with those local variations (particles). The excited particles scatter part of the wave energy and absorb another part of it. The interactions depend strongly on the particle size compared to the wavelength of the electromagnetic wave.

In this chapter, the interaction of the wave with a small particle whose radius $a < \lambda$ (Rayleigh or Mie scattering) for different shape, size and orientation is evaluated. The response of a cloud of particles is discussed in the last part of this chapter.

5.1 Scattering of a Single Particle

Particle scattering can be negligible when the particles are very small compared to the wavelength ($a < 0.0003\lambda$) [10]. For larger particles Rayleigh theory, Mie theory, and Geometrical Optics are used to model the scattering. Rayleigh scattering is an approximation of Mie scattering that considers the smaller sized particles. The particle size limit for the Rayleigh approximation to be valid varies across different references and applications ($a < 0.03\lambda$ in [10] and $a < 0.1\lambda$ in [90]).

The Mie scattering formulation is derived by solving Maxwell's equations on the boundary between the particle and background media [65]. The solution is very complex compared to Rayleigh. For particles of very large sizes, scattering can be considered to be a result of interference of the rays having multiple reflections and refractions according to the laws of Geometrical Optics [91].

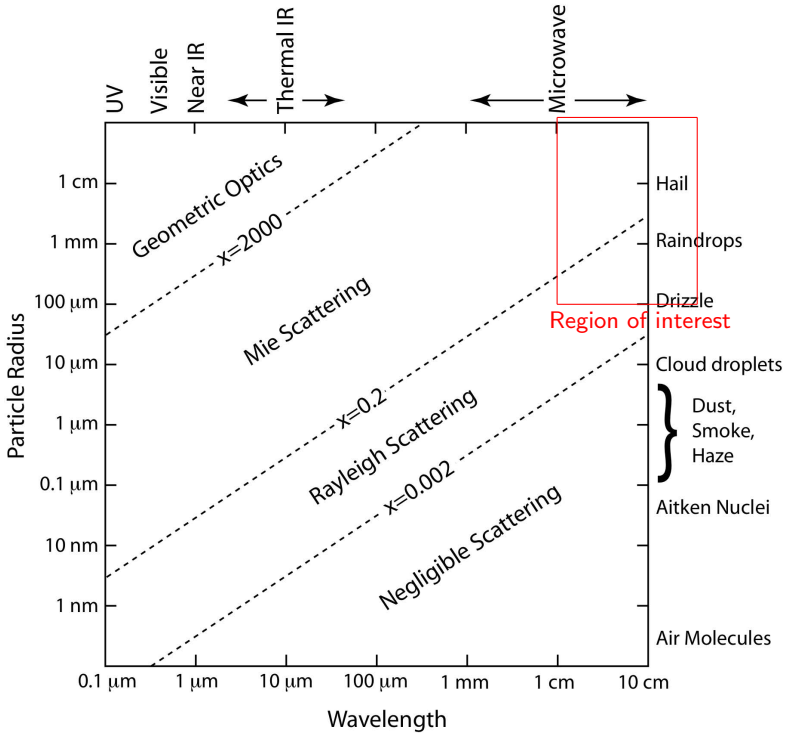


Figure 5.1 Application space for different scattering models over ranges of particle radius and wavelength, [10].

Fig. 5.1 shows the region covered by the three scattering models over different radiuses and wavelengths [10]. The factor x which relates the particle radius to the wavelength is introduced in Eq. 5.1. Here x is used to evaluate the suitable scattering model for a single particle.

$$x = \frac{2\pi}{\lambda} a \tag{5.1}$$

The dashed lines in Fig.5.1 represent constant value of x which describe the boundaries between the appropriate scattering model for the scattering from the particle. The graph does not cover L-band but it can be extended to any frequency taking into consideration x values at the boundary.

In radar remote sensing applications, the particle radius is usually much smaller than the wavelength. For L-band most of the particles that contribute

significantly to the volume scattering have dimensions that lay in the region of Rayleigh or Mie scattering.

5.2 Rayleigh Scattering

For a free charged particle, the scattering of the electromagnetic wave follows the Thomson scattering theorem [84]. The electric field of the incident wave accelerates the charged particle, causing it to emit radiation at the same frequency as the incident wave, and thus the wave is scattered. Thomson theorem holds as long as the motion of the particle has a speed that is much less than the speed of light. The particle oscillates following excitation by the incident electric field, and for a linearly polarised case the particle oscillate along a path resembling a dipole.

In the case of a harmonically bound charged particle, the particle oscillates sinusoidally with a certain frequency. The bound charged particle can be forced (driven) by the incident wave to oscillate with the wave's frequency. When the driving frequency is much lower than the free oscillation frequency of the bound charged particle, then the electric field is nearly static for the particle and the dipole moment is directly proportional to it [84]. This scattering is called Rayleigh scattering and the relation between the dipole moment and the electric field defines the polarisability which is static for this case [91].

For particle dimensions that are very small compared to the wavelength, the charges on the circumference of the particle are excited by the incident electromagnetic field and move within the particle similarly to a driven harmonically bound charged particle by a frequency lower than its free oscillation frequency.

This charge movement on the particle holds only when the electric field is constant inside the particle. Changes of the field inside the dipole are negligible when the particle size is small compared to the wavelength inside the particle [91]. This leads to the following condition for Rayleigh scattering

$$\frac{2\pi\sqrt{\epsilon_r}}{\lambda} a \ll 1, \quad (5.2)$$

where ϵ_r is the particle's relative permittivity.

For a spherical particle, the oscillating charges follow the exciting electromagnetic wave independently from the orientation because of the symmetry of the sphere. In case of a dipole shaped particle, the charges can only move along the dipole axis following the projection of the incident field on the dipole axis. These two extreme particle shapes are not found in natural environments. More realistic are spheroidal particles (prolate and oblate) with one major axis and two equal minor axes. According to [91] these three axes define the particle

polarisabilities p_1, p_2 and p_3 . The incident electric field is projected on each polarisability and the sum of those projections determines the movement of the charges on the particle. The mathematical derivation of the scattered field for each particle shape (sphere, dipole and ellipsoid) is given in the following.

5.2.1 Sphere Shaped Particle

To obtain the particle scattering matrix, a spherical coordinate system that describes the orientation of the particle, the incident wave, and the scattered wave is considered as shown in Fig. 5.2a.

A spherical coordinate system is easier for describing the scattered fields and the orientation of the particle in the three-dimensional space. The center of the coordinate system coincides with the particle center as clarified in Fig. 5.2a.

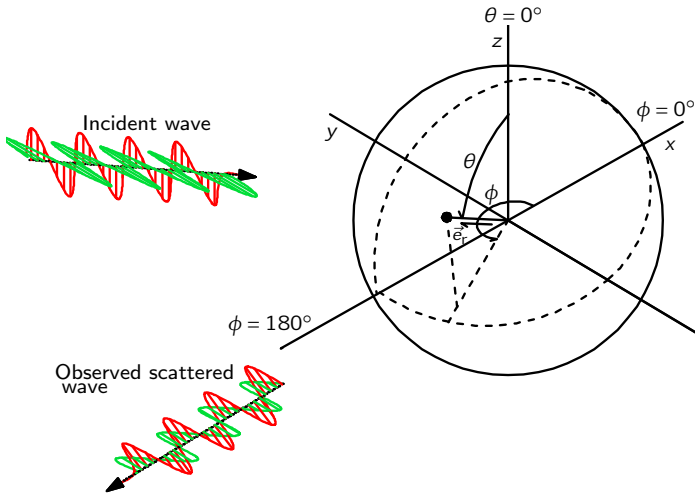
The electromagnetic wave propagates in the direction that is opposite to the radial direction which is $-\vec{e}_r$ with a certain polar angle θ_{inc} and azimuthal angle ϕ_{inc} until it encounters the particle. The scattered electromagnetic wave from the particle is traveling in \vec{e}_r direction, and the considered scattered wave is observed at a certain polar angle θ_{obs} and azimuthal angle ϕ_{obs} . The vertical polarisation for the incident and scattered wave is in the direction of the polar angle \vec{e}_θ when the azimuthal angle $\phi \in [90^\circ, 270^\circ]$, and in the direction of $-\vec{e}_\theta$ when $\phi \leq 90^\circ$ or $\phi \geq 270^\circ$. The direction that is perpendicular on the plane defined by \vec{e}_r and the vertical direction, is the orientation of the horizontal polarisation for both incident and scattered wave.

The scattering matrix for a single spherical particle, where transmitter and receiver are positioned at the same azimuthal angle ($\phi_{obs} = \phi_{inc}$) is obtained by the following equation [91]

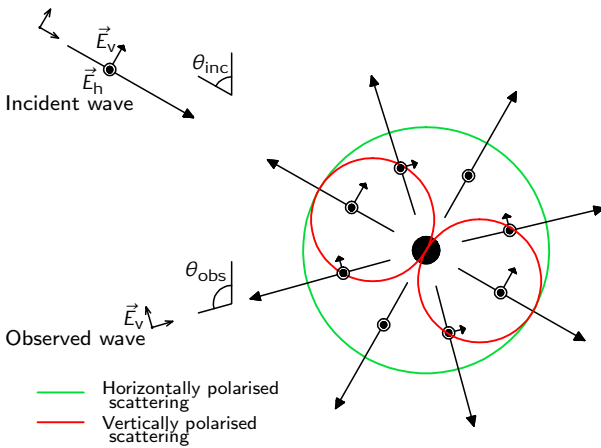
$$\begin{bmatrix} S_{hh}^S & S_{hv}^S \\ S_{vh}^S & S_{vv}^S \end{bmatrix} = j(2\pi)^{3.5} \frac{a^3}{\lambda^3} (m-1) \frac{J_{3/2}\left(\frac{4\pi}{\lambda} a \sin \frac{\pi-d\theta}{2}\right)}{\left(\frac{4\pi}{\lambda} a \sin \frac{\pi-d\theta}{2}\right)^{3/2}} \begin{bmatrix} 1 & 0 \\ 0 & -\cos(\theta_{obs} - \theta_{inc}) \end{bmatrix}, \quad (5.3)$$

where m is the ratio of the particle's refractive index to the refractive index of the background material. $J_{3/2}(x)$ is the Bessel function of the $3/2^{\text{th}}$ order.

The absence of a cross-polar component in the scattered field is due to the symmetric shape of the sphere. By projecting this geometry onto the one of the side-looking SARs, two main scattering properties of the sphere are obtained. First the backscattered power at $\theta_{obs} = \theta_{inc}$ has equal horizontal and vertical component. Second, the scattered power for a bistatic case ($\theta_{obs} \neq \theta_{inc}$), where ϕ is still the same for the transmitter and the receiver, has a higher horizontal than vertical scattered power. This second observation will play a



(a) Spherical coordinate system



(b) Radiation pattern of a sphere over $\phi_{inc} = \phi_{obs} = 180^\circ$

Figure 5.2 Rayleigh scattering for a sphere in a spherical coordinate system; spherical particle in the center of the coordinate system

role in the formulation of the double bounce backscattering from the volume and the subsurface later in Chapter 6.

5.2.2 Dipole Shaped Particle

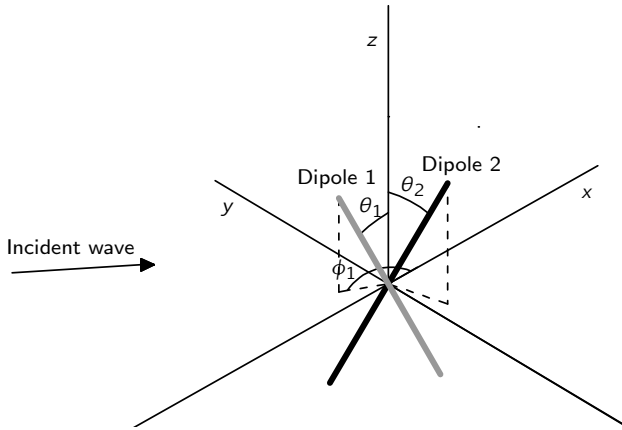
When an electromagnetic wave encounters a dipole only the energy portion of the wave in the polarisation parallel to the dipole orientation excites it. This energy portion of the incident wave can be mathematically obtained by considering the projection of the wave's electric field on the dipole axis. The observed scattered wave is the projection of the induced field by the dipole on the plane that is perpendicular to the Poynting vector of the scattered, linearly polarised wave. Polarisation and amplitude are obtained from the projection as shown in Fig.5.3b.

The scattered wave is the projection of the dipole induced field on the plane that is perpendicular to the Poynting vector of the observed wave. It is a linearly polarised wave whose polarisation and amplitude are obtained from the field generated by the dipole as shown in Fig.5.3b. Regarding the power scattered from a short dipole, it is assumed that the power backscattered from a sphere is similar to the power backscattered from a dipole whose orientation coincides with the polarisation of the incident wave, and has the same characteristic dimension as the sphere.

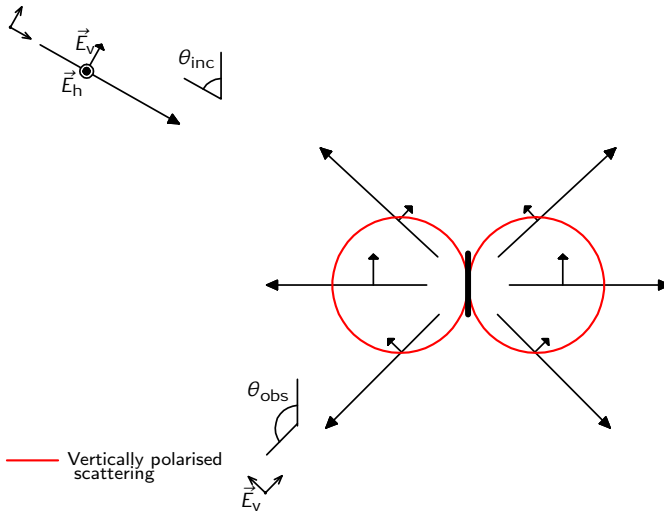
To calculate the scattered field from a dipole, first the projection of the electric and magnetic field of the wave incident on the dipole are required, and then its projection on the predefined horizontal and vertical polarisation axes of the receiver. The solution is a matter of geometry and in the same coordinate system that has been introduced in the previous section (Fig. 5.2a), a dipole oriented along the specified polar angle θ and azimuthal angle ϕ is placed (Fig. 5.3a).

The scattering matrix for a single dipole $H(\theta, \phi)$ (corresponding to Hertzian dipole) which is normalised to the backscattered electric field from a sphere with the same characteristic dimension as for the dipole [91] and where the transmitter and receiver are positioned at the same azimuthal angle ($\phi_{\text{inc}} = \phi_{\text{obs}} = 180^\circ$) is obtained by

$$[H(\theta, \theta_{\text{inc}}, \theta_{\text{obs}}, \phi)] = \begin{bmatrix} S_{hh}^H & S_{hv}^H \\ S_{vh}^H & S_{vv}^H \end{bmatrix}, \quad (5.4)$$



(a) Examples for dipoles in the center of a coordinate system whose orientations can be described by ϕ and θ .



(b) Radiation pattern of a dipole over $\phi_{inc} = \phi_{obs} = 180^\circ$

Figure 5.3 Used coordinate system and radiation pattern for scattering from a short dipole

with

$$\begin{aligned}
 S_{hh}^H &= \frac{(1 - \cos 2\phi)(1 - \cos 2\theta)}{4}, \\
 S_{hv}^H &= \sin 2\phi \cos \theta_{\text{obs}} \frac{1 - \cos 2\theta}{4} - \sin \phi \sin \theta_{\text{obs}} \frac{\sin 2\theta}{2}, \\
 S_{vh}^H &= \sin 2\phi \cos \theta_{\text{inc}} \frac{1 - \cos 2\theta}{4} - \sin \phi \sin \theta_{\text{inc}} \frac{\sin 2\theta}{2}, \\
 S_{vv}^H &= \cos \theta_{\text{inc}} \cos \theta_{\text{obs}} \frac{(1 + \cos 2\phi)(1 - \cos 2\theta)}{4} \\
 &\quad - \sin(\theta_{\text{inc}} + \theta_{\text{obs}}) \cos \phi \frac{\sin 2\theta}{2} + \sin \theta_{\text{inc}} \sin \theta_{\text{obs}} \frac{1 + \cos 2\theta}{2}.
 \end{aligned} \tag{5.5}$$

Here θ_{inc} is the polar angle of the wave incident on the dipole and θ_{obs} is the polar angle in the direction of the receiver. The derivation of Eq. (5.5) is given in Appendix B.

We can see that for a vertically oriented dipole ($\theta = 0^\circ$), $S_{hh} = 0$ and $S_{vv} = \sin \theta_{\text{inc}} \sin \theta_{\text{obs}}$, while for a horizontally oriented dipole ($\theta = \pi/2, \phi = \pi/2$), then $S_{hh} = 1$ and $S_{vv} = 0$. From this we notice that when $\theta_{\text{inc}} \neq \theta_{\text{obs}}$ and for a wide range of orientations, the average S_{hh} is higher than the average S_{vv} , when ϕ is the same for the transmitter and the receiver.

5.2.3 Ellipsoid Shaped Particle

The scattering from a small ellipsoid can be regarded as an intermediate case between scattering from a dipole and a sphere. The main direction of the vertically polarised scattered power is not directed along the Poynting vector of the incident wave like for the sphere case (Fig. 5.2b) nor perpendicular to the orientation of the particle main axis like for the dipole case (Fig. 5.3b), but lies in between depending on the ellipsoid orientation and shape (Fig. 5.4b). That is because the free charges are not bound to the dipole shape anymore and are also not free in their movement as in the case of the sphere. They tend to follow the ellipsoid shape by moving along the long axis.

To model the scattering from a small particle, the particle's *polarisabilities* are considered [91]. The three polarisabilities of a particle are perpendicular to each other and the particle is symmetric around each of them, such that when the incident electric field on the particle is parallel to one of the polarisabilities then the induced dipole moment (the oscillation of the driven harmonically bound charged particle) is parallel to the polarisability vector too. For an incident wave of any polarisation, the scattered field is given by the superposition of the wave scattered on the three polarisabilities, each excited by the projection of the incident field. In other words the scattering from the ellipsoid is equivalent

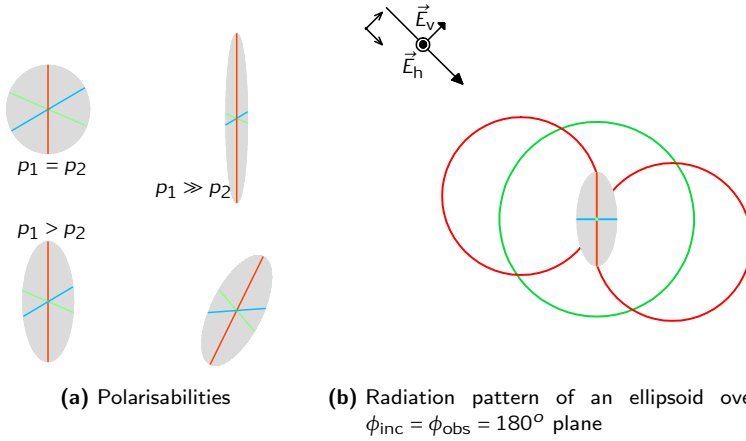


Figure 5.4 Scattering from a small ellipsoid, which is equivalent to the coherent superposition of the scattering from three short dipoles p_1 , p_2 , and p_3

to the total scattering from the three short dipoles (polarisabilities) that are perpendicular to each other and aligned along the principle axes of the ellipsoid as shown in Fig. 5.4a. Accordingly, the scattered wave from the ellipsoid is obtained by

$$\begin{aligned}
 [E(\theta, \theta_{\text{inc}}, \theta_{\text{obs}}, \phi)] &= \begin{bmatrix} S_{\text{hh}}^E & S_{\text{hv}}^E \\ S_{\text{vh}}^E & S_{\text{vv}}^E \end{bmatrix} = p_1 \cdot [H(\theta, \theta_{\text{inc}}, \theta_{\text{obs}}, \phi)] \\
 &+ p_2 \cdot [H(\theta + \pi/2, \theta_{\text{inc}}, \theta_{\text{obs}}, \phi)] \\
 &+ p_2 \cdot [H(\theta + \pi/2, \theta_{\text{inc}}, \theta_{\text{obs}}, \phi + \pi/2)],
 \end{aligned} \tag{5.6}$$

where p_1 is the polarisability parallel to the main axis of the ellipsoid, while $p_2 = p_3$ are the polarisabilities of each of the minor axes.

By substituting $[H(\cdot)]$ from Eq. (5.4), the elements of the scattering matrix can be written as

$$\begin{aligned}
 S_{hh}^E &= \frac{(1 - \cos 2\phi)(1 - \cos 2\theta)(p_1 - p_2) + 4p_2}{4}, \\
 S_{hv}^E &= \left(\sin 2\phi \cos \theta_{\text{obs}} \frac{1 - \cos 2\theta}{4} - \sin \phi \sin \theta_{\text{obs}} \frac{\sin 2\theta}{2} \right) (p_1 - p_2), \\
 S_{vh}^E &= \left(\sin 2\phi \cos \theta_{\text{inc}} \frac{1 - \cos 2\theta}{4} - \sin \phi \sin \theta_{\text{inc}} \frac{\sin 2\theta}{2} \right) (p_1 - p_2), \\
 S_{vv}^E &= \cos \theta_{\text{inc}} \cos \theta_{\text{obs}} \frac{(1 + \cos 2\phi)(1 - \cos 2\theta)(p_1 - p_2) + 4p_2}{4} \\
 &\quad - \sin(\theta_{\text{inc}} + \theta_{\text{obs}}) \cos \phi \frac{\sin 2\theta}{2} (p_1 - p_2) \\
 &\quad + \sin \theta_{\text{inc}} \sin \theta_{\text{obs}} \frac{(p_1 + p_2) + (p_1 - p_2) \cos 2\theta}{2}.
 \end{aligned} \tag{5.7}$$

The particle anisotropy $A_p = p_1/p_2$ describes the shape of the particle. Spherical particles are given by $A_p = 1$: the superposition of three equal polarisabilities yield to a scattering similar to the one described in Eq. (5.3). A value of $A_p > 1$ describes prolate shapes (needle like), while $A_p < 1$ describes oblate shapes (disc like).

The spheroid scattering equation is more complex than the equations for sphere and dipole, but it covers a more realistic and a wider variation of particle shapes. The power scattered from an ellipsoid is considered similar to the power scattered from a Rayleigh sphere (Eq. (5.3)) and from a dipole both are of the same characteristic dimension. The shape of the ellipsoid only influences the polarimetric signature.

5.3 Mie Scattering

When the particle dimensions are comparable to the wavelength ($x \approx 3$), see Eq. 5.1) then the field induced on the particle is no longer constant, because of the different phases of the wave incident on the boundary between the particle and the background. To obtain the exact formulation of the scattering from such particles, Maxwell's equations must be solved across the boundary between the particle and the background material. The solution is rather complex. In general it shows that when the particle size increases, then the forward scattering will dominate over the backward scattering as shown in Fig. 5.5, [10].

As discussed in the previous sections the phase difference between the horizontal and vertical backscattering for the Rayleigh case is either 0 or π . For

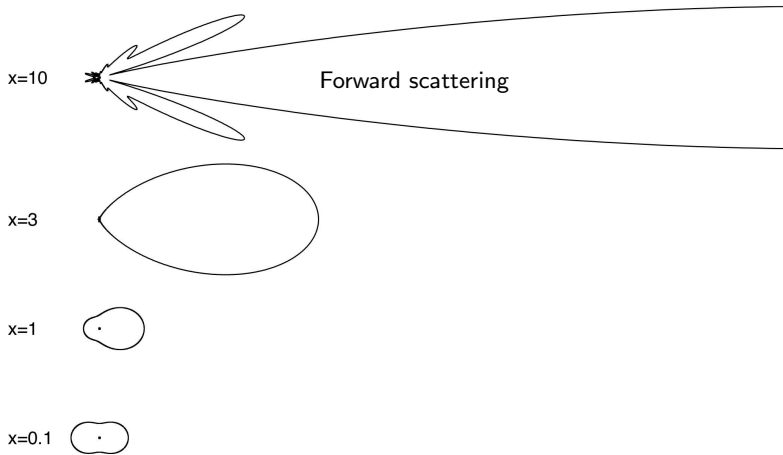


Figure 5.5 Angular distribution of the scattered power for Rayleigh scattering $x = 0.1$ and Mie scattering $x = \{1, 3, 10\}$ [10]

Mie scattering, this phase difference is 0 or π only at $\theta_{\text{obs}} - \theta_{\text{inc}} = \{0, \pi\}$, while a certain shift is expected at other observation angles. Since the particle size compared to L-band wavelength in ice lies mostly in the Rayleigh scattering region, Rayleigh scattering is the main focus of this research, and only a brief description of the polarimetric scattered field for Mie sized objects (sphere, dipole, and ellipsoid) is presented in the following subsections.

5.3.1 Sphere Shaped Particle

The scattering from a sphere of arbitrary radius and material had been derived by solving Maxwell's equation [65]. The solution includes an infinite series that can be found in [91]. In this sense the Rayleigh solution is an approximation of the Mie solution that takes into account only the first term of the series: When the radius of the sphere is considerably smaller than the wavelength then the Mie scattering acts similar to Rayleigh scattering with a higher forward than backward scattered power. For larger spherical particles, the scattering pattern is more complex with several zeros and sidelobes, which can be seen by solving the Mie series.

5.3.2 Dipole Shaped Particle

The concept of traveling wave antennas can describe the scattering from a long dipole [73]. Since the dipole is long, the induced current is not constant,

but has a certain change of phase due to the different propagation distance of the incident wave. The changing phase in the induced current for a vertically oriented dipole can be written as

$$I(z) = I \exp\left(j \frac{2\pi}{\lambda} z \cos \theta_{\text{inc}}\right), \quad (5.8)$$

where z is between $-l/2$ and $l/2$ and l is the length of the dipole. In this sense, the scattered wave is proportional to the spatial Fourier inverse of the surface current on the dipole, which is also known as the radiation vector [73]

$$E_{\text{VV}}, H_{\text{VV}} \propto jk \frac{e^{jkr}}{4\pi r} \sin \theta \int_{-l/2}^{l/2} I(z) e^{jkz \cos \theta} dz. \quad (5.9)$$

In the case of long dipole, $I(z)$ in Eq. (5.8) is substituted in Eq. (5.9) and this leads to

$$\begin{aligned} E_{\text{VV}}, H_{\text{VV}} &\propto \sin \theta \int_{-l/2}^{l/2} I e^{jkz \cos \theta_{\text{inc}}} e^{jkz \cos \theta} dz \\ &= Il \sin \theta \cdot \frac{\sin\left(\frac{kl}{2}(\cos \theta_{\text{inc}} + \cos \theta)\right)}{\frac{kl}{2}(\cos \theta_{\text{inc}} + \cos \theta)}. \end{aligned} \quad (5.10)$$

The phase shift in the induced current is described by the exponent term $j2\pi/\lambda z \cos \theta_{\text{inc}}$, and corresponds to a $\sin(x)/x$ function in the angular distribution, where the $\sin(x)/x$ peak is at $\theta = \pi - \theta_{\text{inc}}$ and $\theta = \pi + \theta_{\text{inc}}$. The \cos -function within the $\sin(x)/x$ widens the maximum of the main lobe, and increases the slope at the edge of the main lobe. The resulting beam is shown in Fig. 5.6. Equation (5.10) also contains an angle ($\theta_{\text{obs}}, \theta_{\text{inc}}$) dependent phase term.

Due to the directivity of the long dipole, a random volume of long dipoles has a larger scattering in the forward direction of the whole volume than the backward direction.

The scattering from a short dipole is an approximation of the general approach for the long dipole with consideration of the impulse like spatial distribution of the induced current on the short dipole $I(z) = \delta(z)$. In this sense, the integral becomes a uniform function and $E_{\text{VV}}, H_{\text{VV}} \propto \sin \theta$. This is the angular distribution observed in Section 5.2.2.

5.3.3 Ellipsoid Shaped Particle

Ellipsoid scattering is expected to behave as an intermediate case between a dipole and a sphere scattering. Solving Maxwell's equations on the boundary of

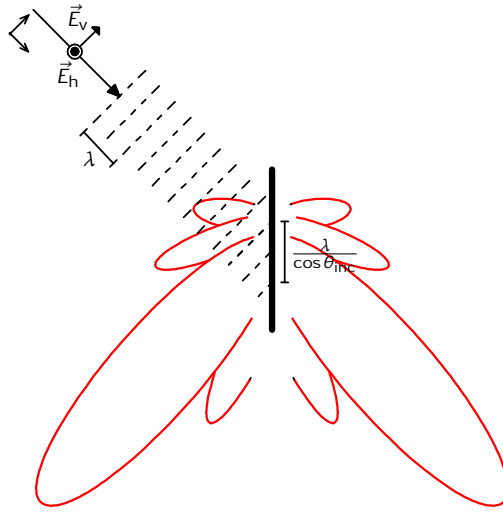


Figure 5.6 Radiation pattern of a long dipole

the ellipsoid (or using numerical programs to do so) leads to an exact solution. Further investigations regarding modelling the ellipsoid with long dipoles will not be treated in this work.

5.4 Coherency Matrix for a Cloud of Particles

Because particles do not normally exist alone, investigating a cloud containing particles of different sizes, shapes and orientations is required. The total scattering is given by the sum of the scattering from all particles, where each one has a different phase. Thus the scattered electric field for the arrangement shown in Fig. 5.7 can be calculated as follows [91]

$$E_s = E_i [S] \sum \frac{1}{jkr} e^{jk(x^2+y^2)/2r}. \quad (5.11)$$

where $[S]$ is the single particle scattering matrix, x and y are the two dimensional displacement of the single particle within the volume from the shortest path between the incident wave and the receiver. The sum can be replaced with an integral over the volume dimensions and hence the electric field is calculated as

$$E_s = E_i \frac{2\pi}{k^2} N I [S], \quad (5.12)$$

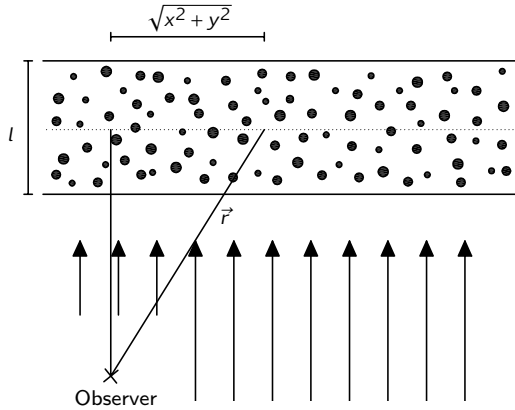


Figure 5.7 Scattering from a distributed volume of particles

where N is the volume density and l the thickness of the volume layer. The magnetic field is equivalent to the electric field divided by the free space impedance (i.e. $H = E/\eta$), with a direction that is perpendicular to the electric field and the propagation direction.

The power scattered by the volume depends on the volume density, depth, the wavelength and the scattering of the single particle. Equation (5.3) indicates that the scattering from a single particle depends mainly of the particle size and on the material's dielectric properties, while the particle shape influences only the polarimetric signature of the scattered field.

By evaluating the entropy-alpha values obtained from the eigen-decomposition of the coherency matrices introduced in Section 2.4, the polarimetric signature is characterized. For small particles, the scattering matrix in Eq. (5.6) is used to calculate the coherency matrix. By setting $p_1 = p_2 = p_3$ in the equation the scattering matrix of a sphere is obtained, while the dipole coherency matrix corresponds to $p_1 = 1, p_2 = p_3 = 0$. Substituting θ_{obs} and θ_{inc} by the local incident angle θ_L , the volume backscattering for the monostatic case is obtained. Then the corresponding coherency matrix is calculated according to Eq. (2.7). The averaging in the equation is done here by integrating over different orientation angles

$$[T_V] = \int_0^{2\pi} \int_0^{\theta_{\text{orientation}}} \vec{k}_P(\theta, \phi) \cdot \vec{k}_P^*(\theta, \phi) \cdot P(\theta) d\theta d\phi, \quad P(\theta) = \frac{\sin \theta}{4\pi}, \quad (5.13)$$

where $P(\theta)$ is the probability density function of the orientation angle of the dipoles in the volume. The integral covers the upper half of a sphere. The

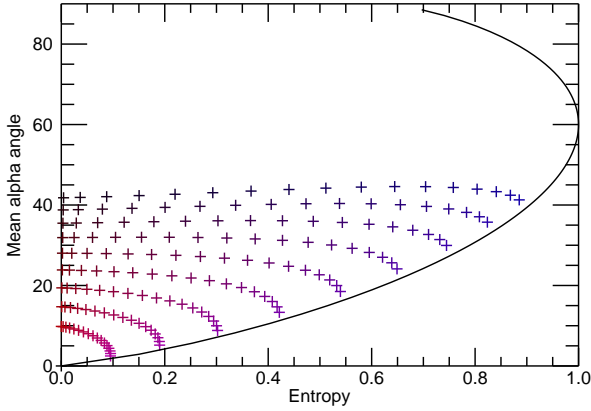


Figure 5.8 Entropy–alpha distribution for the backscattering from a volume of ellipsoids at 90° local incident angle, where the red colour indicates the change in shape from dipoles (dark red) to spheres (bright red) and blue the change in orientation from totally oriented (dark blue) to randomly oriented (bright blue) particles

probability density of the orientation angles presented in Eq. (5.13) maintains a homogeneous (uniform) distribution of orientations in the 3D space.

By applying the above described integration, the coherency matrix for the volume backscattering can be obtained for any local incident angle, orientation distribution, and particle shape. The resulting entropy-alpha distribution of the volume scattering for 90° local incident angle is presented in Fig. 5.8. The red color indicates a spherical shaped particle (lower A_p , where $A_p \in [1, \infty)$), and the blue color indicates a rather randomly oriented volume (higher $\theta_{\text{orientation}}$, where $\theta_{\text{orientation}} \in [0^\circ, 90^\circ]$). The plot is similar to the one obtained in [12], which indicates that both approaches are almost equivalent. The plot shows that the alpha value depends mainly on the particle shape, while it remains widely independent of the width of the orientation distribution, that is influencing the entropy value.

Different local incident angles do not really influence the power scattered from the volume, contrary to the surface backscattering whose power drops fast with increasing local incident angle. The alpha value for the volume slightly decreases for larger local incident angles, but it shows a higher independency from the local incident angle when the volume is more random (the region of the maximum entropy line), as can be seen in Fig. 5.9 in comparison to Fig. 5.8.

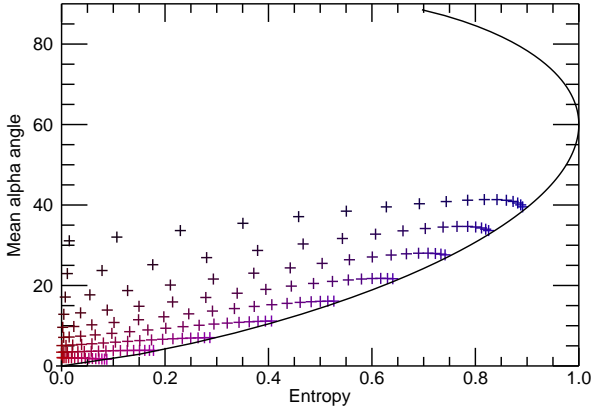


Figure 5.9 Entropy–alpha distribution for the backscattering from a volume of ellipsoids at 25° local incident angle for the same samples shown in the previous figure

The large particles act similar to the small particles regarding the volume backscattering in the monostatic case. For the bistatic case and for second order scattering, the $\sin(x)/x$ radiation pattern described in Eq. (5.10) is required for calculating the Pauli vector.

This approach of calculating the volume scattering can be adapted to calculate any volume distribution. By substituting θ_{inc} with the local incident angle of the transmitter and θ_{obs} with the local incident angle of the receiver, the volume scattering for the bistatic case is obtained.

Chapter 6

Multiple Scattering (Dihedral Backscattering)

When a wave is scattered by only one localised scattering centre, the process is called single scattering. In the presence of several scattering centres, the wave can undergo several scattering interactions before being received, which is known as multiple scattering. The coherency matrix for this process is not the sum of the particles' coherency matrices nor the multiplication, as the interaction process has a coherent polarimetric effect. Therefore the scattering matrix for the multiple scattering process is considered before generating the corresponding coherency matrix of geometrically distributed scatterers.

With the presence of a subsurface under a volume, multiple scattering can occur as a scattering at a particle in the volume combined with a reflection at the subsurface interface. Such second-order scattering contributions can be as large as or even larger than the single scattering contributions of volume or surface backscattering, as the specular reflection at the subsurface can have negligible losses. Hence the second order scattering can not be ignored in modelling a two-layer structure. In certain applications, for example in [6], it is possible to observe the multiple scattering separated from the single scattering, such that its impact on the total backscattering can be demonstrated.

For a side-looking SAR system, a commonly observed second-order scattering mechanism specially in urban areas and forests is the dihedral. Therefore the same term *dihedral backscattering* is used here to refer to the backscattering from a volume scattering that is reflected back by the subsurface. Due to the decreased power of higher order scattering contributions, terms of higher order than two are not considered in the following.

The formulation of the volume-subsurface backscattering considers the coherent addition of the scattering from first subsurface then particle and first

particle then subsurface components. The calculation of the backscattering from a volume of spheres and a subsurface is introduced first, then for volumes of dipoles and ellipsoids. In the last section of this chapter, the fact that the particles are geometrically distributed is considered in calculating the coherency matrix and the power backscattered from this scattering mechanism.

6.1 Sphere Shaped Particles

The scattering from the sphere is presented in Eq. (5.3). The part of the scattered power that participates in the dihedral scattering is the one whose specular reflection from the subsurface is directed to the receiver. By considering a flat subsurface, the scattering from the volume that is reflected back to the monostatic radar is the portion that is directed to the angle $\theta_{\text{obs}} = \pi - \theta_L$, such that the angle between the incident and the observed wave is $\theta_{\text{obs}} - \theta_{\text{inc}} = \pi - 2\theta_L$. From the above, the scattering matrix of a dihedral which consists of a sphere and a subsurface that is normalised to the backscattered electric field from the sphere one can be written as

$$\begin{bmatrix} S_{hh}^{D,S} & S_{hv}^{D,S} \\ S_{vh}^{D,S} & S_{vv}^{D,S} \end{bmatrix} = \begin{bmatrix} R_{\perp} & 0 \\ 0 & R_{\parallel} \cos(\pi - 2\theta_L) \end{bmatrix}, \quad (6.1)$$

where R_{\perp} , R_{\parallel} are the Fresnel coefficients for the subsurface interface.

From this equation, we can see that the backscattering from the particle-subsurface interaction has a larger horizontal backscattering than vertical, as the cosine function is smaller than 1 and $|R_{\parallel}| < |R_{\perp}|$. Since usually R_{\perp} is negative and R_{\parallel} is positive, as can be seen in Eq. (2.27), S_{hh} and S_{vv} are in phase for $\theta_L < 45^\circ$ as the cosine term is negative, and they are out of phase when $\theta_L > 45^\circ$, as shown in Fig. 6.1. The scattering from the sphere which contributes in the dihedral backscattering for local incident angles larger than 45° corresponds to the backward lobe of the Rayleigh scattering angular pattern from the sphere, hence the total co-polar phase difference is 180° which is similar to the conventional dihedral scattering introduced in Section 2.5.2.

For a cloud of spheres, the scattering from it followed by the reflection at the subsurface does not depolarise and corresponds to a zero entropy value and zero cross-polarization component, since a sphere is symmetric and does not change its backscattering with orientation. Figure 6.2 shows the simulated dihedral backscattering (volume of spheres – surface), where the Fresnel coefficients are assumed to be $(1, -1)$. The parameters for the plots can be obtained from the coherency matrix that will be explained in detail in Sec. 6.4. The results are

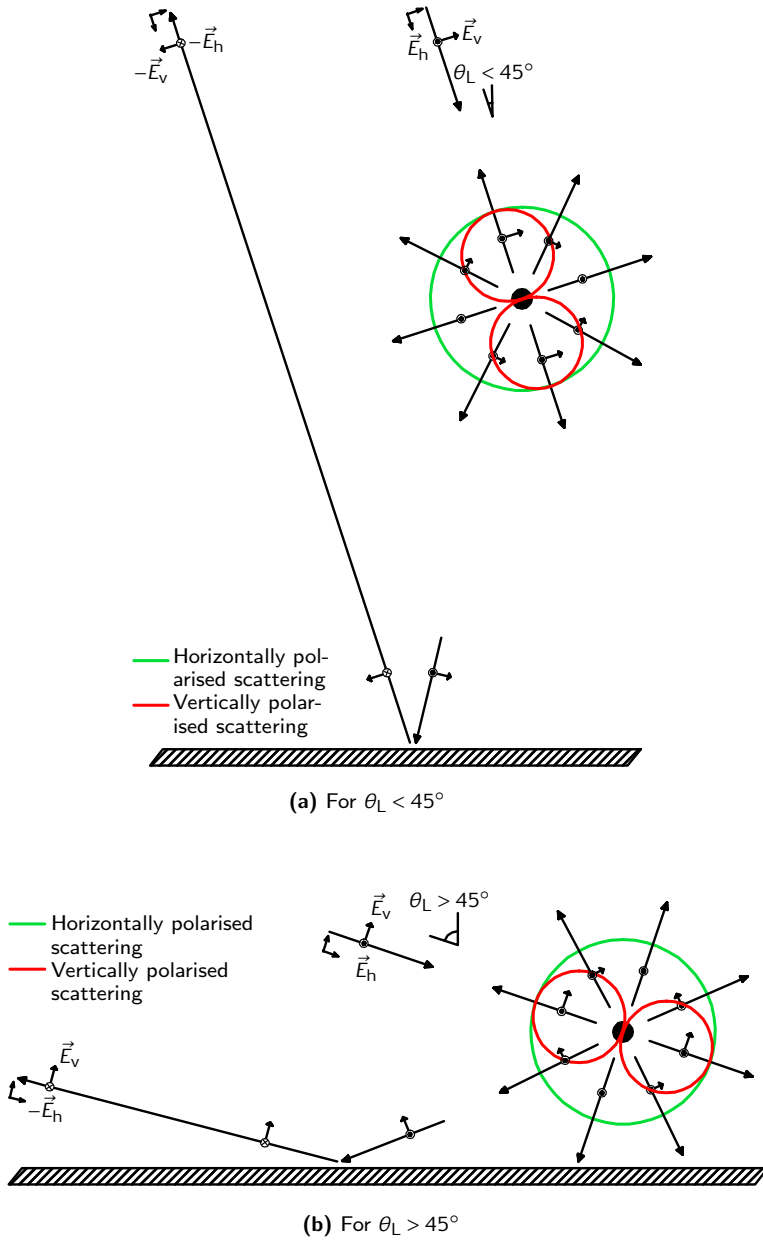


Figure 6.1 The dihedral backscattering from a single sphere and a surface.

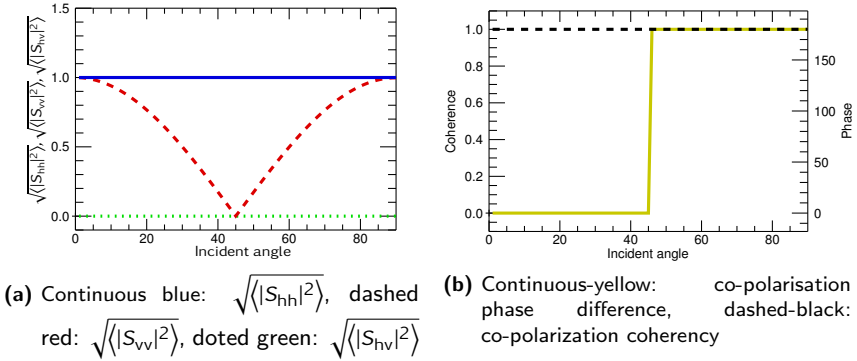


Figure 6.2 Simulated dihedral backscattering (cloud of small spheres – surface), Fresnel coefficients are assumed to be (1, -1)

shown here to illustrate the effect of the specific particle shape on the response of the dihedral. The particle-subsurface dihedral mechanism induces a larger horizontal backscattering than the vertical and both components are in phase for $\theta_L < 45^\circ$.

The dihedral component from a scattering from a large sphere first and then a specular reflection from the subsurface can contribute with larger backscattering than the direct backscattering from the large sphere itself. This can occur when the dimensions of the sphere are in the range of the electromagnetic wavelength, such that Mie scattering theory applies. With Mie theory the scattering from the forward lobe can have a larger power than the scattering from the backward lobe, as explained in Section 5.3, and when the contrast of the permittivity on the subsurface interface is large then most of the power is reflected back in a specular reflection, as shown in Fig. 6.3. The backscattering from this dihedral component has a higher power, when the Mie scattering and specular reflection compensate for the extra propagation attenuation that influences the dihedral backscattering due to the longer propagation path.

6.2 Dipole Shaped Particles

As shown in the previous chapter and particularly in Fig. 5.8 and 5.9 the main difference between the scattering from a cloud of dipoles and a cloud of spheres is the depolarisation induced by the dipole scattering leading to a higher entropy, and the dependency of the scattering on the dipole orientation, since its shape is not symmetric for every orientation. The dihedral backscattering

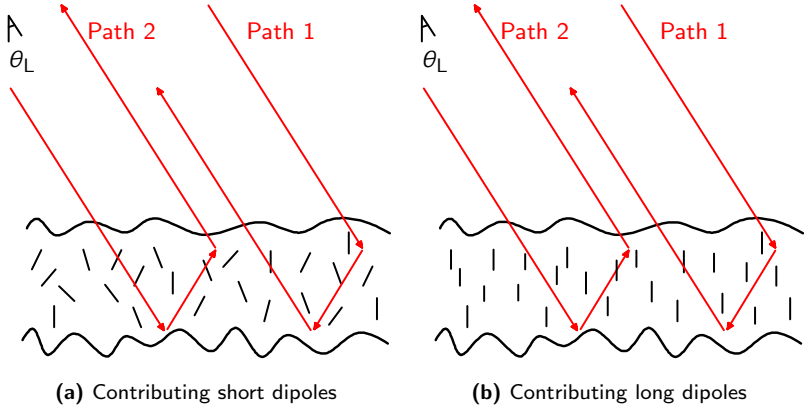


Figure 6.4 Schematic representations of the dipoles contributing to the dihedral backscattering. The contribution of the two propagation paths, represented by the red arrows, are added coherently.

6.2.1 Short Dipole

The direction of the main scattering from a single dipole is perpendicular to the dipole orientation and unlike the long dipoles, the two scattering lobes are wide and, therefore all dipole particles within the volume are considered in the mathematical formulation of the dihedral scattering.

For an electromagnetic wave encountering a dipole at $\theta_{\text{inc}} = \theta_L$, the wave scattered at an angle $\theta_{\text{obs}} = \pi - \theta_L$ is reflected by the subsurface back to the radar. This component is added coherently to the component scattered at the angle $\theta_{\text{obs}} = \theta_L$ from a dipole excited by the wave reflected at the subsurface. This wave reflected at the subsurface encounters the dipole at an angle of $\pi - \theta_L$. Therefore the two paths shown in Fig. 6.4 sum up to

$$\begin{aligned} \begin{bmatrix} S_{\text{hh}}^{\text{D,H}} & S_{\text{hv}}^{\text{D,H}} \\ S_{\text{vh}}^{\text{D,H}} & S_{\text{vv}}^{\text{D,H}} \end{bmatrix} &= \frac{1}{2} \begin{bmatrix} R_{\perp} & 0 \\ 0 & R_{\parallel} \end{bmatrix}^T [H(\theta, \phi)] \Big|_{\substack{\theta_{\text{inc}} = \theta_L \\ \theta_{\text{obs}} = \pi - \theta_L}} \\ &+ \frac{1}{2} [H(\theta, \phi)] \Big|_{\substack{\theta_{\text{inc}} = \pi - \theta_L \\ \theta_{\text{obs}} = \theta_L}} \begin{bmatrix} R_{\perp} & 0 \\ 0 & R_{\parallel} \end{bmatrix}, \end{aligned} \quad (6.2)$$

where the $[H(\cdot)]$ matrix is the normalised scattering matrix of a single dipole discussed in Section 5.2.2, Eq. (5.4). The factor $1/2$ results from averaging the two paths of the dihedral backscattering.

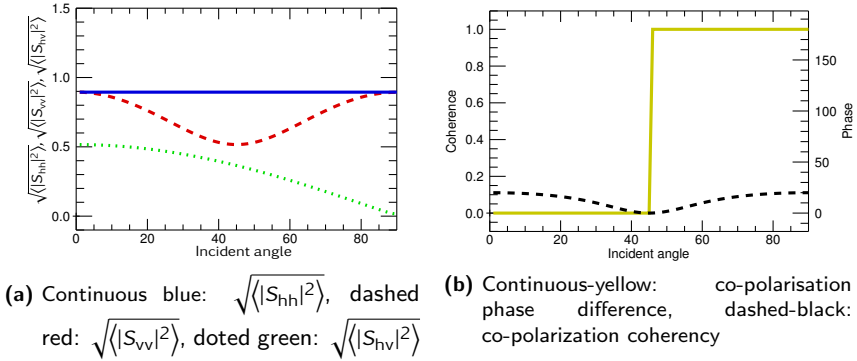


Figure 6.5 Simulated dihedral backscattering (cloud of random short dipoles-surface), Fresnel coefficients are assumed to be $(1, -1)$, see Fig. 6.2.

Then the elements of the scattering matrix can be written as

$$\begin{aligned}
 S_{hh}^{D,H} &= R_{\perp} \frac{(1 - \cos 2\phi)(1 - \cos 2\theta)}{4} \\
 S_{vh}^{D,H} &= S_{hv}^{D,H} = (R_{\perp} - R_{\parallel}) \sin 2\phi \cos \theta_L \frac{1 - \cos 2\theta}{8} - (R_{\perp} + R_{\parallel}) \sin \phi \sin \theta_L \frac{\sin 2\theta}{4} \\
 S_{vv}^{D,H} &= \frac{R_{\parallel}}{2} \left(-\cos^2 \theta_L \frac{(1 + \cos 2\phi)(1 - \cos 2\theta)}{2} + \sin^2 \theta_L (1 + \cos 2\theta) \right).
 \end{aligned} \tag{6.3}$$

The scattering from this dihedral mechanism shows a significant cross-polarisation power that depends of the dipole orientation.

For a cloud of dipoles, due to their non-symmetrical shape, in the case of statistically distributed orientation, a high entropy is expected for the dihedral backscattering from a cloud of dipoles and a subsurface. As an example, Fig. 6.5 shows the simulated backscattering of a dihedral (volume of dipoles – surface), where the Fresnel coefficients are assumed to be $(1, -1)$ and the dipoles are assumed to be randomly oriented (orientation distribution width $\theta_{\text{orientation}} = \pi/2$). The coherency matrix can be obtained according to Sec. 6.4, specifically Eq. (6.9). The results are shown here to illustrate the effect of the specific particle shape on the response of the dihedral. The distribution is similar to the illustration shown in Fig. 6.4a. The dihedral scattering in this case, shows a zero phase between horizontal and vertical backscattering at local incident angles lower than 45° and is out of phase for larger local incident angles, which is similar to the case of a dihedral formed by a cloud of spheres

and the subsurface discussed in the previous section, because the total average of the scattering for a completely random volume of dipoles includes more scattering from the forward lobe of the dipoles than from the backward lobe for smaller angles. If the volume is more vertically oriented, the co-polarization component will be out of phase at smaller local incident angles, as more dipoles will contribute with scattering from the backward lobe than the forward lobe.

The dihedral scattering from a volume of dipoles in combination with a subsurface backscatters more horizontally than vertically polarised power, and results in a zero co-polarization phase for small local incident angles. The scattering has a non-zero cross-polarisation backscattering and a small coherency between the co-polarisation channels. In general this scattering shows a high entropy value.

6.2.2 Long Dipole

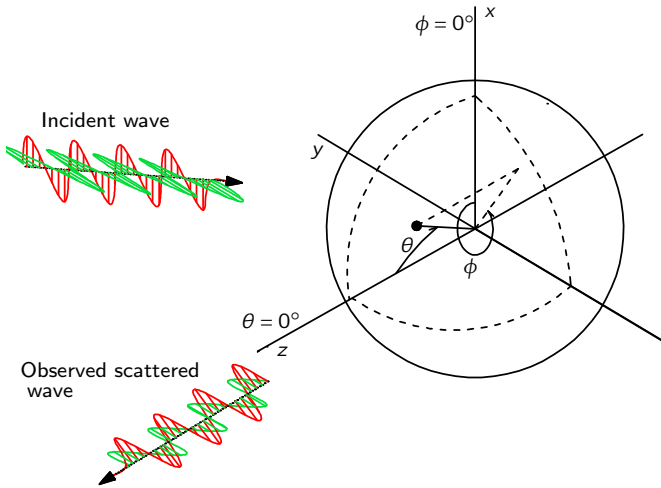
The scattering from a vertically oriented long dipole is directed mainly towards $\pi - \theta_{inc}$, as has been shown in Section 5.3.2. If the dipole is tilted by an angle τ to the line of sight then the beam will be directed to $\pi - \theta_L + 2\tau$, and the main power scattered by the long dipole is not reflected back to the radar system by the subsurface. Because of this directivity, dipoles that are tilted in the line of sight direction contribute with lower dihedral backscattering than dipoles titled with the same angle but around the line of sight.

A simplified approach to calculate the backscattered polarimetric signature from this dihedral mechanism is proposed here which uses the short dipole approach, but considers a different volume distribution as illustrated in Fig. 6.4. The following coordinate system, shown in Fig. 6.6, is used to describe the distribution of the effective volume in a clearer way.

The scattering matrix for a single dipole in this system is equivalent to the scattering matrix of a single dipole in the system shown in Fig. 5.2 for a short dipole, but with replacing θ from the coordinate system of Fig. 5.2 by ϕ and substituting ϕ by $\pi/2 - \theta$.

With this system two distribution widths for the dipole orientation can be modelled. The angle $\phi_{orientation}$ in this system corresponds to the physical orientation distribution of the dipoles, while $\theta_{orientation}$ represents the effective orientation distribution of the dipoles around $\theta = \pi/2$ in the line of sight direction. The effective orientation distribution is always less than the physical orientation distribution $\theta_{orientation} < \phi_{orientation}$ and even much less for longer dipoles, as the beam is more directed and the effective volume is less distributed in the line of sight direction.

For very long dipoles the main beam is narrow and only dipoles located in the plane perpendicular to the subsurface and perpendicular to the incident plane



(a) The rotated spherical coordinate system

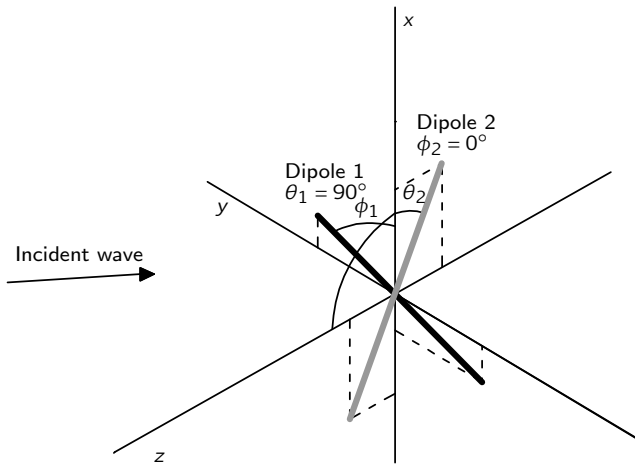
(b) Two long dipoles in the center of a coordinate system oriented one on $\phi = \phi_1$ and the other on $\theta = \theta_2$ angles

Figure 6.6 Adapted coordinate system for the long dipoles/ellipsoids which can describe the distribution of the effective volume along the line of sight \vec{e}_θ and around it \vec{e}_ϕ .

of the wave on the subsurface, that is clarified in Section 4.2.1, contribute to the dihedral backscattering. Therefore the effective volume distribution is only the one shown in Fig. 6.4b. Only this portion of the volume contributes to the dihedral backscattering, while the rest of the volume scatters the wave away from a monostatic receiver. Therefore the scattering matrix for a dihedral of single very long dipole and a subsurface is calculated according to

$$\begin{aligned} \begin{bmatrix} S_{hh}^{D,L} & S_{hv}^{D,L} \\ S_{vh}^{D,L} & S_{vv}^{D,L} \end{bmatrix} &\propto \begin{bmatrix} S_{hh}^{D,H} & S_{hv}^{D,H} \\ S_{vh}^{D,H} & S_{vv}^{D,H} \end{bmatrix} \Bigg|_{\substack{\phi=\pi/2 \\ \theta=\phi}} \\ &= \zeta_{D,L} \begin{bmatrix} R_{\perp}(1 - \cos 2\phi) & -(R_{\perp} + R_{\parallel})\sin \theta_L \frac{\sin 2\phi}{2} \\ -(R_{\perp} + R_{\parallel})\sin \theta_L \frac{\sin 2\phi}{2} & R_{\parallel} \sin^2 \theta_L (1 + \cos 2\phi) \end{bmatrix}, \end{aligned} \quad (6.4)$$

where $\zeta_{D,L}$ is a normalisation factor for the scattered electric field.

For a cloud of long dipoles, since the effective volume of long dipoles is more vertically oriented than for short dipoles, the dihedral backscattering contains a stronger contribution from the backward lobe than from the forward lobe of the dipoles. Accordingly, long dipoles contribute with co-polarization backscattering that is out of phase. Figure 6.7 shows the simulated backscattering of a dihedral formed by a volume of very long dipoles and a subsurface ($\theta_{\text{orientation}} = 0$), where the Fresnel coefficients are assumed to be $(1, -1)$ and the dipoles are assumed to be randomly distributed (orientation distribution width $\phi_{\text{orientation}} = \pi/2$). The coherency matrix can be obtained according to Sec. 6.4, specifically Eq. (6.12). The results are shown here to illustrate the effect of the specific particle shape on the response of the dihedral.

The scattering from a dihedral formed by a volume of long dipoles and the subsurface is almost similar to the scattering of a conventional dihedral, where the horizontal backscattering is larger than the vertical one and out of phase. The cross-polarisation backscattering component is proportional to the sum of the Fresnel coefficients as shown in Eq. (6.4), and it is equal to zero in this example, because of the preassumption of the Fresnel coefficients. This effective volume approach in modelling the backscattering from the dihedral of a volume of long dipoles and a subsurface is a simple way to approximate the backscattering, which can use the same approach as for short dipoles but with a different spatial distribution of the volume.

6.3 Ellipsoid Shaped Particles

The dihedral scattering from a volume of ellipsoids and the subsurface has properties that are between the dihedral formed by a cloud of spheres interacting

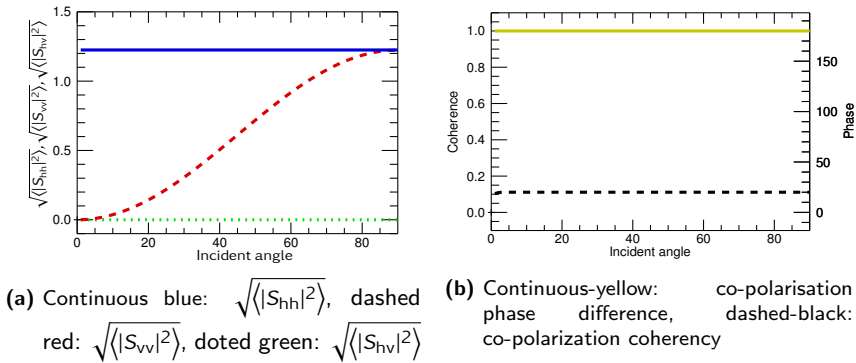


Figure 6.7 Simulated dihedral backscattering (cloud of random long dipoles–surface), Fresnel coefficients are assumed to be $(1, -1)$

with the subsurface and the version with a cloud of dipoles and a subsurface. As mentioned in Chapter 5 the ellipsoid scattering is equivalent to the superposition of the scattering from the three polarisabilities of the ellipsoid as shown in Eq. (5.6). For the dihedral backscattering from an ellipsoid and a subsurface, the scattering from an ellipsoid to the subsurface direction, that is reflected back to the sensor, is added coherently to the scattering from the same ellipsoid in the direction of the sensor that has been excited by the wave reflected on the

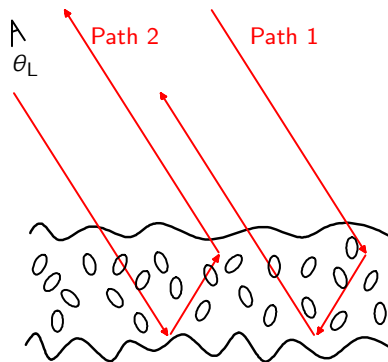


Figure 6.8 Schematic representations of the small ellipsoids contributing to the dihedral backscattering. The contribution of the two propagation paths, represented by the red arrows, are added coherently.

subsurface as shown in Fig. 6.8. Therefore the backscattering from a dihedral of a single ellipsoid and the subsurface is obtained by the following equation

$$\begin{aligned} \begin{bmatrix} S_{hh}^{D,E} & S_{hv}^{D,E} \\ S_{vh}^{D,E} & S_{vv}^{D,E} \end{bmatrix} &= \frac{1}{2} \begin{bmatrix} R_{\perp} & 0 \\ 0 & R_{\parallel} \end{bmatrix}^T [E(\theta, \phi)] \Big|_{\substack{\theta_{\text{inc}}=\theta_L \\ \theta_{\text{obs}}=\pi-\theta_L}} \\ &+ \frac{1}{2} [E(\theta, \phi)] \Big|_{\substack{\theta_{\text{inc}}=\pi-\theta_L \\ \theta_{\text{obs}}=\theta_L}} \begin{bmatrix} R_{\perp} & 0 \\ 0 & R_{\parallel} \end{bmatrix}, \end{aligned} \quad (6.5)$$

where $[E(\theta, \theta_{\text{inc}}, \theta_{\text{obs}}, \phi)]$ is the scattering matrix for an ellipsoid as shown in Eq. (5.6), such that

$$\begin{aligned} S_{hh}^{D,E} &= R_{\perp} \frac{(1 - \cos 2\phi)(1 - \cos 2\theta)(p_1 - p_2) + 4p_2}{4} \\ S_{vh}^{D,E} &= S_{hv}^{D,E} = \left((R_{\perp} - R_{\parallel}) \sin 2\phi \cos \theta_L \frac{1 - \cos 2\theta}{8} \right. \\ &\quad \left. - (R_{\perp} + R_{\parallel}) \sin \phi \sin \theta_L \frac{\sin 2\theta}{4} \right) (p_1 - p_2) \\ S_{vv}^{D,E} &= \frac{R_{\parallel}}{2} \left(-\cos^2 \theta_L \frac{(1 + \cos 2\phi)(1 - \cos 2\theta)(p_1 - p_2) + 4p_2}{2} \right. \\ &\quad \left. + \sin^2 \theta_L ((p_1 + p_2) + (p_1 - p_2) \cos 2\theta) \right). \end{aligned} \quad (6.6)$$

For a cloud of ellipsoids, Fig. 6.9 shows the simulated backscattering of a dihedral (volume of ellipsoids–surface), where the Fresnel coefficients are assumed to be $(1, -1)$ and the ellipsoids are assumed to be randomly oriented. The coherency matrix can be obtained according to Sec. 6.4. The results are shown here to illustrate the effect of the specific particle shape on the response of the dihedral. The particle shape is defined by $A_p = 3$. The plots show values that lay between the curves obtained with a dihedral of a volume of dipoles and a surface and the one of a volume of spheres and a surface. The horizontal is still larger than the vertical backscattering, and the co-polarisation phase at small local incident angles is zero.

For the dihedral of a volume of large ellipsoids and the subsurface the same approach as discussed for the long dipole can be used to estimate the dihedral scattering and only a portion of the volume is considered according to the geometry clarified in Fig. 6.6. The single ellipsoid scattering matrix in the geometry of Fig. 6.6 is similar to the one shown in Eq. (6.6) with substituting θ by ϕ and ϕ by $\pi/2 - \theta$.

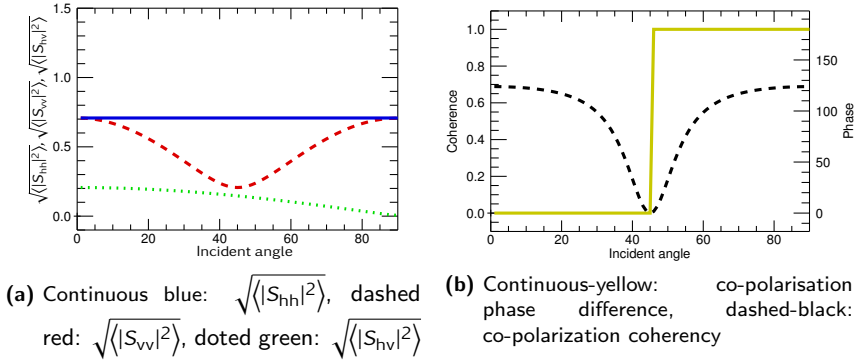


Figure 6.9 Simulated dihedral backscattering (cloud of small random ellipsoids ($A_p = 3$) –surface), Fresnel coefficients are assumed to be (1, -1)

6.4 Coherency Matrix for a Dihedral of a Cloud of Particles and a Subsurface

The power backscattered from the mechanism using a cloud of particles and a subsurface is equivalent to the power backscattered from the volume with an attenuation arising from the propagation through the volume and a reflection at the subsurface, as shown in Eq. (6.7). As the experimental data show a zero copolar phase shift, the extinction through the volume is neglected assuming small particles compared to the wavelength and distributed in a layer of only one metre and a half thickness (small depth).

$$\sigma_{\text{dihedral}} = |R_{\perp/\parallel}|^2 \cdot e^{(2k \cos \theta)^2 \sigma_{\text{rms}}^2} \cdot \sigma_{\text{volume}}(\theta_{\text{obs}} = \pi - \theta_{\text{inc}}). \quad (6.7)$$

At lower frequencies, such as *L*-band, a roughness in the range of centimetres is already small enough to drive the exponent term close to one, such that the attenuation of the forward volume scattering depends mainly on the reflection coefficients, which are discussed in Section 4.2.1. Therefore the contribution of the dihedral scattering is highly dependent on the subsurface's physical properties.

The polarimetric signature of the dihedral scattering from a volume of ellipsoids and a subsurface is evaluated and compared to the polarimetric signature of a volume scattering by calculating its corresponding coherency matrices according to Eq. (2.13), and the entropy-alpha values are obtained from eigen-decomposition, discussed in Section 2.4. The averaging for obtaining the coherency matrix is performed here by integrating over different angles of

volume orientation, similar to the concept applied in Eq. (5.13), but with the dihedral scattering matrix instead of the one for the particle backscattering. The Pauli vector used to evaluate the integral is obtained from the scattering matrix for the dihedral of an ellipsoid and a subsurface shown in Eq. (6.6). For the general case regarding particle shape and orientation distribution, a symbolic integration, using a computer algebra package e.g. Maple core [64] for Matlab, can be performed to obtain numerical results of the coherency matrix.

For the specific case of a random volume of short dipoles with a uniform orientation distribution reflected back by the subsurface the scattering matrix in Eq. (6.6) with $p_1 = 1$ and $p_2 = 0$, which is equivalent to Eq. (6.3), is substituted in Eq. (2.7) to generate the corresponding Pauli vector. Then a closed form of the coherency matrix, introduced in Eq. (2.13), is obtained by applying basic integration rules and integrating over different angles of volume orientation, similar to Eq. (5.13). The upper limit $\theta_{\text{orientation}}$ in the integration is set to $\pi/2$ to represent a random volume for this case. The solution of the integral had also been verified using computer algebra program (Maple) [64]. The coherency matrix results as follows:

$$[T_3^{D,H}] = \frac{R_{\text{Volume}}}{2} \begin{bmatrix} t_1^{D,H} & t_2^{D,H} & 0 \\ t_2^{D,H*} & t_4^{D,H} & 0 \\ 0 & 0 & t_6^{D,H} \end{bmatrix}, \quad (6.8)$$

where R_{Volume} is the power contribution of the volume backscattering as introduced in Section 2.5.3 and

$$\begin{aligned} t_1^{D,H} &= 1.5R_{\perp}^2 + R_{\parallel}R_{\perp} \left(1 - 2\cos^2\theta_L\right) + R_{\parallel}^2 \left(1.5 - 4\cos^2\theta_L + 4\cos^4\theta_L\right) \\ t_2^{D,H} &= 1.5R_{\perp}^2 - R_{\parallel}^2 \left(1.5 - 4\cos^2\theta_L + 4\cos^4\theta_L\right) \\ t_4^{D,H} &= 1.5R_{\perp}^2 - R_{\parallel}R_{\perp} \left(1 - 2\cos^2\theta_L\right) + R_{\parallel}^2 \left(1.5 - 4\cos^2\theta_L + 4\cos^4\theta_L\right) \\ t_6^{D,H} &= 0.5R_{\perp}^2 + R_{\parallel}R_{\perp} \left(1 - 2\cos^2\theta_L\right) + 0.5R_{\parallel}^2. \end{aligned} \quad (6.9)$$

For large ellipsoids the coordinate system shown in Fig. 6.6 is considered and the integral is evaluated over the effective volume, clarified in Section 6.2.2 and 6.3, with a homogeneous distribution as shown is the following equation

$$[T_{\text{dihedral}}] = \int_{\phi=\pi/2-\theta_{\text{orientation}}}^{\pi/2+\theta_{\text{orientation}}} \int_{\theta=-\phi_{\text{orientation}}}^{\phi_{\text{orientation}}} \vec{k}_p(\theta, \phi) \cdot \vec{k}_p^*(\theta, \phi) \cdot P(\theta) d\theta d\phi, \quad (6.10)$$

$$P(\theta) = \frac{\sin\phi}{4\pi}.$$

The vector \vec{k}_p in the equation above corresponds to the Pauli vector of a small ellipsoid. The angles θ and ϕ are replaced by ϕ and $\pi/2 - \theta$ by changing the integral limits compared to Eq. (5.13). The integral covers the upper half of a sphere.

The coherency matrix for the backscattering for the specific case of a randomly oriented volume of long dipoles reflected back by the subsurface can be obtained in a closed form by applying basic integration rules and solving the integral above with the limits $\phi_{\text{orientation}} = \pi/2$ and $\theta_{\text{orientation}} = 0$. The solution of the integral had also been verified using computer algebra program (Maple) [64] and is as follows:

$$\left[T_3^{D,L} \right] = P_{D,L} \begin{bmatrix} t_1^{D,L} & t_2^{D,L} & 0 \\ t_2^{D,L*} & t_4^{D,L} & 0 \\ 0 & 0 & t_6^{D,L} \end{bmatrix} \quad (6.11)$$

where $P_{D,L}$ is the power contribution of the dihedral backscattering from long dipoles and a subsurface, and

$$\begin{aligned} t_1^{D,L} &= 1.5R_{\perp}^2 + R_{\parallel}R_{\perp} \sin^2 \theta_L + 1.5R_{\parallel}^2 \sin^4 \theta_L \\ t_2^{D,L} &= 1.5R_{\perp}^2 - 1.5R_{\parallel}^2 \sin^4 \theta_L \\ t_4^{D,L} &= 1.5R_{\perp}^2 - R_{\parallel}R_{\perp} \sin^2 \theta_L + 1.5R_{\parallel}^2 \sin^4 \theta_L \\ t_6^{D,L} &= 0.5 \sin^2 \theta_L (R_{\parallel} + R_{\perp})^2. \end{aligned} \quad (6.12)$$

The entropy-alpha values for the dihedral backscattering from a volume of small ellipsoids reflected by the subsurface at 25° local incident angle and a large permittivity for the subsurface material ($80 + j \cdot 20$), referring to water as discussed in Section 4.1.1, are shown in Fig. 6.10. The points correspond to the same values for shape and orientation as the points in Fig. 5.8 and 5.9.

In general the points show a larger alpha value, indicating a larger co-polarization ratio due to the reflection coefficient that increases the horizontal polarisation compared to the vertical one. The points cover also a wider range of entropy-alpha values including the region of the conventional double bounce discussed in Section 2.4.2. This region is covered by a volume of vertically highly oriented, almost dipole shaped particles as the dihedral backscattering includes more scattering from the backward scattering lobe of the particles than from the forward scattering lobe and the co-polarization backscattering is out of phase, see Section 6.2.1. Because of the influence of the backward/forward lobe contributions in the dihedral scattering mechanism, the alpha value is highly dependent on both the shape and the orientation distribution of the

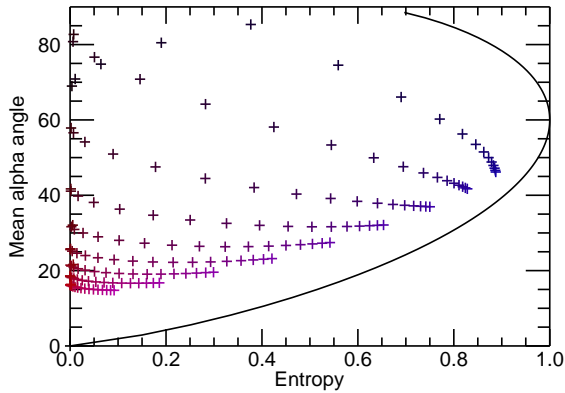


Figure 6.10 Entropy–alpha distribution for the dihedral backscattering of a cloud of small ellipsoids-subsurface at 25° local incident angle and subsurface permittivity of $(80 + j \cdot 20)$, where the red colour indicates the shape from dipole (dark red) to spheres (bright red) and blue describes the orientation from totally oriented (dark blue) to randomly oriented (bright blue) particles

particles, unlike the volume backscattering whose alpha is mainly dependent on the particle shape.

Some areas of the entropy-alpha distribution of this dihedral mechanism overlap with areas covered by the backscattering from the volume. Nevertheless the backscattering here is different as it has a higher backscattering from the horizontal polarisation than the vertical polarisation. This higher ratio of S_{nh}/S_{vv} than expected for a Bragg surface and a partially vertically oriented volume is also observed in ALOS data, as discussed in Chapter 3. Therefore this scattering mechanism plays a significant role in the backscattering from the subarctic lakes.

Chapter 7

Two-Layer Structure Ice–Subsurface: Theoretical Model and Observed Data

This chapter addresses the complete polarimetric backscattering model for the shallow subarctic lakes. The model considers the three main scattering mechanisms as presented in Chapters 4, 5, and 6: subsurface scattering from the ice/water or ice/frozen soil interface modelled as an X-Bragg surface backscattering model discussed in Chapter 4; volume backscattering from the methane bubbles trapped within the ice modelled as cloud of partially vertically oriented ellipsoids as presented in Chapter 5; and dihedral scattering which is generated by scattering from the same volume of partially vertically oriented ellipsoids reflected by the subsurface whose mathematical form was derived in Chapter 6. They occur when ice is present on the lakes and they dominate the backscattering. The total backscattering is the incoherent sum of the backscattering from those mechanisms with a certain power weighting for each. The power dependency of the individual scattering mechanism on the physical and geometrical properties is already discussed in Chapters 4, 5, and 6. Combining the backscattering from these mechanisms considers these dependencies and is presented in the first part of this chapter.

The forward simulation of the model is performed for different scenarios, that are grounded/floating ice with high/low inhomogeneity densities within the ice. Then the simulation results are compared to fully polarimetric L-Band data that have already been presented in Chapter 3. From those results, an entropy-alpha colouring scheme is suggested and colour coded maps, that can distinguish between lakes with floating and grounded ice, are presented in the last part of this chapter.

7.1 Model equation

The coherency matrix of the model is obtained by adding the coherency matrices of the three main scattering mechanisms that are subsurface, volume and dihedral scattering, as shown in Fig. 1.1. As discussed in Chapter 6, the third scattering mechanism contributes with higher horizontal than vertical backscattering and a zero phase between them. ALOS data show an increase in the horizontally polarised backscattering compared to the vertically polarised during ice presence which has been noticed in Chapter 3, e.g. Fig. 3.10. Since this increase is not predicted by the subsurface nor the volume contribution, only the dihedral backscattering (volume-subsurface) can be used to predict it. Therefore the backscattering from this mechanism can not be neglected especially when the subsurface is water, which has a high reflectivity.

The backscattering from the surface (air-ice interface) is neglected, as its power is very low compared to the power backscattered from the ice-water interface and its polarimetric signature is very similar, such that its influence is further reduced, as shown Section 4.3.

The total backscattering coherency matrix for the model is

$$\begin{aligned}
 [T_{\text{total}}] = & P_{\text{SS}} \begin{bmatrix} T_{11}^{\text{SS}} & T_{12}^{\text{SS}} & 0 \\ T_{12}^{*\text{SS}} & T_{22}^{\text{SS}} & 0 \\ 0 & 0 & T_{33}^{\text{SS}} \end{bmatrix} + P_{\text{V}} \begin{bmatrix} T_{11}^{\text{V}} & T_{12}^{\text{V}} & 0 \\ T_{12}^{*\text{V}} & T_{22}^{\text{V}} & 0 \\ 0 & 0 & T_{33}^{\text{V}} \end{bmatrix} \\
 & + P_{\text{D}} \begin{bmatrix} T_{11}^{\text{D}} & T_{12}^{\text{D}} & 0 \\ T_{12}^{*\text{D}} & T_{22}^{\text{D}} & 0 \\ 0 & 0 & T_{33}^{\text{D}} \end{bmatrix} + [T_{\text{N}}],
 \end{aligned} \tag{7.1}$$

where each matrix above is normalized to the sum of its eigenvalues.

The first term in the equation corresponds to the backscattering from the subsurface. The subsurface is assumed to be an X-Bragg interface, since the X-Bragg model describes well the backscattering from the lakes during summer, as shown in Section 3.3.1, where only scattering from the air-water interface is expected. The power backscattered from the subsurface assuming an X-Bragg model is proportional to the factor P_{SS} and depends on the surface's geometrical and physical properties as clarified in Section 4.3. The power portion of the X-Bragg scattering is related to the permittivities of the layers through the scattering coefficients, shown in Eq. (2.24), as $P_{\text{SS}} \sim |R_{\text{h}}^2 + R_{\text{v}}^2|^2$. The polarimetric coherency matrix of the X-Bragg depends on the layers' permittivities and the distribution width of the subsurface slope angles which is related to the surface roughness. A preassumption of the permittivities is done according to Section 4.1.1. A fixed value for the distribution width of the slope angles

($\beta = 30^\circ$) is assumed for all cases, since it is the predicted value by the X-Bragg model for the backscattering acquired during summer.

The second term in the equation represents the coherency matrix of the volume backscattering. Rayleigh scattering is assumed. The power backscattered is proportional to the factor R_V which depends on volume density, layer thickness and the scattering from the single particles as shown in Eq. (5.12) and Eq. (5.3). The exact knowledge about the volume density and the particle dimensions is not available, nevertheless the volume backscattered power is expected to increase with increasing ice thickness. The volume is approximated by partially vertically oriented ellipsoids as mentioned in Section 1.1, and the power normalised coherency matrix of the volume backscattering depends on the particle shape and the orientation distribution. The forward simulations of the model consider the whole range of particle shapes (between sphere and dipole) and orientation (between oriented and random distribution). Preassumptions for the particle shape and distribution are not accurate without a priori knowledge as both may vary from site to site, the same holds for the particle density.

The third term in Eq. (7.1) corresponds to the coherency matrix of the dihedral backscattering from the volume reflected by the subsurface. The power backscattered from this component R_D depends on the specular reflection at the subsurface and the power scattered by the volume in the direction where the power is reflected back to the satellite by the subsurface. Hence this power backscattered by the dihedral component depends mainly on the volume backscattered power and the permittivities of the layers. The normalised coherency matrix in the forward simulation depends on the shape of the particles in the volume and the orientation distribution which are the same dependencies than those of the volume coherency matrix.

The last term in Eq. (7.1) is the additive noise consisting of a power coefficient multiplied by a unitary matrix.

7.2 Scenario Simulation

The model described in the previous section is used to simulate different lake conditions. The influence of the dihedral mechanism on the backscattering is better understood when it is observed in combination with the volume backscattering. In the following subsection, the scattering from volume and dihedral is discussed, and in the second subsection, simulations that consider the full combination of surface, volume and dihedral are performed.

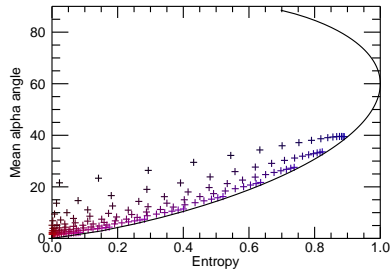
7.2.1 Combination of Volume and Dihedral Backscattering

The entropy-alpha distribution of the volume backscattering, dihedral backscattering and the combination of both is shown in Fig. 7.1. The volume backscattering in Fig. 7.1a differs from Fig. 5.9 by including the influence of the transmission through the air–ice interface. In general, the incident angle within the ice is smaller because of the transmission effects through the air–ice interface on the electromagnetic wave. Therefore the alpha values in Fig. 7.1a are smaller than in Fig. 5.9. The dihedral backscattering from the volume contribution reflected by the subsurface is shown in Fig. 7.1b, the left plot considers water subsurface and the right is for a frozen soil. The dihedral backscattering in those plots includes the transmission effects, which have not been included in Fig. 6.10. Similar to the volume, the transmission effects yield to lower alpha values. The permittivity of the subsurface slightly influences the dihedral polarimetric backscattering signature due to the relative changes in the Fresnel coefficients.

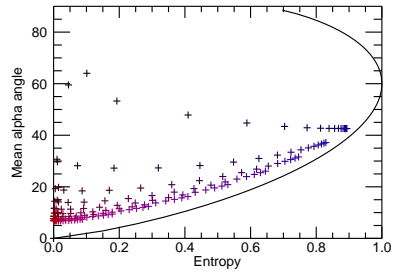
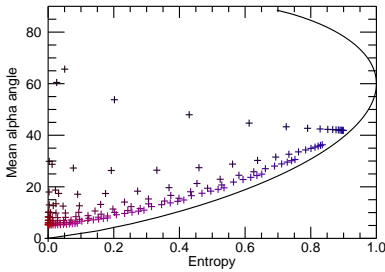
The combination of volume and dihedral backscattering has a higher entropy value compared to the volume backscattering, as shown in the two graphs in Fig. 7.1c, the left plot considers water subsurface and the right is for frozen soil. The combined backscattering of volume and dihedral is power weighted. The power backscattered from the dihedral is assumed to be equal to the power backscattered from the volume, since Rayleigh scattering with equal backscatter in the forward and backward direction is assumed and the look angles for the available ALOS data is rather small. Power attenuation through the 2 metres of fresh water ice layer is negligible at low frequencies (L-band) when the values in Section 4.1.1 are taken into account, and the power scattered from the volume that is related to the dihedral backscattering is mainly attenuated by the Fresnel reflection coefficients as described in Section 6.4. Power losses through reflection on the subsurface due to roughness are also neglected in the process of dihedral backscattering as the ice–water and ice–lake bed interfaces are expected to be smooth at L-band and the losses are small compared to the Fresnel coefficients. Accordingly the dihedral backscattered power is approximated to be proportional to the average Fresnel coefficient and the power backscattered by the volume as follows:

$$P_D \approx P_V \frac{(R_{\perp} + R_{\parallel})^2}{4}. \quad (7.2)$$

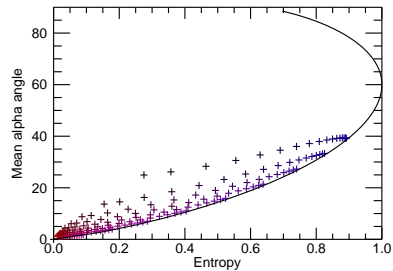
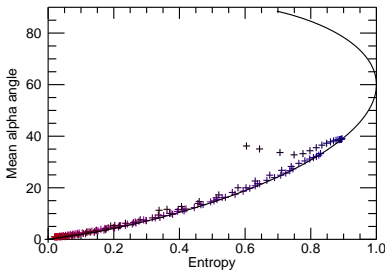
As can be seen in the equation above, the power contribution of the dihedral and volume backscattering is highly dependent on the permittivity of the subsurface. The high permittivity of the water yields to a higher dihedral backscattering contribution which brings an entropy-alpha distribution closer to the line of



(a) Volume backscattering



(b) Dihedral backscattering (left: water subsurface, right: soil subsurface)



(c) Volume + dihedral backscattering (left: water subsurface, right: soil subsurface)

Figure 7.1 Simulation of volume and dihedral backscattering at 25° local incident angle for the same points as in Fig 5.9 and Fig. 6.10.

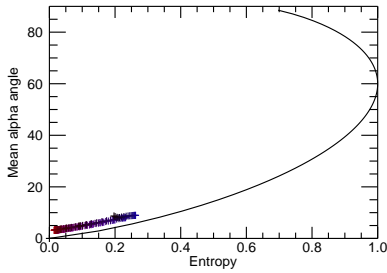
maximum entropy compared to a subsurface of frozen soil as can be observed in Fig. 7.1c.

The dihedral component has a higher absolute value for the coherency between the $S_{hh} - S_{vv}$ and $S_{vv} + S_{hh}$ channels than the volume backscattering. This coherency is proportional to the t_2 element of the normalised coherency matrix in Eq. (2.15). This coherency has a positive sign as $S_{hh} > S_{vv}$, unlike the coherency of the backscattering from partially vertical oriented prolates considered here, which has the property $S_{vv} > S_{hh}$. Because of this higher coherency with opposite sign, a small contribution from the dihedral backscattering effectively increases the entropy, as the coherency of the total volume and dihedral contribution is reduced, while the polarimetric ratio S_{hh}/S_{vv} and alpha angle are only slightly influenced, since the polarimetric ratios are more power dependent than the coherency. This can also be observed in the right graph of Fig. 7.1c when compared to Fig. 7.1a. The alpha value is slightly reduced since the co-polarisation ratio is closer to one and the influence of the coherency can be clearly observed with the high entropy values that are close to the line of maximum entropy.

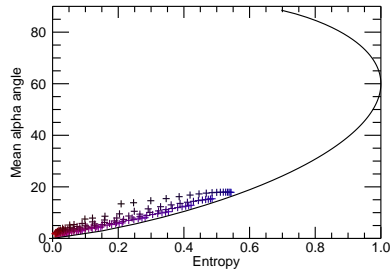
7.2.2 Subsurface, Volume and Dihedral Backscattering Combination

As has been discussed in Chapter 5, the volume backscattering depends mainly on the bubble size, bubble density and ice thickness, while the subsurface backscattering as presented in Chapter 4 depends mainly on the subsurface roughness and permittivity. Because of the wide variety of dependencies, no practical value based on theory for the subsurface to volume power ratio can be assumed, at least not based on the current knowledge about the methane bubbles and the subsurface properties. The lag of a priori knowledge about this ratio or about the bubbles' shape and orientation distribution leads to a non-unique mapping of entropy-alpha values, as for every subsurface to volume power ratio the same values of entropy and alpha are obtained for different realisation with respect to the shape of particles and their orientation distribution.

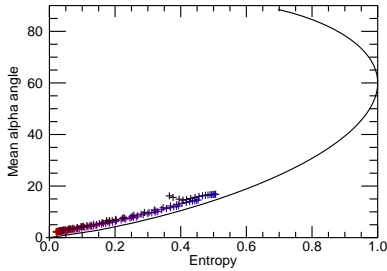
Figures 7.2a–7.2c show the entropy and alpha distributions for different volume power contributions (10 %, 25 % and 40 %). The distributions in Fig. 7.2a, 7.2b and 7.2c assume a water subsurface. The distribution in Fig. 7.2a has a 10 % volume backscattering, the dihedral backscattering contributes with 5 % calculated from Eq. (2.27) and Eq. (7.2), and the remaining 85 % is the power contribution of the subsurface backscattering. Therefore the distribution of the points are close to the surface scattering region, defined according to Fig. 2.3 . Figure 7.2d shows the same scenario as Fig. 7.2a, except the change in the subsurface permittivity where instead of water, soil is assumed. The power



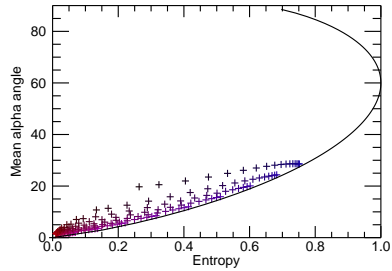
(a) 10% power backscattered by the volume with water subsurface.



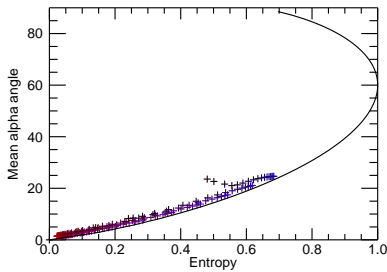
(d) The same simulation of (a) with soil subsurface



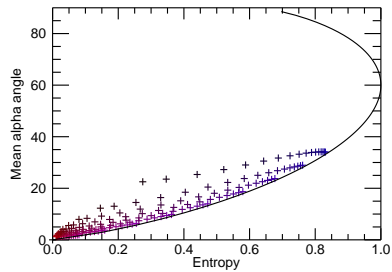
(b) 25% power backscattered by the volume with water subsurface.



(e) The same simulation of (b) with soil subsurface



(c) 40% power backscattered by the volume with water subsurface.



(f) The same simulation of (c) with soil subsurface

Figure 7.2 Simulation of subsurface, volume and dihedral backscattering at 25° local incident angle for the same set of points regarding shape and orientation of the particles, but different scenarios regarding lake conditions.

Water subsurface			
Volume power	10 %	25 %	40 %
Dihedral power	5 %	12 %	19 %
Subsurface power	85 %	63 %	41 %
Soil subsurface			
Ratio of total backscattered power for soil to water	0.26	0.38	0.51
Volume power	39 %	65 %	79 %
Dihedral power	3 %	6 %	7 %
Subsurface power	58 %	29 %	14 %

Table 7.1 Obtained power contributions of the different scattering mechanisms for different given volume power contribution in case of a water subsurface.

backscattered by the subsurface and the power backscattered by the dihedral are reduced for the lower subsurface permittivity. The change in the power backscattered by the subsurface due to the different permittivity is summarized in Eq. (4.4) and obtained for soil as shown in the following equation:

$$P_{SS,soil} = \frac{(R_{h,soil} + R_{v,soil})^2}{(R_{h,water} + R_{v,water})^2} \cdot P_{SS,water} \quad (7.3)$$

The dependency of the power backscattered by the dihedral on the physical properties is shown in Eq. (6.7) and the changes in the power backscattered by the dihedral for the water subsurface to the dihedral with a soil subsurface is according to

$$P_{D,soil} = \left(\frac{|R_{\perp,soil}| + |R_{\parallel,soil}|}{|R_{\perp,water}| + |R_{\parallel,water}|} \right)^2 \cdot P_{D,water} \quad (7.4)$$

From the two equations above, lower powers backscattered by the subsurface and the dihedral in Fig. 7.2d are obtained. Those lower values of the two backscattering mechanisms drive the volume backscattered power to be more dominant and correspond to a higher percentage of power despite that the absolute power backscattered by the volume does not change from Fig. 7.2a to Fig. 7.2d. Hence, the volume backscattering in Fig. 7.2d is around 39 %, the dihedral backscattering is only 3 %, and the subsurface backscattering is 58 %. The total absolute power in the case of Fig. 7.2d is scaled by a factor of 0.26 compared to the total power in the case of Fig. 7.2a.

The entropy-alpha distribution for the other cases (25 % and 40 % volume contribution) are also obtained with the same procedure presented above, and the obtained powers are shown in Tab. 7.1 .

All the simulations above show that the entropy and alpha values are higher when the volume is more dominant, therefore grounded ice has higher entropy and alpha values than floating ice for the same ice properties as the volume backscattering is more dominant over the subsurface and the dihedral. On the other hand, the influence of the dihedral backscattering is visible in the floating ice scenario as high entropy values are obtained for relatively low alpha, such that the entropy-alpha distribution is closer to the maximum entropy line.

7.3 Data Interpretation

The subarctic lakes are acquired in different conditions during the year, where for each condition different assumptions for the volume contribution and the subsurface permittivity are required to model them correctly. During summer and in the beginning of winter, a small volume contribution from a thin layer of floating ice is assumed. During winter, a higher volume contribution representing a thicker ice layer for both floating and grounded ice is assumed.

In this section, the forward simulations for the entropy and alpha values of different assumptions that match the expected site conditions are performed and compared with the observed entropy-alpha histograms. The test sites have been presented in Chapter 3. This comparison can better present the relation between the physical conditions of the lakes and the observed polarimetric information.

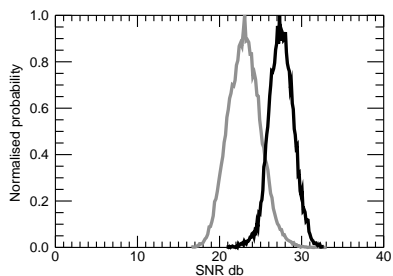
In the end of this section, a summary of expected properties of the backscattering for different lake conditions is shown in Tab. 7.4

7.3.1 Churchill site

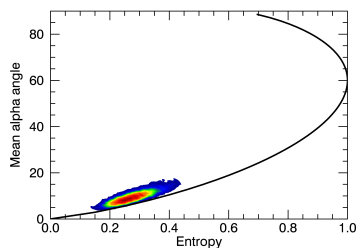
As mentioned in Chapter 3, the summer acquisition over Churchill site shows a response that matches the predictions of the X-Bragg surface model. Temperature measurements and ice thickness information close to the test site do not indicate considerable changes between the two winter acquisitions (23/04/2009 and 10/05/2009).

In general for each of the two acquisitions, the lake samples are divided into two groups, one with low backscattered power that is assumed to be grounded ice. The other group has high backscattered power and is assumed to be floating ice. The distribution of the lakes samples for May data is based on the separation performed for April data regarding grounded and floating ice, such that samples do not change groups and can be compared for temporal changes.

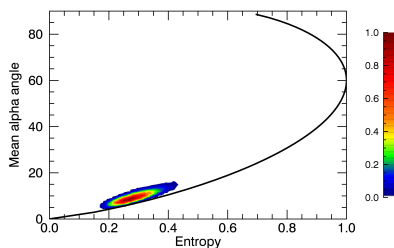
The grounded ice group from April data shows an average backscattered power that is around 0.35 of the average power of the floating ice samples. The entropy-alpha histogram for the data is shown in Fig 7.3b and 7.3c.



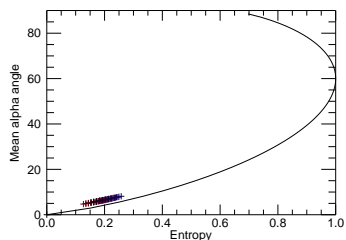
(a) Histogram of pixel intensities normalised to pixel noise intensity, grey: low backscattered power (grounded ice), black: high backscattered power (floating ice)



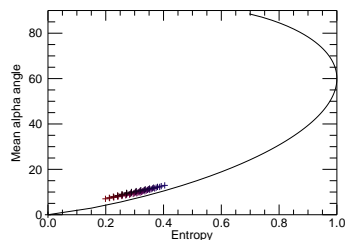
(b) Entropy-alpha histogram for floating ice (high power)



(c) Entropy-alpha histogram for grounded ice (low power)

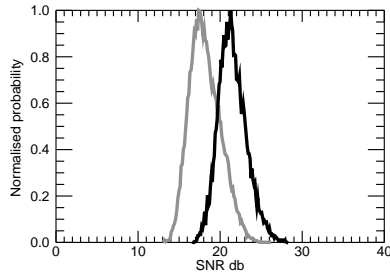


(d) Model simulation for 25% volume contribution, $A_p = 3.5 \dots 18$, and $\theta_{\text{orientation}} = 4^\circ \dots 54^\circ$ (water subsurface)

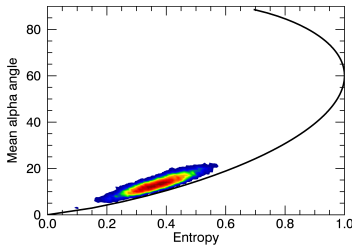


(e) The corresponding simulation to (d) (soil subsurface)

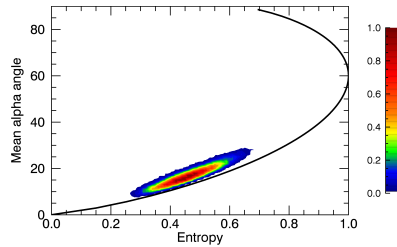
Figure 7.3 Data evaluation and corresponding simulation for Churchill site (23/04/2009).



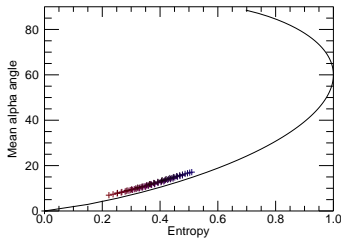
(a) Histogram of pixel intensities normalised to pixel noise intensity, grey: grounded ice categorised according to April observation, black: floating ice categorised according to April observation



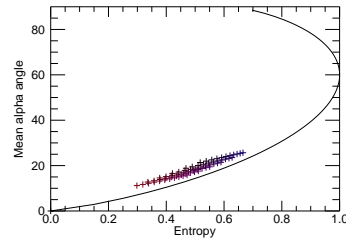
(b) Entropy-alpha histogram for floating ice



(c) Entropy-alpha histogram for grounded ice



(d) Model simulation for 35% volume contribution, $A_p = 4.5 \dots 18$, and $\theta_{\text{orientation}} = 4^\circ \dots 54^\circ$ (water subsurface)



(e) The corresponding simulation to (d) (soil subsurface)

Figure 7.4 Data evaluation and corresponding simulation for Churchill site (10/05/2009).

According to the analysis presented in Section 7.2, a volume power contribution of 25% for floating ice, results in a total backscattered power for grounded ice that has a factor of 0.38 of the power for floating ice. A certain range of volume orientation and particle shapes is simulated in Fig. 7.3d and 7.3e. The ranges of volume shape ($A_p = 3.5 \dots 18$) and orientation ($\theta_{\text{orientation}} = 4^\circ \dots 54^\circ$) are chosen to produce entropy and alpha values that cover the same range observed in the histogram of the floating ice. Figure 7.3d shows the distribution for the exact same parameters used to produce Fig. 7.3e but for a soil subsurface instead of water. The simulation does not highly differentiate between the floating and grounded ice as both simulation and data do not show high changes for different subsurfaces in this range of entropy-alpha.

The grounded ice group of the May data shows an average backscattered power that is 0.46 of the average power of the floating ice samples. The entropy-alpha histogram for the data is shown in Fig. 7.4b and 7.4c. Using the same analysis described above, a volume power contribution of 35% for floating ice results in a total backscattered power for grounded ice that has a factor of 0.46 of the power for floating ice. The ranges of volume shape ($A_p = 4.5 \dots 18$) and orientation ($\theta_{\text{orientation}} = 4^\circ \dots 54^\circ$) are chosen to produce entropy and alpha values that cover the same range observed in the histogram of the floating ice shown in Fig. 7.4b. Figure 7.4e shows the distribution for the exact parameters used to produce Fig. 7.4d but for a soil subsurface instead of water. Both simulation results and data show the same tendency, and vary similarly from floating ice to grounded ice.

7.3.2 Baker Lake site

The entropy-alpha histograms for the lake samples over Baker Lake site are shown in Fig. 7.5 for both acquisitions (March 15, 2007 and April 30, 2007). Ice thickness measurements over the Baker Lake show an increase of around 50 cm from March to April, see Fig. 3.4. The temperature measurements increased after March but it is still below zero in the end of April.

To investigate the change in the entropy-alpha histogram, an initial volume contribution for floating ice during March is chosen (Scenario 1 and Scenario 2 in Tab. 7.2). From the initial set up of the two scenarios, two assumptions for each scenario are investigated for April. The first one assumes an increase of 5% in the volume contribution and the second one is that the subsurface changes from water to frozen soil.

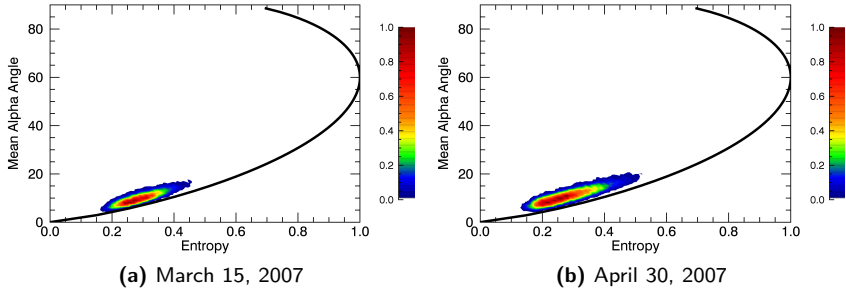


Figure 7.5 Entropy-alpha histogram obtained from ALOS data over Baker Lake site.

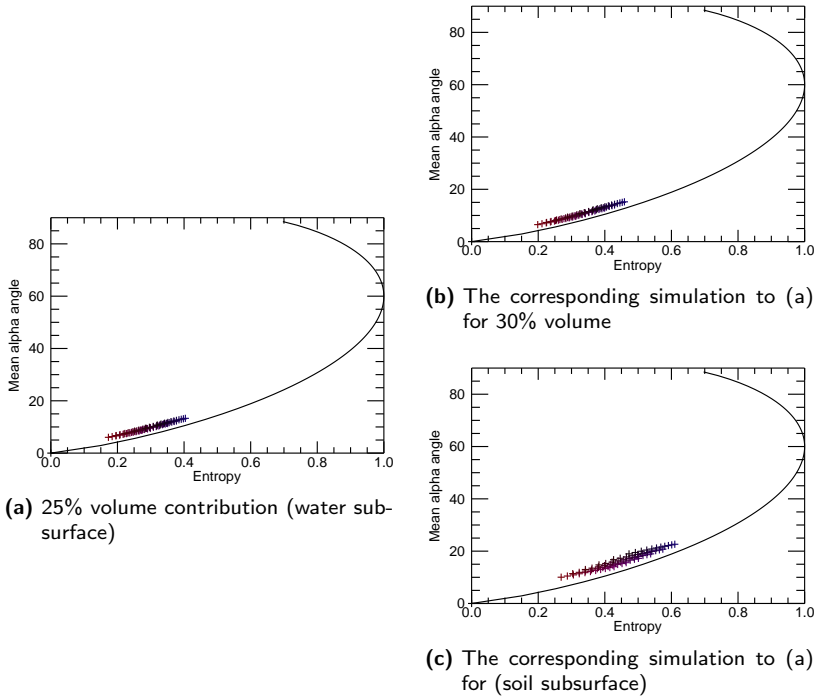
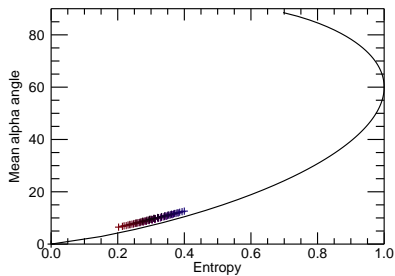
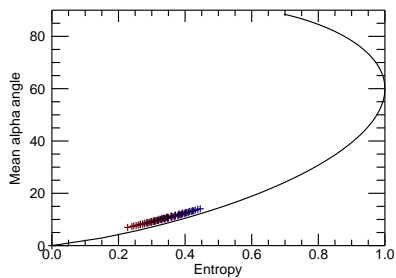


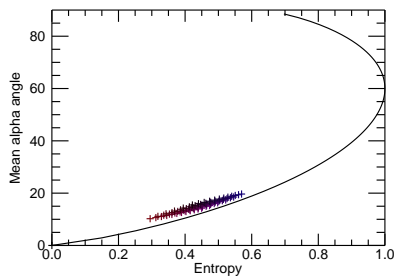
Figure 7.6 Simulated entropy-alpha point distributions for Baker Lake considering the parameters of scenario 1 in Tab. 7.2.



(a) 30% volume contribution (water subsurface)

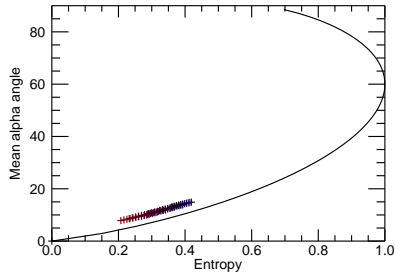


(b) The corresponding simulation to (a) for 35% volume

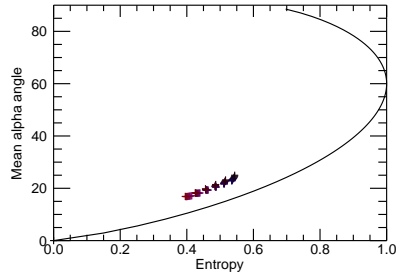


(c) The corresponding simulation to (a) for (soil subsurface)

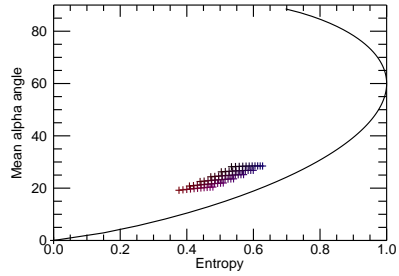
Figure 7.7 Simulated entropy-alpha point distributions for Baker Lake considering the parameters of scenario 2 in Tab. 7.2.



(a) 25% volume contribution (water subsurface)



(b) The corresponding simulation to (a) for 30% volume



(c) The corresponding simulation to (a) for (soil subsurface)

Figure 7.8 Simulated entropy-alpha point distributions for Baker Lake considering the parameters of scenario 1 in Tab. 7.2, but for a larger local incident angle $\theta_L = 30^\circ$ instead of 25° . A clearer separation is expected for larger local incident angles.

Water subsurface	Scenario 1	Scenario 2
Volume power	25 %	30 %
Dihedral power	12 %	14.5 %
Subsurface power	63 %	55.5 %
$\theta_{\text{orientation}}$	4° – 52°	4° – 60°
A_p	4.5 - 18	4.2 - 18.2
Water subsurface + 5 % volume power		
Volume power	30 %	35 %
Dihedral power	14.5 %	17 %
Subsurface power	55.5 %	48 %
Soil subsurface		
Ratio of total backscattered power for soil to water	0.38	0.42
Volume power	65 %	71 %
Dihedral power	6 %	6 %
Subsurface power	28 %	23 %

Table 7.2 Parametres and power contributions of the two different simulated scenarios considered for Baker site.

Volume contributions of 25 % (Fig. 7.6a) and 30 % (Fig. 7.7a) are assumed and compared with the March acquisition, shown in Fig. 7.5a. With increasing the volume contribution by 5 % for the same volume shape and orientation, an entropy-alpha point distribution is obtained and shown in Fig. 7.6b and 7.7b that covers the same region as the data in April. By running the same simulation of March but with soil subsurface, the entropy-alpha distributions in Fig. 7.6c and 7.7c are obtained, where the values are larger than what is obtained from ALOS data during April. Nevertheless the grounded ice region highly overlaps with the region of ALOS data such that April data can also be covered by a mixture of grounded and floating ice. The values of volume, dihedral and surface contribution in addition to the assumed ranges of volume shapes and orientations are listed in Tab. 7.2.

When the entropy-alpha values are low then the point distributions for varying parameters are more confined and closer to the maximum entropy line. In this region the values for floating and grounded ice highly overlap. For larger local incident angle, the effects of more volume can be better distinguished from grounded ice as shown in Fig. 7.8, where the same simulation as in Fig. 7.6 is performed but with a local incident angle of 30°.

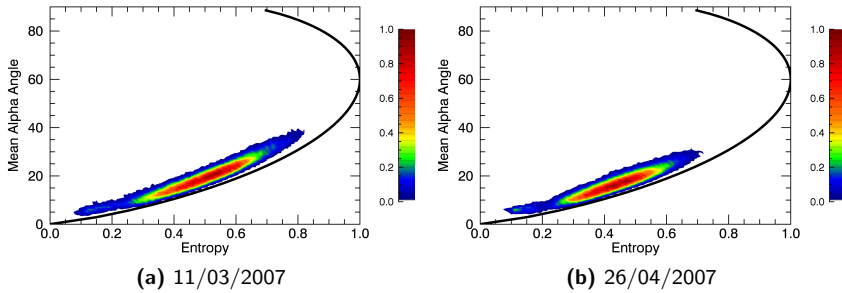


Figure 7.9 Entropy-alpha histogram obtained from ALOS data over Inuvik site.

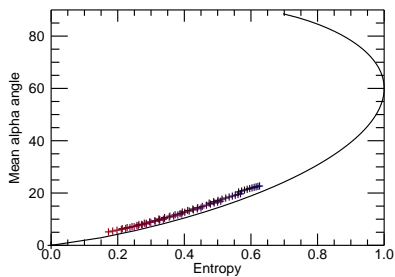
7.3.3 Inuvik site

For the Inuvik site two acquisitions one in March and one at the end of April are available. Temperature measurements in the area for the days before the second acquisition were above zero indicating a possible melting process, see Fig. 3.7. Unfortunately, ice thickness measurements are not available for the year of the acquisition but similar melting processes are observed in the ice thickness measurement in the years before the acquisition, occurring at the beginning of May.

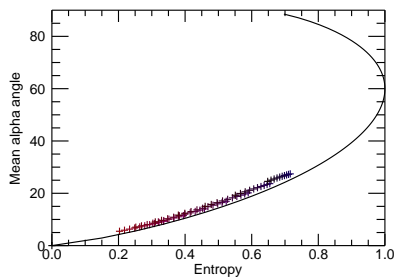
For the SAR data, higher entropy and alpha values with a distribution that is further away from the maximum entropy line is observed for the first acquisition compared to the second (Fig. 7.9a and 7.9b). This indicates a change from grounded ice in the first acquisition to floating ice in the second.

Similar investigations for floating and grounded ice that were referenced on Churchill and Baker lake region are performed for Inuvik data with an assumption of 40% and 25% volume contribution during ice presence and shown in Fig. 7.10 and Fig. 7.11 respectively. The sets of parameters used for those two scenarios are summarised in Tab. 7.3. Considering a different volume contribution results in a different range of particles' shape and orientation to cover the same region of entropy-alpha values, but shows similar trend between grounded and floating ice.

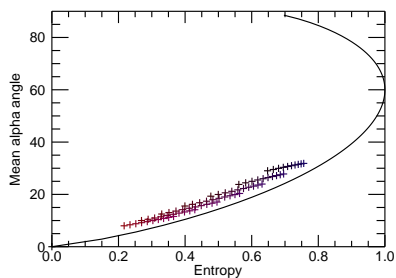
The simulation of 10% higher volume contribution shown in Fig. 7.10b and 7.11b, do not show a similar correspondence to the data obtained during March since the entropy-alpha histogram observed by the data is not very close to the maximum entropy line as well as for the simulation.



(a) 40% volume contribution (water subsurface) compared to April data

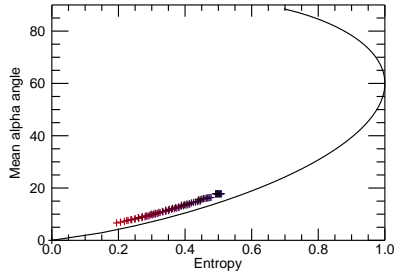


(b) The corresponding simulation to (a) for 50% volume compared to March data

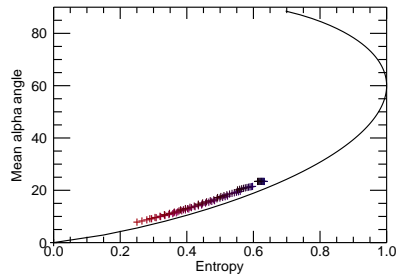


(c) The corresponding simulation to (a) for (soil subsurface) compared to March data

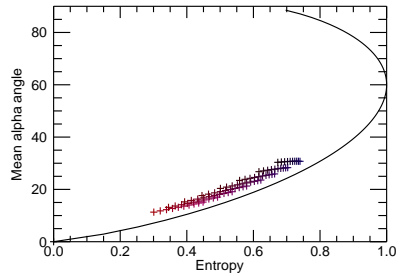
Figure 7.10 Simulated entropy-alpha point distributions for Inuvik considering the parameters of scenario 1 in Tab. 7.3.



(a) 25% volume contribution (water subsurface) compared to April data



(b) The corresponding simulation to (a) for 35% volume compared to March data



(c) The corresponding simulation to (a) for (soil subsurface) compared to March data

Figure 7.11 Simulated entropy-alpha point distributions for Inuvik considering the parameters of scenario 2 in Tab. 7.3.

Water subsurface	Scenario 1	Scenario 2
Volume power	40 %	25 %
Dihedral power	19 %	12 %
Subsurface power	41 %	63 %
$\theta_{\text{orientation}}$	4° – 50°	4° – 50°
A_p	3.5 - 18	5.3 - 18.3
Water subsurface + 5 % volume power		
Volume power	50 %	35 %
Dihedral power	24 %	17 %
Subsurface power	26 %	48 %
Soil subsurface		
Ratio of total backscattered power for soil to water	0.51	0.38
Volume power	79 %	65 %
Dihedral power	7 %	6 %
Subsurface power	14 %	29 %

Table 7.3 Parametres and power contributions of the two different simulated scenarios considered for Inuvik site.

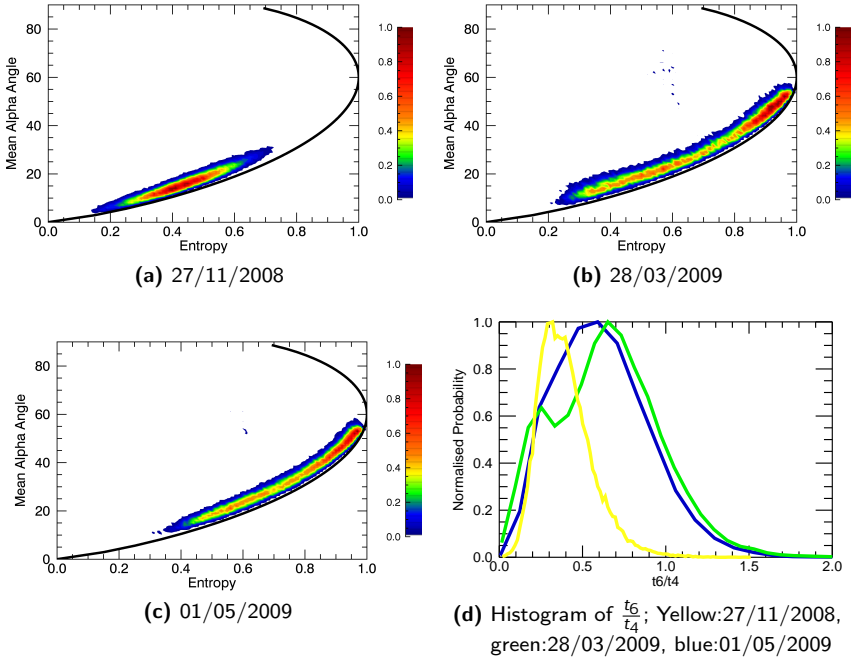


Figure 7.12 Histograms obtained from ALOS data over Lena Delta site, a,b, and c are entropy-alpha histograms, d is the histogram of t_6/t_4 .

7.3.4 Lena Delta site

While for all other test sites and all acquisition times a strong correlation between model prediction and experimental data is given, the winter data over the Lena Delta site are an exception with entropy-alpha values that exceed the model limits, as shown in Fig. 7.12b, 7.12c. This can also be observed in the low coherency between the co-polarisation channels in Fig. 3.16b and the low value of the polarimetric anisotropy in Fig 3.16d. Later winter data over Lena site show also a lower horizontal to vertical backscattering ratio than the data obtained during early winter, as can be observed in Fig. 3.16c.

The data show also a high backscattering in the cross-polarization channel, such that a high value for the t_6 element of the coherency matrix, shown in Eq. (2.15), is observed. The histogram of the measured t_6 to t_4 ratio is shown in Fig. 7.12d. It contains values that exceed 1 during late winter acquisitions. A low coherency between the co-polarisation and cross-polarisation channels

is also measured indicating a symmetry around the line of sight, as discussed in Section 2.4. A value of t_6 to t_4 ratio that is larger than one could not be predicted by any model that assumes symmetry around the line of sight [58], even when a volume of large dipoles is considered.

On-site measurements of the physical properties of the ice and lakebed and maybe a more sophisticated model might be required to explain the measured backscattering.

	Dominating scattering mechanism	Relative scattered power	Co-polarisation power ratio S_{HH}/S_{VV}	Entropy H	Alpha α	Position in the entropy-alpha plane	Anisotropy A
Water surface / Water + thin layer of ice	Surface	Low	Low (< 0.9)	Very low (< 0.2)	$\approx 10^\circ$	Between close to far from the boundary line	≈ 0.8
Thin layer of grounded ice	Surface + volume	Low / medium (depending on subsurface roughness)	Low (≤ 0.9)	Low ($0.2 < H < 0.5$)	$\leq 10^\circ$	Close to the boundary line (with a trend of being further away when volume contribution increases)	≈ 0.5
Medium thickness layer of floating ice	Surface + volume + dihedral	High	High (≈ 1.1)	Low ($0.2 < H < 0.5$)	$\approx 10^\circ$	Close to the boundary line (and approach it when volume contribution increases)	≈ 0.5
Medium thickness layer of grounded ice	Surface + volume	Low (for smooth subsurface)	Low (≈ 0.9)	High ($0.5 < H < 0.9$)	$\approx 25^\circ$	Far from the boundary line	≈ 0.5
Thick layer of floating ice	Surface + volume + dihedral	High	High (≈ 1.2)	High ($0.5 < H < 0.9$)	$\approx 20^\circ$	Very close to the boundary line	≈ 0.5

Table 7.4 Expected properties of the backscattering for different lake conditions.

Water subsurface	
Volume power	0.1 %–60 %
Dihedral power	0 %–29 %
Subsurface power	99.9 %–11 %
$\theta_{\text{orientation}}$	45° – 30°
A_p	18
Soil subsurface	
Ratio of total backscattered power for soil to water	0.18–0.67
Volume power	0.6 %–89 %
Dihedral power	0 %–8 %
Subsurface power	99.4 %–3 %

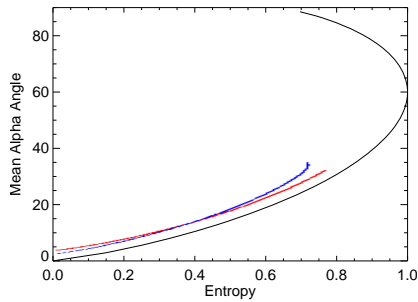
Table 7.5 Parameters for the power contributions considered for the simulation of the two (floating/grounded lake ice) entropy-alpha lines, shown in Fig. 7.13a.

7.4 Data Representation

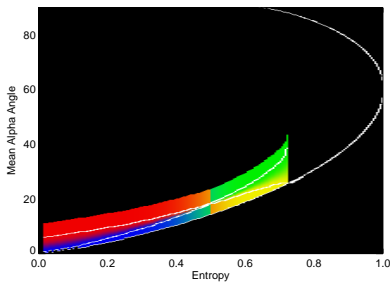
As can be concluded from the previous section, the entropy-alpha values depend on the scattering processes occurring. For a certain range of particle shapes and orientations within the ice volume of the frozen subarctic lakes, a clear difference between floating and grounded ice can be observed in measurements and simulations of the power independent entropy-alpha plane. Therefore an entropy-alpha colour scheme based on those simulations is suggested and colour coded maps of the considered ALOS acquisitions are presented and discussed in this section.

The colour scheme is generated by considering two entropy-alpha lines. One corresponds to floating ice and the other to grounded ice. The value for the particle anisotropy (A_p) of the inhomogeneities within the ice layer is assumed to be 18, a value well within the range covered by all scenarios considered in the previous section. Note that no remarkable difference is observed compared to a particle anisotropy of 8. The orientation distribution is assumed to decrease from 45° for a thin ice layer to 30° for a thick ice layer, by assuming that a thin ice layer has more randomness in the orientation of the inhomogeneities, while they are more oriented in thick ice. This combination of particle anisotropy and orientation distribution corresponds to entropy and alpha values for different volume contributions that are close to the maximum entropy line and observed by most of the data acquired during ice presence.

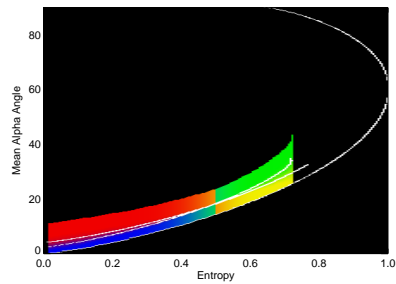
Figure 7.13a shows the two simulated entropy-alpha lines, where the blue line corresponds to grounded ice and the red line corresponds to floating ice



(a) Simulated entropy-alpha lines, red for floating ice and blue for grounded ice



(b) The two lines that are used to generate the colour scheme



(c) The simulated lines of Fig. 7.13a with the colour scheme

Figure 7.13 Construction of a colour scheme based on the simulation of subsurface, volume and dihedral backscattering at 25° local incident angle for the same set of points regarding shape and orientation of the particles, but different scenarios regarding lake conditions. Blue: thin layer of grounded ice. Green: medium thickness layer of grounded ice. Red: medium thickness layer of floating ice. Yellow: thick layer of floating ice.

with a larger dihedral backscattering. Each line is generated by considering the volume shape and orientation described above, the corresponding subsurface permittivity and different contributions of the volume backscattered power starting from 0.1% up to 60% of the total backscattered power for floating ice. The detailed simulated parameters and power contributions are listed in Tab. 7.5.

Two new lines are generated from the simulated lines by doubling the distance between the simulated lines as shown in Fig. 7.13b. The new lines are used to calculate the colour scheme shown in Fig. 7.13c, such that the colours

gradually change from one line to the other. This colour scheme assigns a blue colour to a thin layer of grounded ice as for the case of bare soil lands that are covered by a thin layer of ice during winter. The red colour is assigned to a medium thickness layer of floating ice, while the green colour corresponds to a medium thickness layer of grounded ice (grounded lakes). The yellow colour corresponds to a thick layer of floating ice, it has to be noted that this case might not be accurately modelled, as propagation effects which are not considered here might influence the backscattering significantly.

This model with fixed volume shape and orientation distribution is a simplified approach for representing the complex nature of subarctic lakes, but nevertheless it can explain the trends observed in ALOS acquisitions, as can be seen in the following subsections.

7.4.1 Churchill site

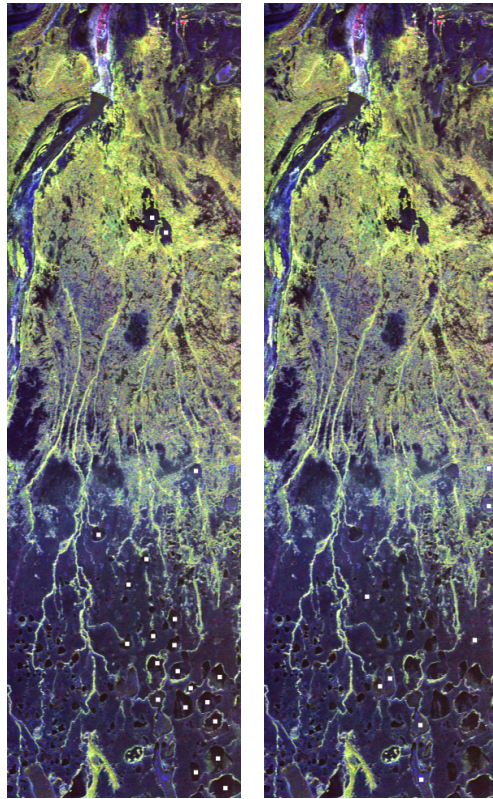
The power histogram observed over Churchill site in Fig. 3.10a shows a wide range of powers over the lakes (around 10 dB range) with two peaks which made the site a good candidate for dividing the lake samples into two groups, as shown in Section 7.3.1. One group has low backscattered power and it is assumed to correspond to grounded ice. The other group has high backscattered power and is assumed to be floating ice. The entropy-alpha histogram observed during the winter acquisition (10/05/2009) is in a good agreement with the simulation. Therefore a close look at the maps of this acquisition is presented here.

The power map of the winter acquisition (10/05/2009) over Churchill site is shown in Fig. 7.15a and according to this power map the lake samples are assigned to be either grounded, shown in Fig. 7.14a, or floating ice, shown in Fig. 7.14b. For each pixel in the maps, entropy, alpha and anisotropy values can be calculated, as shown in Fig. 7.16a, 7.16b, and 7.16c. To implement the colour scheme in Fig. 7.15b, the colour of each pixel is assigned according to the entropy and alpha values observed at that pixel after looking up the values in the colour scheme. The map of Churchill acquisition (10/05/2009) in Fig. 7.15b is generated in this way. In general, bare soil in the entropy-alpha colour coded maps appears blue during winter, since it is covered by a thin layer of ice and acts similar to a thin layer of grounded ice. Lakes with floating ice appear red in addition to parts of the Churchill river as water under a meter thick layer of ice contributes with more dihedral backscattering than grounded ice. Some lakes that have not been considered in the preselected samples also appear red in the power normalised entropy-alpha map, and they correspond to high power when they are compared to the power map indicating that they are floating ice. The lake indicated in Fig. 7.15a with a red circle is assigned according to the observed power to be grounded ice but appears to be floating

ice in the entropy-alpha map. Without on-site measurements it is difficult to conclude about the right interpretation. Lakes with grounded ice appear green as the backscattering is mostly dominated by the volume backscattering. The entropy-alpha values for grounded lakes are ambiguous with the values for the trees as they also appear green in the entropy-alpha map but the scattering mechanisms occurring at trees are different, which can be observed in the anisotropy map in Fig. 7.16c, as the lakes and the ground have in general higher anisotropy than the trees.

The maps of entropy or alpha alone cannot describe the difference between the two classes of lakes, but the combined information in the entropy and alpha values can better interpret the observed scatterer.

The entropy-alpha colour coded maps for Churchill site for both winter acquisitions (23/04/2009, and 10/05/2009) are shown in Fig. 7.17a, and 7.17b, in order to evaluate the temporal changes. For the first winter acquisition some lakes appear as grounded ice with few inhomogeneities within the ice layer (a thin layer of ice or few bubbles within the ice). Therefore they are indicated by blue colour while other lakes show a rather red colour indicating floating ice condition. The difference between grounded and floating ice is clearer in the second acquisition as more inhomogeneities are observed within the lake ice, such that lakes with grounded ice appear green since the backscattering is dominated by the volume contribution and lakes with floating ice appear more red compared to the first acquisition as the dihedral backscattering increases. Hence a clearer difference in the contribution of the dihedral backscattering between grounded and floating ice is observed in the second available acquisition.



(a) Samples of lakes with grounded ice

(b) Samples of lakes with floating ice

Figure 7.14 SAR image from May 10, 2009 (Pauli image) over Churchill site with white squares that represent the lake samples.

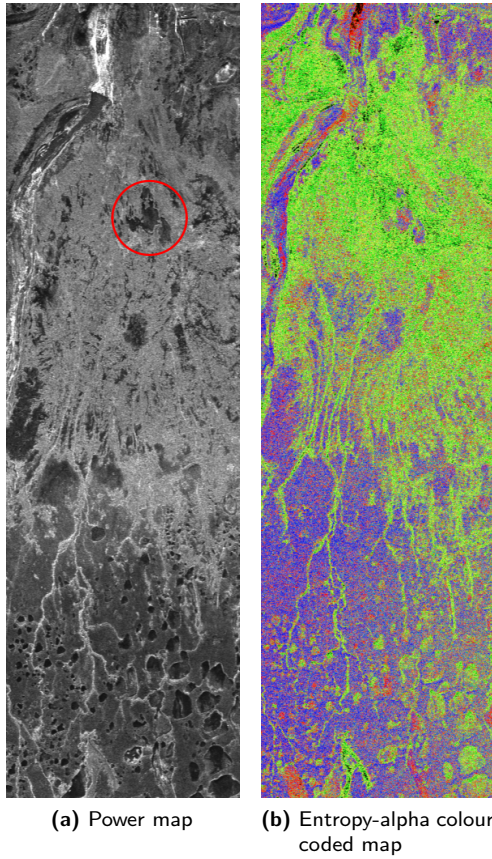


Figure 7.15 SAR image from May 10, 2009, Churchill site. The colour coded map is generated from the colour scheme shown in Fig. 7.13c.

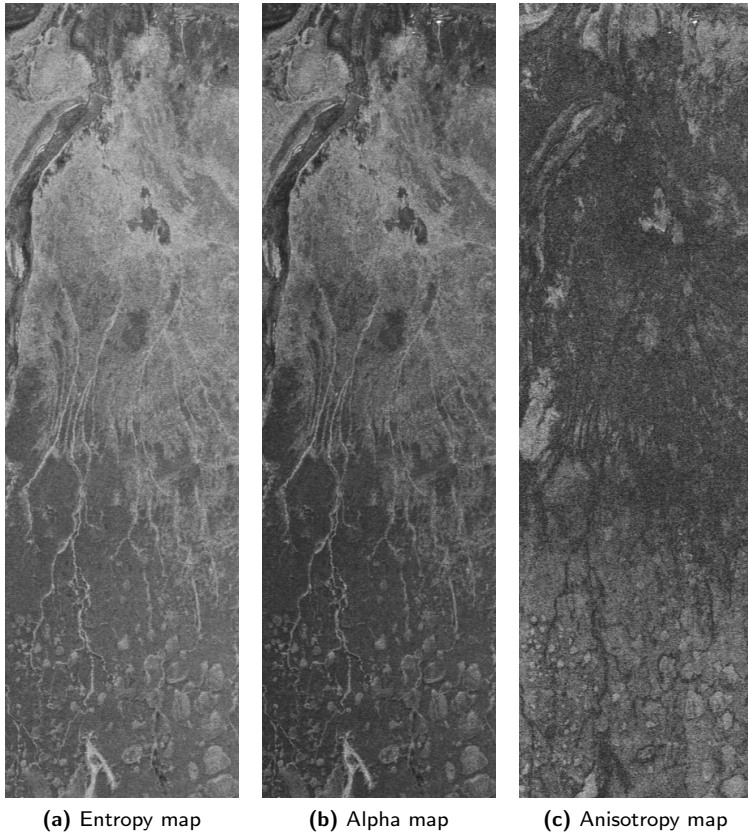


Figure 7.16 SAR image from May 10, 2009, Churchill site.

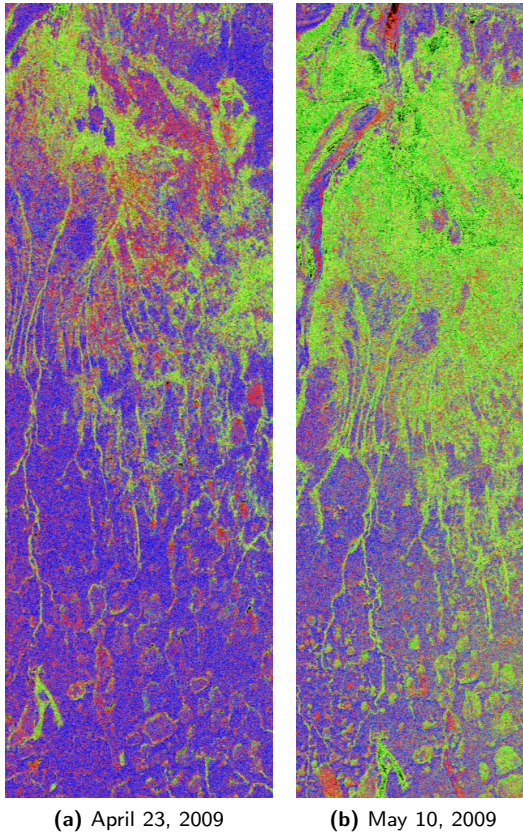


Figure 7.17 Entropy-alpha colour coded maps of Churchill site. The maps are generated from the colour scheme shown in Fig. 7.13c.

7.4.2 Baker Lake site

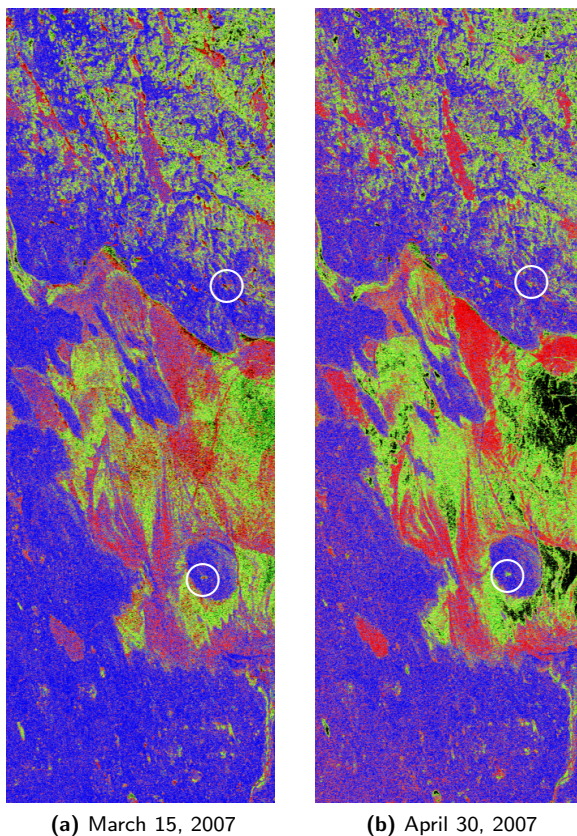


Figure 7.18 Entropy-alpha colour coded maps of Baker Lake site. The maps are generated from the colour scheme shown in Fig. 7.13c.

The entropy-alpha colour coded maps over Baker Lake site for the winter acquisitions (15/03/2007, 30/04/2007) are shown in Fig. 7.18. The image of the second acquisition shows a more intensive red and green colour, which indicates a clear increase in the inhomogeneities within the ice layer as the lakes show either a larger backscattering from the volume or backscattering from the dihedral of volume and water subsurface. This increase in the inhomogeneities can be due to the increase in the ice thickness in the time between the first and second acquisition, as has been discussed in Section 7.3.2. The lakes

marked with white circles have floating ice in the first acquisition which became grounded ice in the second acquisition.

The second acquisition shows black areas in a part of the Baker Lake, which indicates the presence of scattering mechanisms that correspond to entropy-alpha values that are not covered by the colour scheme proposed in Fig. 7.13. This can be due to cracks within the ice layer that can appear in big lakes.

7.4.3 Inuvik site

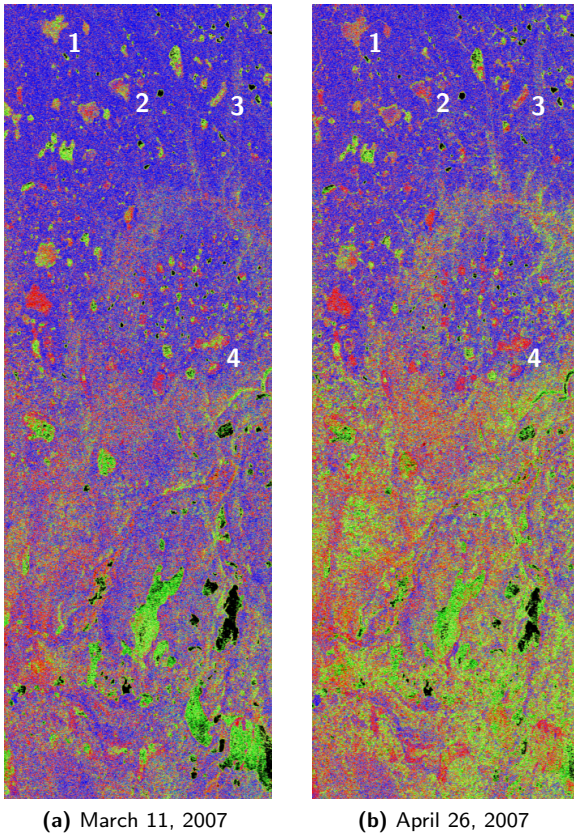


Figure 7.19 Entropy-alpha colour coded maps of Inuvik site. The maps are generated from the colour scheme shown in Fig. 7.13c.

The entropy-alpha colour coded maps over Inuvik site for the two acquisitions in March and end of April are shown in Fig. 7.19. Possible melting occurrence before the second acquisition is discussed in Section 7.3.3. The melting is also observed in the entropy-alpha colour coded maps, as several lakes changed their colour from green indicating grounded ice to red indicating floating ice condition. Some of those lakes are indicated by the numbers 1 to 4 in Fig. 7.19. The red lakes during the first acquisition stay red during the second acquisition as floating ice stays floating. Some relatively large lakes show a black colour and are not covered by the scattering model proposed.

7.4.4 Lena Delta site

The entropy-alpha colour coded maps from data acquired over Lena Delta are shown in Fig. 7.20. The early winter acquisition (27/11/2008) shows that most of the lakes on the northern part of Lena Delta and close to the Laptiv sea are already frozen to the lakebed, while the lakes that are further to the south still covered by floating ice since they appear red in the map.

Late winter data (28/03/2009 and 01/05/2009) show several lakes that are black as they are not covered by the model. Most of the lakes in the first late winter acquisition (28/03/2009) are red but this does not indicate an increase in the dihedral backscattering, because the ratio of the horizontal to vertical co-polarisation channels is less than the ratio measured in the other two acquisitions of Lena Delta as shown in Fig. 3.16c. Interpretation of the backscattering from Lena Delta site during late winter is not feasible without the on-site ground measurements, that lead to an extended model for the lakes.

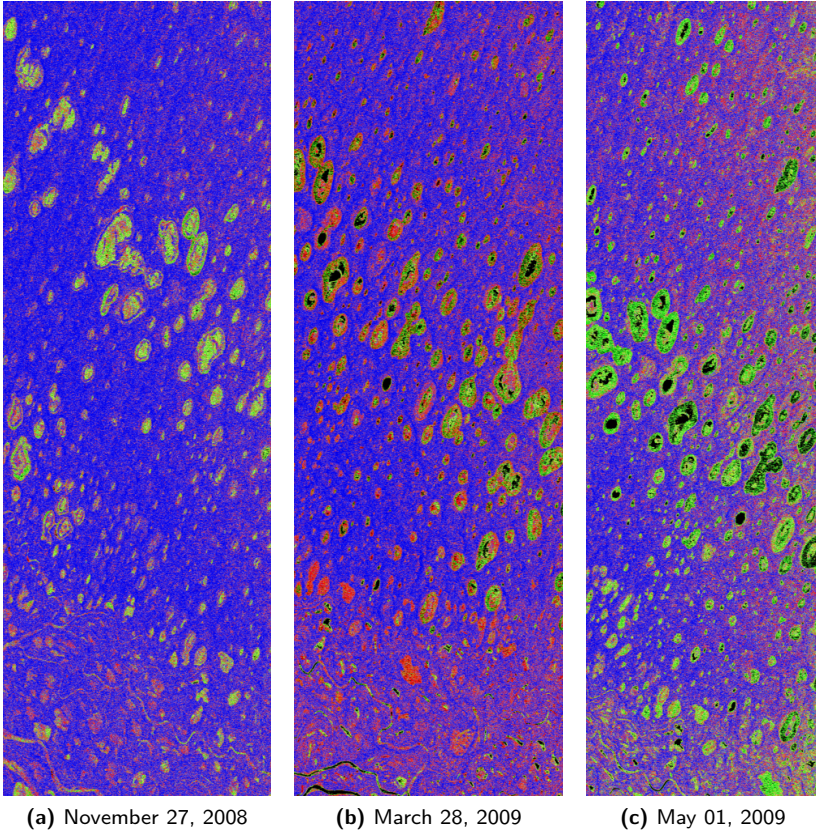


Figure 7.20 Entropy-alpha colour coded maps of Lena Delta site. The maps are generated from the colour scheme shown in Fig. 7.13c.

Chapter 8

Conclusion

With the purpose of investigating the potential of long wavelength side-looking SAR in revealing facts about the subsurface within several metres depth, a model for the polarimetric backscattering was developed and compared to fully polarimetric L-band data acquired by ALOS-PALSAR over frozen subarctic lakes. Most of the data were acquired during ice presence where the lakes' water freezes up to one or two metres.

The data show a noticeable decorrelation between the co-polarisation backscattering, which indicates a strong contribution of the scattering from the inhomogeneities within the ice in addition to the backscattering from the ice-water subsurface. Literature reports several sources of inhomogeneities, such as crystals and bubbles, but one type of inhomogeneities which is the largest in size are the methane bubbles. For modelling it, observations of methane bubbles in lakes, were considered. They clarify that the ice is formed layer by layer and the bubbles get trapped in the newly formed layer of ice, generating the column shape structure. The volume backscattering from those structures was modelled as the Rayleigh backscattering from partially vertically oriented ellipsoids.

ALOS data show an increase in the horizontally polarised backscattering correlated with the ice presence. This increase cannot be explained with the volume backscattering since the partially vertically oriented volume contributes with a higher vertically than horizontally polarised backscattering. The most well-known scattering mechanism that corresponds to a higher horizontally than vertically polarised backscattering is the dihedral backscattering, but it predicts a co-polarisation phase shift of π which is not observed in the data. Therefore

the dihedral backscattering from the volume reflected by the subsurface was evaluated.

The mathematical formulation for the backscattering from this mechanism has been developed within the frame of the thesis, since there had not been any closed form that can directly evaluate this scattering. First, the scattering for a single ellipsoid particle has been derived in the form of a scattering matrix, which is used to describe its interaction with the subsurface. Then for the correct polarimetric signature it is essential to consider the two possible paths for the particle subsurface interaction. Finally, the contribution of the dihedral mechanism is obtained by statistically averaging over all possible particles in the volume. The resulting polarimetric backscattering was described in a coherency matrix. This scattering mechanism predicts a larger horizontally polarised backscattering than vertically polarised, a zero co-polarisation phase shift for small local incident angles and a phase shift of π for large incident angles. This mechanism could describe a great part of the backscattering from the subarctic lakes.

The final model for the subarctic lakes considered the three main backscattered contributions: subsurface backscattering modelled as X-Bragg subsurface, volume backscattering, and the dihedral backscattering of a volume above a subsurface. The power contribution from the dihedral mechanism was assumed to be equal to the power contribution of the volume attenuated by the reflection coefficient on the subsurface. This assumption holds only for negligible propagation losses within the volume layer and a smooth subsurface, which is expected for the case of subarctic lakes (1 to 2 meters of ice) using L-band. In this way, the dihedral backscattering depends on the volume characteristics and the subsurface permittivity, such that the model has the same number of unknowns as a model that considers the contributions of the subsurface and volume only. The model is more complex but it can explain far better the backscattering dependency on the subsurface material (water/soil) and the observed high value of the polarimetric entropy than other models with only subsurface and volume.

The model predicts a higher backscattered power from the floating ice than from the grounded ice, because of the higher contribution from the subsurface and the dihedral backscattering. Because of the higher backscattered power from the dihedral mechanism, a higher horizontal to vertical backscattering ratio is expected for floating ice. The model also predicts a higher entropy value when the ice is grounded than when the ice is floating for an ice layer of medium thickness, since the volume contribution is more dominant over the subsurface and dihedral contribution for the first case. According to the model, the entropy-alpha combination for grounded ice is further away from

the entropy-alpha boundary line than the combination for floating ice in the case of medium thickness.

Simulations based on the model were compared with ALOS data. Over Churchill site the lake samples were divided into two groups, one with high backscattered power that was assumed to be floating ice and one with low backscattered power that was assumed to be grounded ice. The forward simulation with a water subsurface and a certain range of volume characteristics matched the observed polarimetric parameters for floating ice lake samples observed by ALOS. The exact same simulation with the identical assumptions was performed for grounded ice and it matched the observed polarimetric parameters for grounded ice lake samples observed by ALOS. Hence the model shows the same trend as the observed data for grounded and floating ice. Over Inuvik site a similar investigation was performed while assuming the first acquisition to be grounded ice and the second to be floating ice, as ice melting before the second acquisition was verified by temperature measurements. The model could explain this temporal change as well.

Sites with very high methane emission form large bubbles (larger than 5 cm) or even some holes in the ice (hot spots). The examples of such subarctic lakes are the lakes over Lena Delta site. The polarimetric parameters for those lakes during later winter exceed the limits predicted by the model, since the assumption of Rayleigh size inhomogeneities seems not appropriate anymore. On-site measurements of the physical properties of the ice and lakebed in Lena Delta site and further investigations are required for further considerations in modelling the lakes in Lena Delta.

In general, for all the sites except late winter acquisitions over Lena Delta, the model predicts the same polarimetric backscattering as the observed ALOS data. The model could also explain the difference in the backscattering for different states of the lake ice (grounded/floating) and some temporal changes. The data have also been represented with power independent colour coded maps, where the temporal changes were also observed. The colour scheme was generated by applying the model, while considering a specific particle shape and orientation within the volume.

The applicability of the novel model is not limited to the exclusive scenario of frozen subarctic lakes. Several other scenarios in remote sensing of natural sites can be approached with the established scattering model, as the basic structure of having a surface covered by a volume exists in several different natural scenarios. An example of such a structure is the vegetation cover observed at low frequencies, such as P-band. Propagation effects and/or scattering by a volume of large particles might need to be considered at higher frequencies and an extended version of this model then might be able to explain the backscattering also at higher frequencies. Another example of a structure of a volume

above a surface is snow cover [89], [85] observed at C-band. A slightly different model based on the presented one, that considers propagation effects [14] and/or scattering by a volume of large particles might be able to explain the backscattering from the snow cover, since a co-polarisation phase shift of around 10° at typically 30° incident angle is measured as shown in [38]. Rock bed covered by sand dunes is another example of a two-layer structure [33], [56], [75], [55], [76], that is spread on Earth, where the model might be able to explain the backscattering from it. As most of the nearby planetary objects beside Earth, for example Moon or Mars, have a dry surface, several meters of penetration within their upper layer (regolith) is expected at frequencies such as L-band and P-band [30], [77]. An interpretation of the backscatter of a possible two-layer structure might reveal facts about their surface and subsurface properties in the same way as demonstrated here at the example to frozen lakes.

For further verifying the model or enhancing it with empirical assumptions, on-site measurements of bubble density and shape in addition to weather data can lead to a quantitative evaluation of the model. Such validation might show the importance of further developing this model and the requirement of enhancing the model by including higher order scattering mechanisms such as triple scattering [4]. The trihedral backscattering could predict even higher horizontal than vertical backscattering and a higher backscattered power with a water subsurface presence. Obtaining on-site measurements together with time series of fully polarimetric L-band SAR acquisitions, similar to the one performed in [93], might show clearer the impact of weather and climate changes on the ice and can demonstrate the potential benefits of a wide SAR coverage for these areas. Combining fully polarimetric measurements with interferometry [13], [78], that will be more feasible in future SAR missions [53], [66], might be able to estimate the volume contribution compared to the subsurface and dihedral contribution, which is one of the unknowns in the model and it might aid in further developing the model and in inverting for the subsurface permittivity. Another possibility to resolve more unknowns in the model might be achieved through combining different look angles and exploiting the local incident angle dependency in the model. A possible solution for having different look angles could be to consider multistatic SAR constellations [54], which would require the adaption of the model equations starting from the general dipole scattering matrix in Appendix B, Eq. (B.11) to the multistatic case. Another possibly powerful way to separate the volume contribution from the subsurface and dihedral contribution might be the application of SAR tomography in combination with polarimetry, as it allows the separation of multiple phase centres in the vertical direction. Even the retrieval of volume structure information might be

possible and would be a promising application, as already demonstrated with L-band airborne data in [69], [83], [61].

Bibliography

- [1] N. Al-Kahachi and K. P. Papathanassiou, "Polarimetric investigation of a two surface layer structure," *Synthetic Aperture Radar (EUSAR), European Conference on*, pp. 1–4, June 2010.
- [2] J. L. Alvarez-Perez, "Two novel studies of electromagnetic scattering in random media in the context of radar remote sensing," Ph.D. dissertation, DLR Oberpfaffenhofen, 2001.
- [3] D. Atwood, D. Small, and R. Gens, "Improving PolSAR land cover classification with radiometric correction of the coherency matrix," *IEEE Journal of Selected Topics in Applied Earth Observations and Remote Sensing*, vol. 5, no. 3, pp. 848–856, June 2012.
- [4] D. Atwood, S. Leinss, B. Matthiss, L. Jenkins, S. Wdowinski, and S.-H. Hong, "Wave propagation model for coherent scattering from a randomly distributed target," in *Proc. POLinSAR*, Frascati, Italy, 2013, pp. 1–7.
- [5] C. A. Balanis, *Advanced Engineering Electromagnetics*. John Wiley and Sons, 1989.
- [6] S. Bertl and J. Detlefsen, "Effects of a reflecting background on the results of active MMW SAR imaging of concealed objects," *IEEE Transactions on Geoscience and Remote Sensing*, vol. 49, no. 10, pp. 3745–3752, oct. 2011.
- [7] S. Bickel and R. Bates, "Effects of magneto-ionic propagation on the polarization scattering matrix," *Proceedings of the IEEE*, vol. 53, no. 8, pp. 1089–1091, Aug. 1965.
- [8] W.-M. Boerner, "Basic concepts in radar polarimetry," POLSARPRO V3.0 - Lecture Notes, UIC-ECE Communications, Sensing and Navigation Laboratory, 2006.

- [9] L. C. Brown and C. R. Duguay, "A comparison of measured and simulated ice thickness from the 2008-2010 ice seasons in Churchill, Manitoba," Interdisciplinary Centre on Climate Change (IC3), University of Waterloo, Canada, Tech. Rep., 2010.
- [10] S. A. Carn, "Lecture notes on scattering," http://www.geo.mtu.edu/~scarn/teaching/GE4250/scattering_lecture.ppt, 2010, [Online; status: November 16, 2011].
- [11] S. R. Cloude, *Polarisation: Applications in Remote Sensing*. Oxford University Press, 2010.
- [12] S. Cloude, J. Fortuny, J. Lopez-Sanchez, and A. Sieber, "Wide-band polarimetric radar inversion studies for vegetation layers," *IEEE Transactions on Geoscience and Remote Sensing*, vol. 37, no. 5, pp. 2430–2441, Sept. 1999.
- [13] S. Cloude and K. Papathanassiou, "Polarimetric SAR interferometry," *IEEE Transactions on Geoscience and Remote Sensing*, vol. 36, no. 5, pp. 1551–1565, Sept. 1998.
- [14] S. Cloude, K. Papathanassiou, and W. Boerner, "The remote sensing of oriented volume scattering using polarimetric radar interferometry," in *Proceedings of ISAP*, 2000, pp. 549–552.
- [15] S. Cloude and E. Pottier, "A review of target decomposition theorems in radar polarimetry," *IEEE Transactions on Geoscience and Remote Sensing*, vol. 34, no. 2, pp. 498–518, March 1996.
- [16] —, "An entropy based classification scheme for land applications of polarimetric SAR," *IEEE Transactions on Geoscience and Remote Sensing*, vol. 35, no. 1, pp. 68–78, Jan. 1997.
- [17] J. Dall, "Insar elevation bias caused by penetration into uniform volumes," *IEEE Transactions on Geoscience and Remote Sensing*, vol. 45, no. 7, pp. 2319–2324, 2007.
- [18] G. De Loor, "Dielectric properties of heterogeneous mixtures with a polar constituent," *Applied Scientific Research, Section B*, vol. 11, pp. 310–320, 1964.
- [19] J. Detlefsen and U. Siart, *Grundlagen der Hochfrequenztechnik*. München: Oldenbourg Wissenschaftsverlag, 2012.

- [20] A. Doulgeris and F. Meyer, "Severe radio frequency interference in ALOS PALSAR images," in *Proc. POLinSAR*, Frascati, Italy, 2011, pp. 1–8.
- [21] C. R. Duguay and P. M. Lafleur, "Monitoring ice freeze-up and break-up of shallow tundra lakes and ponds," in *Proceedings of GER-97 (International Symposium: Geomatics in the Era of RADARSAT) (on CD-ROM)*, May 1997.
- [22] —, "Determining depth and ice thickness of shallow sub-arctic lakes using space-borne optical and SAR data," *International Journal of Remote Sensing*, vol. 24, no. 3, pp. 475–489, 2003. [Online]. Available: <http://www.tandfonline.com/doi/abs/10.1080/01431160304992>
- [23] C. R. Duguay, W. R. Rouse, P. M. Lafleur, D. L. Boudreau, Y. Crevier, and T. J. Pultz, "Analysis of multi-temporal ERS-1 SAR data of subarctic tundra and forest in the northern Hudson Bay lowland and implications for climate studies," *Can. J. Remote Sens.*, vol. 25(1), pp. 21–33, 1999.
- [24] C. R. Duguay, G. M. Flato, M. O. Jeffries, P. Ménard, K. Morris, and W. R. Rouse, "Ice-cover variability on shallow lakes at high latitudes: Model simulations and observations," *Hydrological Processes*, vol. 17, no. 17, pp. 3465–3483, 2003. [Online]. Available: <http://dx.doi.org/10.1002/hyp.1394>
- [25] C. R. Duguay, T. J. Pultz, P. M. Lafleur, and D. Draï, "RADARSAT backscatter characteristics of ice growing on shallow sub-arctic lakes, Churchill, Manitoba, Canada." *Hydrological Processes*, vol. 16, pp. 1631–1644, 2002.
- [26] C. Elachi, *Introduction to the Physics and Techniques of Remote Sensing*, 2nd ed. Wiley-Interscience, 1987.
- [27] M. Engram, "SAR analysis of CH₄ bubbles in lake ice," University of Alaska; Water and Environmental Research Center, Tech. Rep., 2 April 2010.
- [28] Environment Canada, "Homepage," <http://www.ec.gc.ca/glaces-ice/>, 2012, [Online; status: July 10, 2012].
- [29] H. Ewe, J. Johnson, and K. Chen, "A comparison study of the surface scattering models and numerical model," in *IEEE International Geoscience and Remote Sensing Symposium*, vol. 6, 2001, pp. 2692–2694.

- [30] W. Fa, M. A. Wiczorek, and E. Heggy, "Modeling polarimetric radar scattering from the lunar surface: Study on the effect of physical properties of the regolith layer," *Journal of Geophysical Research*, vol. 116, no. E3, p. E03005, March 2011. [Online]. Available: <http://www.agu.org/pubs/crossref/2011/2010JE003649.shtml>
- [31] Flatrock.org, "Homepage," http://flatrock.org.nz/archive/2011/Aug/15/but_never_jam_today/, 2011, [Online; status: April 12, 2012].
- [32] A. Freeman and S. Durden, "A three-component scattering model for polarimetric SAR data," *IEEE Transactions on Geoscience and Remote Sensing*, vol. 36, no. 3, pp. 963–973, May 1998.
- [33] A. Freeman and T. Farr, "Modeling surface and subsurface scattering from saline soils," in *Proc. POLinSAR*. ESA, 2007, pp. 1–4.
- [34] A. Fung, Z. Li, and K. Chen, "Backscattering from a randomly rough dielectric surface," *IEEE Transactions on Geoscience and Remote Sensing*, vol. 30, no. 2, pp. 356–369, March 1992.
- [35] M.-L. Geai, K. Walter, and G. G., "Climate change and methane emissions: Pan arctic lake ice methane monitoring network (PALIMMN)," *International Polar Year OSLO science conference*, 2010.
- [36] T. Geldsetzer, J. van der Sanden, and H. Drouin, "Advanced SAR applications for Canada's river and lake ice," in *IEEE International Geoscience and Remote Sensing Symposium (IGARSS)*, July 2011, pp. 3168–3170.
- [37] I. Gherboudj, M. Bernier, and R. Leconte, "A backscatter modeling for river ice: Analysis and numerical results," *IEEE Transactions on Geoscience and Remote Sensing*, vol. 48, no. 4, pp. 1788–1798, April 2010.
- [38] J. Gill and J. J. Yackel, "Evaluation of C-band SAR polarimetric parameters for discrimination of first-year sea ice types," *Canadian Journal of Remote Sensing*, vol. 38, no. 03, pp. 306–323, 2012. [Online]. Available: <http://pubs.casi.ca/doi/abs/10.5589/m12-025>
- [39] Google Earth, "Homepage," <http://maps.google.de/maps>, 2012, [Online; status: April 1, 2012].
- [40] I. Hajnsek, E. Pottier, and S. Cloude, "Inversion of surface parameters from polarimetric SAR," *IEEE Transactions on Geoscience and Remote Sensing*, vol. 41, no. 4, pp. 727–744, April 2003.

- [41] I. Hajnsek, "Inversion of surface parameters using polarimetric SAR," Ph.D. dissertation, DLR Oberpfaffenhofen, 2001.
- [42] R. F. Harrington, *Time-Harmonic Electromagnetic Fields*. New York: McGraw-Hill Book Company, 1961.
- [43] M. Hellmann and S. Cloude, "Polarimetric interferometry and differential interferometry," in *Proceedings RTO-EN-SET-081*, October 2004, pp. 6.1–6.54. [Online]. Available: <http://www.dtic.mil/dtic/tr/fulltext/u2/a437525.pdf>
- [44] P. Hoekstra and A. Delaney, "Dielectric properties of soils at UHF and microwave frequencies," *J. Geophys. Res.*, vol. 79, no. 11, pp. 1699–1708, 1974.
- [45] Japan Aerospace Exploration Agency, "Homepage, advanced land observing satellite "DAICHI" (ALOS)," http://www.jaxa.jp/projects/sat/alos/index_e.html, 2012, [Online; status: January 15, 2013].
- [46] M. O. Jeffries, *Satellite Image Atlas of Glaciers of the World: Glaciers of North America*. U.S. Geological Survey, 2002, ch. Ellesmere Island ice shelves and ice islands, pp. J147–J164.
- [47] M. O. Jeffries, K. Morris, and N. Kozlenko, "Ice characteristics and processes, and remote sensing of frozen rivers and lakes," *Geophys. Monogr. Ser.: Remote Sensing in Northern Hydrology: Measuring Environmental Change*, vol. 163, pp. 63–90, 2005.
- [48] M. O. Jeffries, K. Morris, W. F. Weeks, and H. Wakabayashi, "Structural and stratigraphic features and ERS-1 synthetic aperture radar backscatter characteristics of ice growing on shallow lakes in NW Alaska, winter 1991–1992," *Journal of Geophysical Research: Oceans*, vol. 99, no. C11, pp. 22 459–22 471, 1994. [Online]. Available: <http://dx.doi.org/10.1029/94JC01479>
- [49] M. Jeffries, K. Morris, and G. Liston, "A method to determine lake depth and water availability on the north slope of Alaska with spaceborne imaging radar and numerical ice growth modelling," *ARCTIC*, vol. 49, no. 4, 1996. [Online]. Available: <http://arctic.synergiesprairies.ca/arctic/index.php/arctic/article/view/1212>
- [50] J. S. Kim, A. Danklmayer, and K. Papathanassiou, "Correction of ionospheric distortions in low frequency interferometric SAR data," in *IEEE International Geoscience and Remote Sensing Symposium (IGARSS)*, July 2011, pp. 1505–1508.

- [51] N. Kozlenko and M. Jeffries, "Bathymetric mapping of shallow water in thaw lakes on the north slope of Alaska with spaceborne imaging radar," *ARCTIC*, vol. 53, no. 3, 2000. [Online]. Available: <http://arctic.synergiesprairies.ca/arctic/index.php/arctic/article/view/860>
- [52] T. Kozłowski, "Soil freezing point as obtained on melting," *Cold Regions Science and Technology*, vol. 38, no. 2–3, pp. 93 – 101, 2004. [Online]. Available: <http://www.sciencedirect.com/science/article/pii/S0165232X03001198>
- [53] G. Krieger, I. Hajnsek, K. Papathanassiou, M. Younis, and A. Moreira, "Interferometric synthetic aperture radar (SAR) missions employing formation flying," *Proceedings of the IEEE*, vol. 98, no. 5, pp. 816 –843, May 2010.
- [54] G. Krieger and A. Moreira, "Spaceborne bi- and multistatic SAR: potential and challenges," *Radar, Sonar and Navigation, IEE Proceedings*, vol. 153, no. 3, pp. 184 – 198, June 2006.
- [55] Y. Lasne, P. Paillou, T. August-Bernex, G. Ruffie, and G. Grandjean, "A phase signature for detecting wet subsurface structures using polarimetric L-band SAR," *IEEE Transactions on Geoscience and Remote Sensing*, vol. 42, no. 8, pp. 1683 – 1694, Aug. 2004.
- [56] Y. Lasne, P. Paillou, A. Freeman, T. Farr, K. McDonald, G. Ruffie, J.-M. Malezieux, and B. Chapman, "Study of hypersaline deposits and analysis of their signature in airborne and spaceborne SAR data: Example of Death Valley, California," *IEEE Transactions on Geoscience and Remote Sensing*, vol. 47, no. 8, pp. 2581 –2598, Aug. 2009.
- [57] J. S. Lee, L. Jurkevich, P. Dewaele, P. Wambacq, and A. Oosterlinck, "Speckle filtering of synthetic aperture radar images: A review," *Remote Sensing Reviews*, vol. 8, no. 4, pp. 313–340, 1994. [Online]. Available: <http://www.tandfonline.com/doi/abs/10.1080/02757259409532206>
- [58] J.-S. Lee, T. Ainsworth, and Y. Wang, "Generalized polarimetric model-based decompositions using extended incoherent scattering models," in *International Geoscience and Remote Sensing Symposium (IGARSS)*, July 2012, pp. 1421 –1424.
- [59] J.-S. Lee and E. Pottier, *Polarimetric Radar Imaging*. Boca Raton, FL, USA: CRC Press, 2009.

- [60] G. Leshkevich and S. Nghiem, "Using satellite radar data to map and monitor variations in Great Lakes ice cover," in *IEEE Radar Conference*, May 2009, pp. 1–3.
- [61] P. Lombardo and F. Lombardini, "Multi-baseline SAR interferometry for terrain slope adaptivity," in *IEEE National Radar Conference*, 13-15 May 1997, pp. 196–201.
- [62] A. Löw and W. Mauser, "A semiempirical surface backscattering model for bare soil surfaces based on a generalized power law spectrum approach," *IEEE Transactions on Geoscience and Remote Sensing*, vol. 44, no. 4, pp. 1022–1035, April 2006.
- [63] A. Löw, "Coupled modelling of land surface microwave interactions using ENVISAT ASAR data," Ph.D. dissertation, Ludwig Maximilians Universität München, 2004.
- [64] Maplesoft, "Homepage," <http://www.maplesoft.com/>, 2013, [Online; status: January 11, 2013].
- [65] G. Mie, "Beiträge zur Optik trüber Medien, speziell kolloidaler Metallösungen," *Annalen der Physik*, vol. 330, no. 3, pp. 377–445, 1908. [Online]. Available: <http://dx.doi.org/10.1002/andp.19083300302>
- [66] A. Moreira, G. Krieger, M. Younis, I. Hajnsek, K. Papathanassiou, M. Eineder, and F. De Zan, "Tandem-L: A mission proposal for monitoring dynamic earth processes," in *IEEE International Geoscience and Remote Sensing Symposium (IGARSS)*, July 2011, pp. 1385–1388.
- [67] A. Moreira, "Radar mit synthetischer Apertur – Grundlagen und Signalverarbeitung," Habilitationsschrift, Universität Fridericiana zu Karlsruhe (TH), 2000.
- [68] K. Morris, M. O. Jeffries, and W. F. Weeks, "Ice processes and growth history on arctic and sub-arctic lakes using ERS-1 SAR data," *Polar Record*, vol. 31, pp. 115–128, March 1995. [Online]. Available: <http://dx.doi.org/10.1017/S0032247400013619>
- [69] M. Nannini, R. Scheiber, R. Horn, and A. Moreira, "First 3-D reconstructions of targets hidden beneath foliage by means of polarimetric SAR tomography," *IEEE Geoscience and Remote Sensing Letters*, vol. 9, no. 1, pp. 60–64, Jan. 2012.

- [70] National Climate Data and Information Archive, "Homepage," http://www.climate.weatheroffice.gc.ca/climateData/canada_e.html, 2012, [Online; status: March 15, 2012].
- [71] S. Nghiem, G. Leshkevich, and R. Kwok, "C-band polarimetric backscatter observations of Great Lakes ice," in *IEEE International Geoscience and Remote Sensing Symposium (IGARSS)*, vol. 3, July 1998, pp. 1400–1402.
- [72] H. Ohgushi, *ALOS - User Handbook*, Earth Observation Research Center, Japan Aerospace Exploration Agency, 2007.
- [73] S. J. Orfanidis, *Electromagnetic Waves and Antennas*. www.ece.rutgers.edu/~orfanidi/ewa: Rutgers University, 2010.
- [74] I. Ostrovsky, "Methane bubbles in Lake Kinneret: Quantification and temporal and spatial heterogeneity," *Limnology and Oceanography by the American Society of Limnology and Oceanography*, vol. 48, no. 3, pp. 1030 – 1036, 2003.
- [75] P. Paillou, G. Grandjean, N. Baghdadi, E. Heggy, T. August-Bernex, and J. Achache, "Subsurface imaging in south-central Egypt using low-frequency radar: Bir Safsaf revisited," *IEEE Transactions on Geoscience and Remote Sensing*, vol. 41, no. 7, pp. 1672 – 1684, July 2003.
- [76] P. Paillou, S. Lopez, Y. Lasne, A. Rosenqvist, and T. Farr, "Mapping subsurface geology in Arid Africa using L-band SAR," in *IEEE International Geoscience and Remote Sensing Symposium*, July 2007, pp. 2685–2688.
- [77] P. Paillou, Y. Lasne, E. Heggy, J.-M. Malézieux, and G. Ruffié, "A study of P-band synthetic aperture radar applicability and performance for Mars exploration: Imaging subsurface geology and detecting shallow moisture," *Journal of Geophysical Research: Planets*, vol. 111, no. E6, pp. n/a–n/a, 2006. [Online]. Available: <http://dx.doi.org/10.1029/2005JE002528>
- [78] K. Papathanassiou, "Polarimetric SAR interferometry," Ph.D. dissertation, DLR Oberpfaffenhofen, 1999.
- [79] G. Parrella, N. Al-Kahachi, T. Jagdhuber, I. Hajnsek, and K. Papathanassiou, "Ice volume characterization using long-wavelength airborne PolSAR data," in *IEEE International Geoscience and Remote Sensing Symposium (IGARSS)*, July 2012, pp. 3245–3248.

- [80] A. Phelps, K. Peterson, and M. Jeffries, "Methane efflux from high-latitude lakes during spring ice melt," *Journal of Geophysical Research*, vol. 103 (D22), pp. 29 029–29 036, 1998.
- [81] G. Picardi, D. Biccari, A. Bazzoni, F. Fois, M. Iorio, R. Seu, P. Melacci, C. Federico, A. Frigeri, G. Minelli, L. Marinangeli, R. Orosei, D. Calabrese, E. Zampolini, W. Johnson, R. Jordan, J. Plaut, and A. Safaenili, "Mars advanced radar for subsurface and ionosphere sounding (MARSIS): subsurface performances evaluation," in *Proceedings of the International Radar Conference*, Sept. 2003, pp. 515 – 521.
- [82] G. Picardi, D. Biccari, R. Seu, L. Marinangeli, W. Johnson, R. Jordan, J. Plaut, A. Safaenili, D. Gurnett, G. Ori, R. Orosei, D. Calabrese, and E. Zampolini, "Performance and surface scattering models for the Mars advanced radar for subsurface and ionosphere sounding (MARSIS)," *Planetary and Space Science*, vol. 52, no. 1–3, pp. 149 – 156, 2004. [Online]. Available: <http://www.sciencedirect.com/science/article/pii/S0032063303001831>
- [83] A. Reigber and A. Moreira, "First demonstration of airborne SAR tomography using multibaseline L-band data," *IEEE Transactions on Geoscience and Remote Sensing*, vol. 38, no. 5, pp. 2142 –2152, Sept. 2000.
- [84] G. B. Rybicki and A. P. Lightman, *Radiative Processes in Astrophysics*. Wiley-VCH, 2004.
- [85] E. Santi, M. Brogioni, S. Paloscia, and P. Pampaloni, "Analysis of the frequency and polarization indexes over snow cover areas by means of experimental and theoretical data," in *Microwave Radiometry and Remote Sensing of the Environment (MicroRad), 12th Specialist Meeting on*, March 2012, pp. 1 –4.
- [86] J. Schneider, G. Grosse, and D. Wagner, "Land cover classification of tundra environments in the arctic Lena Delta based on Landsat 7 ETM+ data and its application for upscaling of methane emissions," *Remote Sensing of Environment*, vol. 113, no. 2, pp. 380–391, 2009.
- [87] J. Sharma, I. Hajnsek, K. Papathanassiou, and A. Moreira, "Polarimetric decomposition over glacier ice using long-wavelength airborne PolSAR," *IEEE Transactions on Geoscience and Remote Sensing*, vol. 49, no. 1, pp. 519 –535, Jan. 2011.
- [88] M. I. Skolnik, *Introduction to Radar Systems*. New York: McGraw-Hill Book Company, 2001.

- [89] L. Tsang, J. Pan, D. Liang, Z. Li, D. Cline, and Y. Tan, "Modeling active microwave remote sensing of snow using dense media radiative transfer (DMRT) theory with multiple-scattering effects," *IEEE Transactions on Geoscience and Remote Sensing*, vol. 45, no. 4, pp. 990–1004, April 2007.
- [90] F. T. Ulaby, R. K. Moore, and A. K. Fung, *Microwave Remote Sensing Volume 1*. Artech House, 1981.
- [91] H. Van De Hulst, *Light Scattering by Small Particles*. New York: Dover Publication Inc, 1982.
- [92] J. van der Sanden and H. Drouin, "Polarimetric RADARSAT-2 for river freeze-up monitoring," <http://www.polinsar2011.com/>, 2011, [Presentation slides; online; status: September 21, 2012].
- [93] —, "Satellite SAR observations of river ice cover: A RADARSAT-2 (C-band) and ALOS PALSAR (L-band) comparison," in *Proceedings 16th Workshop on the Hydraulics of Ice Covered Rivers*, 2011, pp. 179–197.
- [94] V. K. Varadan and V. V. Varadan, "Acoustic, electromagnetic and elastic wave scattering - focus on the T-matrix approach," in *Proceedings of the International Symposium sponsored by the U.S. Navy and Ohio State University*, 1979.
- [95] L. c. v. Vrbka and P. Jungwirth, "Brine rejection from freezing salt solutions: A molecular dynamics study," *Phys. Rev. Lett.*, vol. 95, p. 148501, Sept. 2005. [Online]. Available: <http://link.aps.org/doi/10.1103/PhysRevLett.95.148501>
- [96] K. M. Walter, M. E. Edwards, G. Grosse, S. A. Zimov, and F. S. Chapin, "Thermokarst lakes as a source of atmospheric CH₄ during the last deglaciation," *Science*, vol. 318, no. 5850, pp. 633–636, 2007.
- [97] K. M. Walter, M. Engram, C. Duguay, M. Jeffries, and F. S. Chapin, "Potential use of synthetic aperture radar (SAR) for estimating methane ebullition from arctic lakes," *Journal of the American Water Research Association*, vol. 44, no. 2, pp. 305 – 315, 2008.
- [98] K. M. Walter, S. A. Zimov, J. P. Chanton, D. Verbyla, and F. S. Chapin, "Methane bubbling from Siberian thaw lakes as a positive feedback to climate warming," *Nature*, vol. 443, pp. 71–75, 2006.

- [99] M. Watanabe, G. Kadosaki, Y. Kim, M. Ishikawa, K. Kushida, Y. Sawada, T. Tadono, M. Fukuda, and M. Sato, "Analysis of the sources of variation in L-band backscatter from terrains with permafrost," *IEEE Transactions on Geoscience and Remote Sensing*, vol. 50, no. 1, pp. 44–54, Jan. 2012.
- [100] W. F. Weeks, A. G. Fountain, M. L. Bryan, and C. Elachi, "Differences in radar return from ice-covered north slope lakes," *Journal of Geophysical Research: Oceans*, vol. 83, no. C8, pp. 4069–4073, 1978. [Online]. Available: <http://dx.doi.org/10.1029/JC083iC08p04069>
- [101] W. F. Weeks, A. J. Gow, and R. J. Schertler, "Ground-truth observations of ice-covered north slope lakes imaged by radar," Cold Regions Research and Engineering Lab Hanover NH, Tech. Rep. ADA108342, 1981.
- [102] W. F. Weeks, P. V. Sellmann, and W. J. Campbell, "Interesting features of radar imagery of ice-covered north slope lakes," *J. Glaciol.*, vol. 18, no. 78, 1977.
- [103] K. Wohletz and G. Heiken, *Volcanology and Geothermal Energy*. Berkley: University of California Press, 1992, available online: <http://ark.cdlib.org/ark:/13030/ft6v19p151/>.
- [104] M. Younis and W. Wiesbeck, "SAR with digital beamforming on receive only," in *Proceedings International Geoscience and Remote Sensing Symposium*, vol. 3, 1999, pp. 1773–1775 vol.3.

Appendix A

Nomenclature

Variable	Description
α	Alpha angle
α_i	Alpha angle of the i^{th} scattering mechanism
β	Half of the distribution width of the surface slope angles, and angle of rotation in Section 2.4
β_i	Angle of rotation of the i^{th} scattering mechanism
ϵ	Permittivity of a medium
ϵ_r	Relative permittivity of a medium
λ	Wavelength
λ_i	Eigenvalue
μ	Permeability of a medium
μ_r	Relative permeability of a medium
σ	Radar cross section
σ^0	Average radar cross section per unit area
σ_{rms}	Standard deviation of surface height
θ_L	Local incident angle
θ_{ref}	Reflection angle
θ_t	Transmission angle
θ_{inc}	Polar angle of the wave incident on a particle where the centre of the spherical coordinate system is specified by the particle.
θ_{obs}	Polar angle of the considered scattered wave from a particle where the centre of the spherical coordinate system is specified by the particle.

Variable	Description
$\theta_{\text{orientation}}$	Orientation distribution width of the particles within the effective volume (equals to the physical orientation distribution width for Rayleigh particles)
ϕ_{inc}	Azimuthal angle of the wave incident on a particle where the centre of the spherical coordinate system is specified by the particle.
ϕ_{obs}	Azimuthal angle of the considered scattered wave from a particle where the centre of the spherical coordinate system is specified by the particle.
$\phi_{\text{orientation}}$	Physical orientation distribution width of large particles
a	Particle radius
A	Anisotropy
A_0	Illuminated area in Section 2.3
A_p	Particle anisotropy
C_3	Covariance matrix
c_i	Single element of the covariance matrix
E	Electric field
E_h	Horizontal component of the electric field
E_i	Incident electric field
E_v	Vertical component of the electric field
E_s	Scattered electric field
$E(\theta, \phi)$	Normalised scattering matrix of a single ellipsoid
G	Antenna gain
H	Entropy
$H(\theta, \phi)$	Normalised scattering matrix of a single dipole
k	Wavenumber
\vec{k}_l	Lexicographic scattering vector
\vec{k}_p	Pauli vector
l	Surface correlation length in Section 4.1.2, length of the long dipole in Section 5.2.2, and volume thickness in Section 5.4
N	Volume density
m	Ratio of the particle's refractive index to the refractive index of the background material
p_i	The i^{th} polarisability of the particle
$P(\theta)$	Probability density function of the orientation angle of the particles in the volume
P_i	Appearance probability for a decomposed scattering mechanisms (see Section 2.4.1)

Variable	Description
P_r	Received power
P_t	Transmitted power
P_q	Power coefficient of the scattering mechanism 'q'
r	Distance of the observed field from the source
R	Distance between object and radar
$R_{h,v}$	Horizontal and vertical Bragg scattering coefficient
$R_{\perp,\parallel}$	Horizontal and vertical Fresnel reflection coefficient
S	Scattering matrix
S_{pq}	Scattering coefficient for the polarisation 'p' of the incident wave and the polarisation 'q' of the scattered wave
T_3	Coherency matrix
T_4	The 4×4 coherency matrix
t_i	Single element of the coherency matrix
$T_{\perp,\parallel}$	Horizontal and vertical transmission coefficient
u_i	Eigenvector
U_3	Matrix containing the eigenvectors of the coherency matrix
U_4	Matrix containing the eigenvectors of the T_4 coherency matrix

Appendix B

Derivation of the dipole scattering matrix

To derive the dipole equation, a method to calculate the projection of the wave incident on the dipole in 3D space is required. A way to calculate the angle between the incident field and the dipole, which is required to obtain the projection is shown here. The same method is also used to calculate the projection of the scattered wave on the observed field direction. For the geometry described in Fig. B.1, the angle θ_{wanted} between the two plotted lines is of interest.

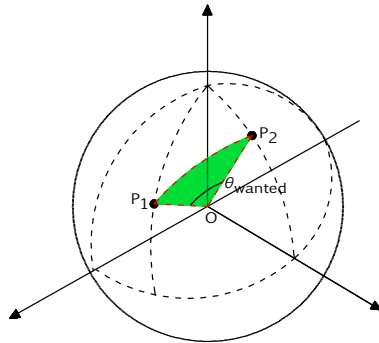


Figure B.1 Geometry for the calculation of θ_{wanted}

The first line is from the origin to $(r, \theta, \phi) = (1, \theta_{p1}, \phi_{p1})$, and the second one is from the origin to $(r, \theta, \phi) = (1, \theta_{p2}, \phi_{p2})$. In a cartesian coordinates system P_1 lays at

$$\begin{pmatrix} x_{p1} \\ y_{p1} \\ z_{p1} \end{pmatrix} = \begin{pmatrix} \cos \phi_{p1} \sin \theta_{p1} \\ \sin \phi_{p1} \sin \theta_{p1} \\ \cos \theta_{p1} \end{pmatrix} \quad (\text{B.1})$$

and the second point P_2 is written as

$$\begin{pmatrix} x_{p2} \\ y_{p2} \\ z_{p2} \end{pmatrix} = \begin{pmatrix} \cos \phi_{p2} \sin \theta_{p2} \\ \sin \phi_{p2} \sin \theta_{p2} \\ \cos \theta_{p2} \end{pmatrix}. \quad (\text{B.2})$$

The distance L between the P_1 and P_2 can be calculated by

$$\begin{aligned} L^2 &= (x_2 - x_1)^2 + (y_2 - y_1)^2 + (z_2 - z_1)^2 \\ &= (\cos \phi_{p2} \sin \theta_{p2} - \cos \phi_{p1} \sin \theta_{p1})^2 \\ &\quad + (\sin \phi_{p2} \sin \theta_{p2} - \sin \phi_{p1} \sin \theta_{p1})^2 + (\cos \theta_{p2} - \cos \theta_{p1})^2 \\ &= 2 - 2 \cos \phi_{p2} \cos \phi_{p1} \sin \theta_{p2} \sin \theta_{p1} \\ &\quad - 2 \sin \phi_{p2} \sin \phi_{p1} \sin \theta_{p2} \sin \theta_{p1} - 2 \cos \theta_{p2} \cos \theta_{p1}. \end{aligned} \quad (\text{B.3})$$

The distance L can also be calculated by considering the triangle P_1 - P_2 - O , and obtaining the length of the third side from the length of the two other sides and the angle between them by

$$L^2 = 1 + 1 - 2 \cos \theta_{\text{wanted}}. \quad (\text{B.4})$$

From solving the last two equations

$$\begin{aligned} \cos \theta_{\text{wanted}} &= \cos \phi_{p2} \cos \phi_{p1} \sin \theta_{p2} \sin \theta_{p1} \\ &\quad + \sin \phi_{p2} \sin \phi_{p1} \sin \theta_{p2} \sin \theta_{p1} + \cos \theta_{p2} \cos \theta_{p1} \end{aligned} \quad (\text{B.5})$$

where $\cos \theta_{\text{wanted}}$ can be used to calculate the projection of one line on another line with a θ_{wanted} angle between them in a three dimensional space.

In the derivation of the dipole scattering, the coordinate system presented in Section 5.2.1 is used. The scattered field is the projection of the vertically and horizontally polarised field of the incident wave on the dipole multiplied by the projection of the scattered wave on the horizontal and vertical polarisation of the receiver. In general the horizontal direction for incident/scattered wave compared to the propagation direction of the wave in a spherical coordinate system is $r = 1$, $\theta_H = \pi/2$, $\phi_H = \phi_{\text{inc/obs}} - \pi/2$. For the vertical polarization this

results in $r = 1$, $\theta_V = \theta_{\text{inc}/\text{obs}} - \pi/2$, $\phi_V = \phi_{\text{inc}/\text{obs}}$. For the incident wave, the projection of the horizontally polarized wave on the dipole is as follows

$$\begin{aligned} E_{H,\text{dipole}} = & E_{H,\text{inc}} (\cos \phi \cos(\phi_{\text{inc}} - \pi/2) \sin \theta \sin(\pi/2) \\ & + \sin \phi \sin(\phi_{\text{inc}} - \pi/2) \sin \theta \sin(\pi/2) + \cos \theta \cos(\pi/2)) \quad (\text{B.6}) \\ = & -E_{H,\text{inc}} \sin \theta \sin(\phi - \phi_{\text{inc}}). \end{aligned}$$

The projection of the vertically polarized wave on the dipole becomes

$$\begin{aligned} E_{V,\text{dipole}} = & E_{V,\text{inc}} (\cos \phi \cos \phi_{\text{inc}} \sin \theta \sin(\theta_{\text{inc}} - \pi/2) \\ & + \sin \phi \sin \phi_{\text{inc}} \sin \theta \sin(\theta_{\text{inc}} - \pi/2) + \cos \theta \cos(\theta_{\text{inc}} - \pi/2)) \quad (\text{B.7}) \\ = & -E_{V,\text{inc}} (\cos(\phi - \phi_{\text{inc}}) \sin \theta \cos \theta_{\text{inc}} + \cos \theta \sin \theta_{\text{inc}}). \end{aligned}$$

In the same way, the projection of the scattered wave is calculated

$$E_{H,\text{scattered}} = -E_{H,\text{dipole}} \sin \theta \sin(\phi - \phi_{\text{obs}}) \quad (\text{B.8})$$

$$E_{V,\text{scattered}} = -E_{V,\text{dipole}} (\cos(\phi - \phi_{\text{obs}}) \sin \theta \cos \theta_{\text{obs}} + \cos \theta \sin \theta_{\text{obs}}). \quad (\text{B.9})$$

The scattering matrix is obtained from the product of the projection of the incident field on the dipole and the projection of the dipole on the scattered field

$$[H(\theta, \theta_{\text{inc}}, \theta_{\text{obs}}, \phi, \phi_{\text{inc}}, \phi_{\text{obs}})] = \begin{bmatrix} S_{\text{hh}}^H & S_{\text{hv}}^H \\ S_{\text{vh}}^H & S_{\text{vv}}^H \end{bmatrix}, \quad (\text{B.10})$$

with

$$\begin{aligned} S_{\text{hh}}^H &= \sin \theta \sin(\phi - \phi_{\text{inc}}) \sin \theta \sin(\phi - \phi_{\text{obs}}) \\ S_{\text{hv}}^H &= (\cos(\phi - \phi_{\text{inc}}) \sin \theta \cos \theta_{\text{inc}} + \cos \theta \sin \theta_{\text{inc}}) \sin \theta \sin(\phi - \phi_{\text{obs}}) \\ S_{\text{vh}}^H &= \sin \theta \sin(\phi - \phi_{\text{inc}}) (\cos(\phi - \phi_{\text{obs}}) \sin \theta \cos \theta_{\text{obs}} + \cos \theta \sin \theta_{\text{obs}}) \quad (\text{B.11}) \\ S_{\text{vv}}^H &= (\cos(\phi - \phi_{\text{inc}}) \sin \theta \cos \theta_{\text{inc}} + \cos \theta \sin \theta_{\text{inc}}) \cdot \\ & \quad (\cos(\phi - \phi_{\text{obs}}) \sin \theta \cos \theta_{\text{obs}} + \cos \theta \sin \theta_{\text{obs}}). \end{aligned}$$

For the monostatic SAR case with $\phi_{\text{inc}} = \phi_{\text{obs}} = \pi$, Eq. (5.4) is obtained.